Calculation of the Electrical Conduction of Molecules and Nanowires

Watheq Zako Elias

School of Physics and Astronomy

Cardiff University

A thesis submitted for the degree of

Doctor of Philosophy

May 2014

DECLARATION

This work has not been submitted in substance for any other degree or award at this or any other university or place of learning, nor is being submitted concurrently in candidature for any degree or other award.

Signed ..... (candidate) Date .....

STATEMENT 1

This thesis is being submitted in partial fulfillment of the requirements for the degree of PhD.

Signed ..... (candidate) Date .....

STATEMENT 2

This thesis is the result of my own independent work/investigation, except where otherwise stated. Other sources are acknowledged by explicit references. The views expressed are my own.

Signed ..... (candidate) Date .....

STATEMENT 3

I hereby give consent for my thesis, if accepted, to be available for photocopying and for inter-library loan, and for the title and summary to be made available to outside organisations.

Signed ..... (candidate) Date .....

I would like to dedicate this thesis to my lovely wife Nasam, my little angels Emmanuel and Daniel, and my family.

ACKNOWLEDGEMENTS

I would like to thank my supervisor Dr. Clarence C. Matthai and my co-supervisor Dr. Martin Elliott for their valuable guidance, support and supervision throughout the period of my research.

My sincere thanks also goes to A. Fasolino and J. Los for sharing the code of LCBOPII with me to use.

I would like to express my gratitude to the Iraqi government represented by the Iraqi cultural attaché in London for the financial sponsoring and their valuable assistant over almost five years of my language course and PhD study.

Many thanks are also due to the administrative and academic staffs at School of Physics and Astronomy for the cooperation, especially Computing Support Staff.

I would like to express my indebtedness to the members of Nanoscale Science & Technology research group at School of Physics and Astronomy, Cardiff University, Dr. J Emyr Macdonald and Dr. Andriy Moskalenko and my colleagues Mark, Ellis, Isam, Athraa, Rangeen and Adam for the lovely friendship environment they have given me and their nice company.

I also acknowledge Gareth Jones, the developer of EHTransport code, for his help and cooperation.

I am also grateful to my family support. I would thank my parents, my parents-in-law, my sisters and brothers for their constant support and encouragement. I especially thank my younger sister Nadia for her help, valuable advices and support.

Finally, the constant love and support of my gorgeous wife Nasam and my two lovely kids Emmanuel and Daniel have helped me to go through the difficulties of my study. It is their love and support that will help me keep going also in the future.

ABSTRACT

As electronics become more and more miniaturised, there is much interest in increasing knowledge about the electronic and transport properties of nano-systems. In particular, there has been some focus on understanding the physics of nanowires with prescribed properties. Two different groups of systems have been considered that of 1D organic molecular nanowires and 2D interconnects based on graphene. In order to develop a deeper insight of the factors that determine the electronic structure and consequently the electrical transport properties, it is desirable to carry out computer simulation studies of these systems.

The work reported in this thesis has focused on studying the porphyrin and DNA molecules as well as investigating the consequences of engineered 2D graphene interconnect. The latter class of systems has included graphene nanoribbons (GNRs), graphene sheets with grain boundaries (GGBs) and graphene nanomeshes (GNMs).

The methodology was to use self-consistent extended Hückel theory (SC-EHT) and density functional theory (DFT) in combination with non-equilibrium Green functions (NEGFs) formalism to investigate the electronic and transport properties of these systems. The SC-EHT calculations were performed using an in-house developed C++ code named EHTransport. While the SIESTA package was employed for the DFT.

It was found that the SC-EHT approach produced comparable results with that obtained by DFT. This supports the idea that the semi-empirical methods can be as valid as *ab-initio* approaches. The findings demonstrated that porphyrin, DNA, and graphene based systems are very promising candidates to incorporate in future electronics.

PUBLICATIONS

1. Watheq Elias, M. Elliott and C. C. Matthai. Electrical transport of zig-zag and folded graphene nanoribbons. *MRS Proceedings*, 1549: 41-46, (2013). doi: 10.1557/opl.2013.950.

2. Gareth Jones, Watheq Elias, M. Elliott and C. C. Matthai. Computational studies investigating the effect of sequencing and environment on the conductance of DNA nanowires. *MRS Proceedings*, 1553, (2013). doi: 10.1557/opl.2013.1058.

3. Watheq Zako Elias, Martin Elliott and Clarence Matthai. On the Effect of Grain Boundaries on the Electronic and Transport Properties of Graphene. To be published in *MRS Proceedings*.

4. G. Jones, Watheq Elias, M. Elliott, C.C. Matthai. A computational study of the factors affecting the electrical conductance of long chain n-porphyrin di-thiols. *Physica B: Condensed Matter*, 446(0):71-79, 2014.

CONTENTS

LIST OF FIGURES

LIST OF TABLES

CHAPTER 1

INTRODUCTION

In 1965, Moore anticipated that the density of transistors on an electronic chip would double every year [1]. Indeed (till now) Moore's predictions were in line with what is really achieved in electronic industry especially after the introduction of the first Ultrabook laptop based on 14 nm process node in September 2013 by Intel. But, sooner or later, Moore's law will reach its limits due to some serious technological, physical limitations and some economical barriers. For instance, shrinking a device size into the scale of 100 nm requires the use of costly lithography equipment and other facilities. Moreover, scaling the oxide layer in MOSFETs down to the order of a few angstroms increases the leakage currents to values comparable to that of ON state which leads to extremely high dissipation of power and makes the device useless [2]. Table 1.1 shows the International Technology Roadmap for Semiconductors ITRS trends for MOS devices covering the interval (2006-2016) [3]. The figures below show the increase in the power dissipation with decreasing the thickness of oxide layer.

An alternative and potentially very attractive strategy to overcome these challenges is the 'bottom-up' approach. This approach depends on replacing the traditional semiconductors with an individual molecule to represent a basic unit for building

Table 1.1: The IRTS trends for MOS devices. Adopted from ref. [2]

Year	2006	2007	2010	2013	2016
MPU physical gate length (nm) (Lg)	70	65	45	32	22
Supply voltage (V)	0.9	0.8	0.6	0.5	0.4
Number of transistors per chip (10^6)	878	1,106	2,212	4,424	8,848
Oxide thickness (nm) (0.02Lg)	1.4	1.3	0.9	0.64	0.44
Max power dissipation (W)	180	190	218	251	288

a device within the nanometer scale. Building such nanoscale devices requires connecting a molecule to a metal contact (lead). This connection will considerably affect the electronic structure of the molecule and consequently its electrical transport properties. Therefore, setting up theoretical models and developing simulation codes are required in order to study the factors that affect the I-V characteristics of an individual molecule “sandwiched" between two or three metal leads. One of the several procedures used for theoretical modelling of electrical conduction through molecules is the Non-Equilibrium Green's function (NEGF) approach. This approach involves firstly, computing the Hamiltonian of the system under study. Secondly, the Green's function of that Hamiltonian is evaluated from which the transmission spectra (and current) at a particular energy and applied bias voltage are extracted.

To obtain the Hamiltonian H, two main categories of methods can be employed: *ab initio* methods like Density Functional Theory (DFT) and semi-empirical approaches like Extended Hückel Theory (EHT). The main difference between the two is that the DFT computes the Hamiltonian from “scratch”. Therefore for systems with large numbers of molecules, it requires enormous computing resources and hence consumes lots of time. On the other hand, EHT uses parameter sets that are obtained by matching experimental and theoretical data. As a result, it often uses a smaller basis set; correspondingly it uses less computer resources and time and most importantly can tackle much larger systems. Accordingly, these crucial points qualify the EHT to be an effective alternative to DFT for studying large systems.

Molecular conduction may be viewed at many different levels of complexity. At its simplest, it is the tunnelling of carriers from one electrode to another across the molecule. The transport can be band-like or, in some instances, might be described by hopping. Most of the theoretical investigations to date have utilized a Landauer description of the tunnelling across the molecule [4–6]. These are effectively within the framework of the one electron picture and the transport occurs through the molecular orbitals on a single electronic potential energy surface. Within this description, the molecular orbitals can be determined through first principles calculations like density functional theory and configuration interaction (Hartree-Fock), or at an empirical or semi-empirical level. Whilst the molecular energy spectrum obtained by first principles techniques is accurate with regard to equilibrium properties, these techniques are

computationally expensive. Besides, it is not clear to what extent they can be applied reliably to strongly correlated transport. In addition, DFT techniques are not always reliable with respect to excited states and so they do not reproduce the correct conductance.

By contrast, the semi-empirical Self Consistent Extended Hückel Theory (SC-EHT) method has the advantage of being computationally tractable and also it provides the flexibility to tailor the band-gap. This is very important in the study of conduction. Moreover, the non-orthogonal basis set is good for describing chemical bonding which in turn allows for transferability. It is the transferability [1] that makes the SC-EHT very effective in describing a wide range of properties across many different systems. Examples of these studies include the determination of band offsets and Schottky barriers at semiconductor interfaces and the optical spectra of adatom adsorbed surfaces [7, 8].

One particular family of molecules being investigated as potential candidates for molecular conductors are the porphyrins [9–11], characterised by a planar conjugated ring containing 20 carbon atoms and 4 nitrogen atoms, usually with a metal ion in the centre (Figure 1.1). This family and its derivatives include many common molecules in biology, which would be expected to show interesting transport behaviours. It may also be possible to construct molecular wires using porphyrins as the building blocks [12, 13]. Experiments have shown that the metal-porphyrins can have multiple separate conduction states [14], which are believed to be due to conformational changes. Porphyrin wires have also been studied experimentally, and theoretically by the DFT/NEGF approach [15]. This combination of interesting electrical properties, prior results and wide variety of possible chemical and conformational changes make the porphyrins a useful tool for benchmarking new systems. Although small enough to run with DFT, the wide variety of these possible structures makes exploring all possible variations a daunting task.

Another promising class of molecules to be used in molecular electronics is DNA. The great interest in the DNA molecule as a possible component of molecular electronic devices is due to its unique recognition and self-assembling properties. These properties

[1] The transferability of the EHT parameters for a species is the ability to use them in different physical and chemical environments.

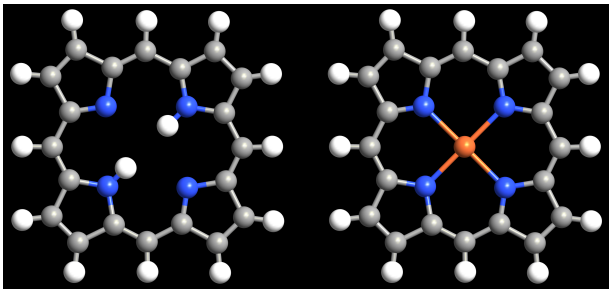

Figure 1.1: The structure of porphyrin, (left) a free-base ring and (right) with iron ion at the center.

offer, in principle, the possibility to build complex circuits with a bottom-up approach using this biological molecule as a building block. Obviously, the understanding of the electron transport in DNA molecules is a necessary prerequisite for the development of a DNA-based molecular electronics [16–19]. Modelling a device with the DNA molecule using first principles techniques is a very difficult task even with DNA samples of a short sequence. This difficulty arises from the fact that most of the computing algorithms used in DFT calculations scale with the number of electrons N considered in the system as $\mathcal{O}(N^3)$. For instance, a DNA molecule of sequence (ACGTACGT), shown in Figure 1.2, contains 528 atoms with 1512 orbitals and 1780 valence electrons. This indicates the size of the computer resources required to perform such calculations.

Other potential candidates that have been suggested to play central role in next generation of microelectronic fabrication are the two dimensional materials, especially graphene based systems. Since graphene was isolated [20], and the subsequent observation of its unusual electronic properties [21–23], graphene has captured the imagination of the scientific community.

Graphene is a single sheet of graphite in which the sp^2 hybridization leads to a trigonal planar structure with strong σ bonds connecting the in-plane carbon atoms with an equilibrium separation, a_{C-C}, of 1.42 Å. These in-plane covalent sp^2 bonds are among the strongest in nature (slightly stronger than the sp^3 bonds in diamond), with a bonding energy of approximately 5.9 eV [24]. By contrast, the adjacent graphene planes within a graphite crystal are linked by weak van der Waals interactions ($\sim$ 50 meV) [24] with a spacing of $\sim$ 3.35 Å [25]. This crystal structure gives rise to a unique electronic band structure and a whole range of interesting properties. Among these are:

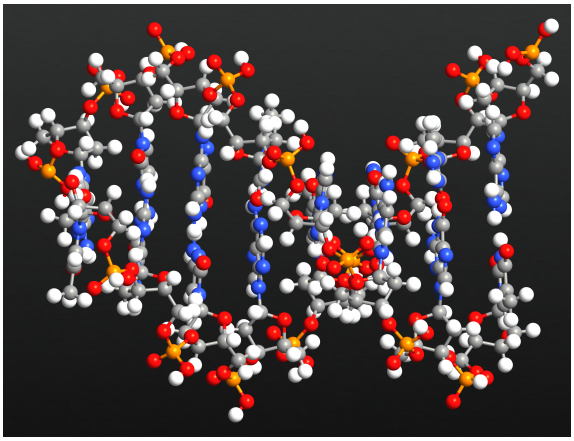

Figure 1.2: A DNA strand with ACGTACGT sequence.

1. The strength of C-C bonds result in a robust structure with a Young's modulus of 1 TPa [26]. This makes graphene 100 times stronger than a hypothetical steel film of the same thickness.

2. The thermal conductivity of graphene at room temperature is among the highest of any known material, about (2000−4000 $Wm^{-1}K^{-1}$) for freely suspended samples [27–29].

3. Graphene's uncommon optical properties give an unexpectedly high opacity for an atomic monolayer in vacuum, absorbing $\pi\alpha_f \approx \frac{3.14}{137} = 2.3\%$ of white light, where α_f is the fine structure constant [30].

4. Experimental measurements have shown that graphene has a remarkably high electron mobility at room temperature, with reported values in excess 15,000 $cm^2V^{-1}s^{-1}$ [22].

These exceptional properties offer a huge advantage in incorporating graphene in future applications. It is expected that graphene based materials will be important in a wide range of areas. This will include, high-speed electronic [31], optical devices [32], energy generation and storage [33–35], hybrid materials [36, 37], DNA sequencing [38–40], and chemical sensors [41].

The semi-metallicity of pristine graphene due to its zero band gap makes it impossible to fabricate logical circuits operated at room temperature with low standby power dissipation. The result is a small current on/off ratio in graphene field-effect transistors (FETs) [42]. Opening a band gap, therefore, is a fundamental step

towards creating semiconducting graphene that is to be incorporated in electronic industry. Several methods have been proposed to accomplish this goal, such as graphene nanoribbons (GNRs) [43–49], graphene grain boundaries (GGBs) [26, 50–68], and graphene nanomeshes (GNMs) [69–78].

GNRs are sheets of graphene that are cut to make ribbons. They have two basic edge shapes which determine the properties of graphene ribbons: zigzag and armchair. The corresponding ribbons are termed zigzag nanoribbons (ZGNRs) or armchair nanoribbons (AGNRs). The presence of these edges in graphene has strong effects on the band structure of graphene at low energies [43, 44, 79]. It has been shown that ribbons with zigzag edges possess localized edge states with energies close to the Fermi level. In contrast, edge states are absent for ribbons with armchair edges. By making such ribbons, the movement of charge carriers is restricted to one dimension rather than two in graphene. This quantum confinement modifies the linear energy dispersion near the Dirac points leading to open a gap.

In order to incorporate graphene in future industrial applications, it requires producing single crystals on a large scale. The most commonly employed method to fabricate large-scale graphene is the chemical vapor deposition (CVD) method [80, 81]. This relatively cheap and simple method has been used successfully to produce extremely large sheets of graphene (up to 30 inches) which can be transfered to other substrates [81]. However, the graphene samples synthesized by CVD or some other method is unavoidably polycrystalline where multi single crystals are stitched together to form the entire sheet (Figure 1.3). The interface between the two adjacent single crystal is termed a grain boundary (GB). The GBs and other topological defects in graphene have a significant impact on the electronic properties of graphene. Understanding how these defects affect the transport properties in graphene is crucial in developing reliable techniques to help produce large-scale graphene with controllable electronic transport features.

The graphene nanomesh is another concept of defect engineering used to open and tune a band gap in pristine graphene. This method was first proposed by Pedersen *et al.* [69] and has been subsequently realized experimentally by Bai *et al.* [70] and Akhavan [71].

Recently, there has also been strong interest in group-IV graphene-like 2D nanosheets.

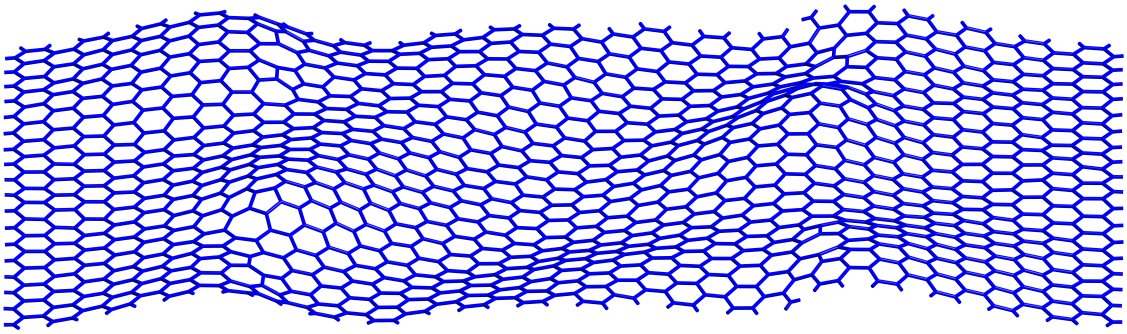

Figure 1.3: An optimized structure of the (17,2)|(18,0) grain boundary supercell which contains 1368 carbon atoms with length and width of 7.93 nm and 4.41 nm respectively.

Silicene and germanene, the silicon and germanium based counterparts of graphene, have progressed from theoretical predications [82] to experimental observations [83] in only few years. They are found to exhibit electronic characteristics similar to graphene [84]. Indeed graphene-like silicene based technologies might have the major advantage of easy integration into existing circuitry because Si is currently the basis of most of the electronics industry.

Other examples of 2D sheets are molybdenum disulfide MoS_2 and hexagonal boron nitride *h*-BN. A single layer of MoS_2 shows a semi-conducting behaviour with a direct band gap of ($\sim$ 1.9 eV) [85]. This makes MoS_2 a promising material that has the potential to be incorporated into digital circuits [86, 87] and light-emitting diodes [88]. For instance, the current on/off ratio of single-layer MoS_2 transistors exceeds 108 at room temperature [89] which is much higher than that ($\sim$ 100) of graphene transistors [20]. A monolayer of *h*-BN exhibits a band gap of ($\sim$ 6.1 eV) as measured by Kim *et al.* [90]. While a theoretical study expects that the band gap can be reduced by a factor of half if the *h*-BN is fully hydrogenized [91].

In this thesis, we have focused on two classes of systems: molecular quantum wires and structures based on graphene sheets. The aim has been to investigate the various factors that contribute to or affect the conductance across these systems. For molecular wires, the main issues are related to the contact geometry, the length and structure of the wires and finally the environment which is principally dependent on the solution around the wires.

For the graphene based systems, as already referred, the aim is to construct structures that open up a band gap in its electronic bands structure. To this end, various

graphene based systems have been studied, including GNRs, GBs in graphene sheets and graphene nanomeshes.

The methodology used was the semi-empirical EHT approach as it provides the most effective and accurate way of performing the large scale computations. At all stages, DFT calculations were carried out in order to check the accuracy of the EHT results for smaller systems. We have used the EHTransport code, which was developed at Cardiff University by Gareth Jones and written in C++ [92].

The thesis comprises nine chapters. Chapter Two is devoted to presenting an overview of the most common methods employed to calculate the electronic structure of materials. A basic introduction to density functional theory and extended Hückel theory is provided. Also an overview of the DFT-SIESTA package and EHT-EHTransport code are presented in the same Chapter. The theoretical details of non-equilibrium Green's functions (NEGFs) formalism are reported in Chapter Three. It starts by presenting the one level model and ends with a derivation of an expression for the electric current flowing through a system in between two contacts. In Chapter Four, we have examined the reliability of the EHTransport code by comparing its outcomes with that of SIESTA for porphyrin molecules. In Chapter Five, we applied the EHTransport code to investigate the factors that affect the electrical conductance of DNA systems. Exploration of the graphene based systems starts in Chapter Six by studying the characteristics of one dimensional graphene nanoribbons. While Chapter Seven focuses on research on the electronic structure and transport properties of grain boundaries in graphene. In Chapter Eight, the two dimensional sheets of graphene with periodically punched nanoholes are scrutinized. The concluding Chapter gives a summary of the work carried out and lists the conclusions of the present thesis. In addition, we point to further work that could be done with current version of the EHTransport code. Possible developmental steps to extend the ability of the code are also discussed.

CHAPTER 2

ELECTRONIC STRUCTURE CALCULATION METHODS

2.1 Introduction

Unavailability of analytical solutions for the problems of solid state physics, except for the very simple systems like hydrogen atom, makes numerical techniques the only way to adopt in finding solutions to these problems. The main interest of this field is finding the electronic structure of solids which is also the concern of this study. Accordingly, the natural point to commence from is the Schrödinger equation which is a second-order differential equation. Actually, various numerical approaches are available which are used to solve this kind of equations such as finite differences and finite elements. However, the presence of huge number of the particles that are involved in most solid state physics' problems, makes applying these tools impossible in practice. As a result, approximate theories are needed. The implementation of these approximations theories turns the problem of many particles to be tractable and can be solved by means of using current available computer resources. In fact, different types and accuracy levels of approximation are used, for example, considering the massive nuclei at rest in comparison with the light electrons, neglecting the electron-electron interaction, etc... . Most of the complex terms that are removed from the original problem can be handled by using experimental data and/or theoretical based models. Unfortunately, no universal approach is available to be generalized to all cases. The reason behind that is simply that each situation demands particular arrangements. In fact, two main categories of approximate computing methods are in use to study the electronic structures: *ab initio* and tight binding methods. In *ab initio* methods, the

calculations do not involve using any experimental data. Instead of that, all the physical quantities are computed using first principles of quantum mechanics. On the other hand, tight binding methods use parameter sets that are obtained by matching between experimental and theoretical data.

2.2 Density functional theory

Density Functional Theory (DFT) [93, 94] is one of the most popular *ab initio* methods which is interested in the total electronic density at each point in space, rather than attempting to obtain the many-particle wavefunction directly. We will start this review of DFT by following the approach of ref. [95]. The ultimate goal of most theoretical approaches in solid state physics is to solve the time-independent, non-relativistic Schrödinger equation

$$\hat{H}\Psi(\vec{r}_1,...,\vec{r}_N,\vec{R}_1,...,\vec{R}_M) = E_T\Psi(\vec{r}_1,...,\vec{r}_N,\vec{R}_1,...,\vec{R}_M) \tag{2.1}$$

where $\hat{H}$ is the Hamiltonian of a system containing N electrons and M nuclei. Ψ is the many-particle wave function which depends on the electron and nuclei positions $\vec{r}_i$ and $\vec{R}_i$ respectively, and E_T is the total energy of the system. If the system does not experience any external fields, the Hamiltonian $\hat{H}$ takes the following form:

$$\begin{aligned}\hat{H} = -\frac{\hbar^2}{2m_e}\sum_i^N \nabla_i^2 - \sum_I^M \frac{\hbar^2}{2m_I}\nabla_I^2 - \sum_{i=1}^N\sum_{I=1}^M \frac{Z_I e^2}{|\vec{r}_i - \vec{R}_I|} \\ + \sum_{i=1}^N\sum_{j>i}^N \frac{e^2}{|\vec{r}_i - \vec{r}_j|} + \sum_{I=1}^M\sum_{J>I}^M \frac{Z_I Z_J e^2}{|\vec{R}_I - \vec{R}_J|}\end{aligned} \tag{2.2}$$

Here, the first two terms are the kinetic energy of the electrons with mass m_e and nuclei with mass M_I respectively. The other three terms represent, respectively, the attractive electrostatic interaction between the nuclei and the electrons, repulsive potential due to the electron-electron and nucleus-nucleus interactions. Solving the Schrödinger equation with the Hamiltonian given by equation (2.2) is impossible either analytically or numerically. For this reason making appropriate assumptions is essential to reduce the complexity of the problem at hand. The first step towards simplifying the Hamiltonian form is using the Born-Oppenheimer approximation [96]. Due to the fact

that the nuclei are much heavier than the electrons, they move much more slowly than the electrons. This means that the nuclear kinetic energy can be ignored and we can think of the electrons as moving through an effectively field of fixed nuclei. So, the Schrödinger equation is solved for the electrons in the system, ignoring the motion of the ions. The Hamiltonian for the electrons is then obtained by removing the second and last term from equation (2.2), so that

$$\begin{aligned}\hat{H}_e &= -\frac{\hbar^2}{2m_e}\sum_i^N \nabla_i^2 - \sum_{i=1}^N\sum_{I=1}^M \frac{Z_I e^2}{|\vec{r}_i - \vec{R}_I|} + \sum_{i=1}^N\sum_{j>i}^N \frac{e^2}{|\vec{r}_i - \vec{r}_j|} \\ &= \hat{T}_e + \hat{V}_{Ne} + \hat{V}_{ee} \end{aligned} \tag{2.3}$$

The result of applying the Born-Oppenheimer approximation is to separate the nuclei and electron motions. The many particle wave function, $\Psi(\vec{r}_1,...,\vec{r}_N,\vec{R}_1,...,\vec{R}_M)$, is written as a product of the many electron wave function, $\Psi_e(\vec{r}_1,...,\vec{r}_N)$ and the many ion wavefunction Ψ_I. Hence, equation (2.1) for the electrons can be re-written as

$$\hat{H}_e\Psi_e = E_e\Psi_e \tag{2.4a}$$

or

$$\left(\hat{T}_e + \hat{V}_{Ne} + \hat{V}_{ee}\right)\Psi_e = E_e\Psi_e \tag{2.4b}$$

where E_e is the electronic energy and the total energy of the system is then given as the sum of E_e and a constant term represents the repulsion between nuclei. Hence employing the Born-Oppenheimer approximation reduces the complexity of equation (2.1). However, even equation (2.4) is generally unsolvable [1]. To obtain an estimate of the electron energies, the variational principle is applied. For a system in quantum state Ψ, the expectation value of the energy is given by

$$E[\Psi] = \frac{\langle\Psi|\hat{H}|\Psi\rangle}{\langle\Psi|\Psi\rangle} \tag{2.5}$$

To get the lowest energy state, we apply the variational principle which states that the

[1] From now on the subscript 'e' will be dropped.

energy calculated by using a trial wavefunction $\tilde{\Psi}$ is an upper bound to the real ground state energy E_0. This can be expressed mathematically as follows:

$$E_0 = \min_{\Psi \to N} E[\Psi] = \min_{\Psi \to N} \langle \Psi | \hat{T} + \hat{V}_{Ne} + \hat{V}_{ee} | \Psi \rangle \tag{2.6}$$

where $\Psi \to N$ indicates that Ψ is an allowed wavefunction describing a system of N electrons. The question then arises, "What is the form of the proposed ground state wavefunction?". In the Hartree-Fock approximation, the ground state wavefunction Ψ_0 is defined as a Slater determinant

$$\Psi_0 \approx \Psi_{HF} = \frac{1}{\sqrt{N!}} \begin{vmatrix} \phi_1(\vec{r}_1) & \cdots & \phi_i(\vec{r}_1) & \cdots & \phi_N(\vec{r}_1) \\ \phi_1(\vec{r}_2) & \cdots & \phi_i(\vec{r}_2) & \cdots & \phi_N(\vec{r}_2) \\ \vdots & & \vdots & & \vdots \\ \phi_1(\vec{r}_N) & \cdots & \phi_i(\vec{r}_N) & \cdots & \phi_N(\vec{r}_N) \end{vmatrix} \tag{2.7}$$

The minimization of the energy functional (to get energy of of ground state E_0) and using Slater determinant as an approximation to the ground state wavefunction lead (Ψ_0) to what are called Hartree-Fock differential equations:

$$\hat{F}\phi_i = \epsilon_i \phi_i, \quad i = 1, 2, ..., N \tag{2.8}$$

This set of N equations has the form of an eigenvalue equation in which ϵ_i are the eigenvalues of the operator $\hat{F}$ which is an effective one-electron operator that is defined as:

$$\hat{F} = -\frac{\hbar^2}{2m_e}\nabla_i^2 - \sum_A^M \frac{e^2 Z_A}{r_{iA}} + V_{HF}(i) \tag{2.9}$$

The first two terms are the kinetic energy and the potential energy due to the electron-nucleus attraction. $V_{HF}(i)$ is the Hartree-Fock potential, the average repulsive potential experienced by the i^{th} electron due to the remaining $(N-1)$ electrons.

2.2.1 The Hohenberg-Kohn Theorems

The corner stone of the DFT as it is known today is the the so-called Hohenberg-Kohn Theorems published in 1964 [94]. The first Hohenberg-Kohn theorem states that the

electron density is uniquely determined by the Hamiltonian operator and thus so are all the properties of the system. This implies that the external potential $V_{ext}(\vec{r})$ is (to within a constant) a unique functional of electronic density $\rho(\vec{r})$. As the external potential $V_{ext}(\vec{r})$ specifies the whole Hamiltonian, the full many particle ground state is a unique functional of electron density $\rho(\vec{r})$. Thus, $\rho(\vec{r})$ determines the number of electrons N and the external potential $V_{ext}(\vec{r})$ and consequently all the properties of the ground state. The total energy functional $E[\rho]$ can be written as,

$$E[\rho] = \int \rho(\vec{r}) V_{ext}(\vec{r}) d\vec{r} + F_{HK}[\rho] \tag{2.10}$$

where

$$F_{HK}[\rho] = T[\rho] + E_{ee}[\rho] \tag{2.11}$$

The first term in equation (2.10) represents the potential energy due to the electron-nuclei interaction, and $F_{HK}[\rho]$ is an unknown, but otherwise universal functional of the electron density $\rho(\vec{r})$ only. If it was known, the solubility of Schrödinger equation would be possible for any system. The $F_{HK}[\rho]$ functional consists of a kinetic energy functional $T[\rho]$ and electron-electron repulsive interaction functional $E_{ee}[\rho]$.

The second Hohenberg-Kohn theorem is nothing more than the variational principle. It states that the electronic density that minimises the total energy is the exact ground state density. That is for a trial density $\tilde{\rho}(\vec{r})$, we have

$$E_0 \leq E[\tilde{\rho}(\vec{r})] = T[\tilde{\rho}] + \int \tilde{\rho}(\vec{r}) V_{ext}(\vec{r}) d\vec{r} + E_{ee}[\rho] \tag{2.12}$$

which means that the energy resulting from equation (2.10), using the trial density $\tilde{\rho}(\vec{r})$, represents an upper bound to the true ground state energy E_0. E_0 is the outcome if and only if the exact ground state density is used in equation (2.12).

2.2.2 The Kohn-Sham Theory

It has been shown that the ground state energy of a system is given as

$$E_0 = \min_{\rho \to N} \left(\int \rho(\vec{r}) V_{ext}(\vec{r}) d\vec{r} + F_{HK}[\rho] \right) \tag{2.13}$$

where the functional $F_{HK}[\rho]$ can be defined as

$$\begin{aligned} F_{HK}[\rho] &= T[\rho] + E_{ee}[\rho] \\ &= T[\rho] + J[\rho] + E_{nc}[\rho] \end{aligned} \tag{2.14}$$

where $T[\rho]$, $J[\rho]$, and $E_{nc}[\rho]$ are respectively the kinetic energy, the classical Coulomb interaction and the non-classical functional. Of these functionals, only $J[\rho]$ is known and is given by

$$J[\rho] = \frac{1}{2}\iint \frac{\rho(\vec{r}_1)\rho(\vec{r}_2)}{|\vec{r}_1 - \vec{r}_2|} d\vec{r}_1 d\vec{r}_2 \tag{2.15}$$

The main goal now is to find the forms of $T[\rho]$ and $E_{nc}[\rho]$. The Kohn-Sham theorem provides an effective way to express these two functionals. The idea of the Kohn-Sham approach is to use the kinetic energy of a fictitious non-interacting system T_s with the same electronic density as the real interacting one instead of the true kinetic energy $T[\rho]$, where

$$T_s = -\frac{\hbar^2}{2m}\sum_i^N \langle \psi_i | \nabla^2 | \psi_i \rangle \tag{2.16}$$

and

$$\rho_s(\vec{r}) = \sum_i^N \sum_\varsigma |\psi_i(\vec{r}, \varsigma)|^2 = \rho(\vec{r}) \tag{2.17}$$

$\psi_i(\vec{r}, \varsigma)$ are then the spin-orbital wave functions of the fictitious non-interacting system. Certainly, the two kinetic energies of the real and fictitious system are different, however, this difference is taken into account by introducing a new functional called exchange-correlation energy which contains everything that is unknown for us. Hence the functional $F_{HK}[\rho]$ takes the following new form

$$F_{HK}[\rho] = T_s[\rho] + J[\rho] + E_{XC}[\rho] \tag{2.18}$$

and

$$\begin{aligned} E_{XC}[\rho] &= T[\rho] - T_s[\rho] + \Big(E_{ee}[\rho] - J[\rho]\Big) \\ &= T[\rho] - T_s[\rho] + E_{nc}[\rho] \end{aligned} \tag{2.19}$$

Calculating the $T_s[\rho]$ requires knowing the orbitals ψ_i of the non-interacting system. This takes us to search for the potential that delivers a Slater determinant which is characterized by the same density as the real system. This can be done by re-writing equation (2.10) with using equation (2.18) to get

$$E[\rho] = \int \rho(\vec{r}) V_{ext}(\vec{r}) d\vec{r} + T_s[\rho] + J[\rho] + E_{XC}[\rho] \tag{2.20}$$

Using equations (2.15) through (2.18) in (2.20) and applying the variational principle [95] gives the following set of Kohn-Sham equations:

$$\left(-\frac{\hbar^2}{2m} + V_{eff}(\vec{r}_1)\right)\psi_i = \varepsilon_i \psi_i \tag{2.21}$$

where the effective potential $V_{eff}(\vec{r}_1)$ is given by

$$V_{eff}(\vec{r}_1) = \int \frac{\rho(\vec{r}_2)}{|\vec{r}_1 - \vec{r}_2|} d\vec{r}_2 + V_{XC}(\vec{r}_1) - \sum_A^M \frac{Z_A e^2}{|\vec{r}_1 - \vec{r}_A|} \tag{2.22}$$

The second term in V_{eff} represents the exchange-correlation potential and defined as the derivative of energy functional with respect to electronic density, i.e.

$$V_{XC} = \frac{\delta E_{XC}}{\delta \rho} \tag{2.23}$$

Knowing the three terms in equation (2.22), determines the potential V_{eff} which consequently determines the energy and electronic density of the ground state. As the potential V_{eff} depends on density, the Kohn-Sham equations have to be solved iteratively. It is worth pointing out that if the exact forms of E_{XC} and V_{XC} were known, the Kohn-Sham approach would lead to the exact ground state energy. Unfortunately, these functionals have unknown forms and using the Kohn-Sham in practice requires finding reasonable approximations first for the exchange-correlation functionals.

2.2.3 The exchange-correlation functionals

2.2.3.1 The local density approximation LDA

The first expression for the exchange-correlation functional E_{XC} was originally derived to describe the exchange effects in a homogeneous electron gas (HEG) without DFT in mind. In HEG, the electrons move in the presence of a background of positive charge which ensures the overall charge neutrality of the system. As the exchange energy of a HEG depends upon the local value of electronic density, the term "local density approximation (LDA)" is used to refer to those functionals based on HEG. The LDA is the basis of all approximate exchange-correlation functionals. According to LDA, the energy functional E_{XC} can be expressed in the form

$$E_{XC}[\rho] = \int \rho(\vec{r})\epsilon_{XC}([\rho],\vec{r})d\vec{r} \tag{2.24}$$

where $\epsilon_{XC}([\rho],\vec{r})$ is the exchange-correlation energy per electron, at position $(\vec{r})$, of a uniform electron gas of density $\rho(\vec{r})$. For the unpolarized system, this energy depends only on the value of electronic density in some neighborhood of position $(\vec{r})$. The quantity ϵ_{XC} can be partitioned into two parts, termed the exchange and correlation contributions as follows

$$\epsilon_{XC}([\rho],\vec{r}) = \epsilon_X[\rho] + \epsilon_C[\rho] \tag{2.25}$$

The first term, derived by Bloch in 1929 [97], is given by

$$\epsilon_X = -\frac{3}{4}\left(\frac{3\rho(\vec{r})}{\pi}\right)^{1/3} \tag{2.26}$$

No such explicit expression is available for the correlation term, ϵ_C, except for some limited cases. For instance, expressions for ϵ_C have been derived in both the low and high density limits (or when the electronic density approaches zero or infinity) [98, 99]. However, various analytical expressions have been since obtained for intermediate densities using interpolations of accurate numerical results of calculations made by Ceperley and Alder, who used a quantum Monte Carlo simulations of the HEG [100].

One of these expressions, as proposed by Perdew and Wang (PW) [101], is

$$\epsilon_C^{PW} = -2A(1+\alpha_1 r_s)\ln\left[1+\frac{1}{2A\left(\beta_1 r_s^{1/2}+\beta_2 r_s+\beta_3 r_s^{3/2}+\beta_4 r_s^2\right)}\right] \tag{2.27}$$

where $A = 0.031091$, $\alpha_1 = 0.21370$, $\beta_1 = 7.5957$, $\beta_2 = 3.5876$, $\beta_3 = 1.6382$, $\beta_4 = 0.49294$, and r_s represents the density parameter which is given by

$$r_s = \left(\frac{3}{4\pi\rho}\right)^{1/3} \tag{2.28}$$

In fact, r_s characterizes the density and is defined as the radius of a sphere containing one electron on average in HEG with density ρ. Thus it is a measure of the average distance between electrons.

More general versions of LDA have been developed to take into account the systems with unbalanced spin population of states, i.e. polarized systems. In this extended version, which is known as local spin-density approximation (LSDA), the exchange-correlation functional E_{XC} has spin dependency form in addition to the spatial one. Introducing the electron density of spin up, $\rho_\uparrow(\vec{r})$, and down, $\rho_\downarrow(\vec{r})$ states with $\rho(\vec{r}) = \rho_\uparrow(\vec{r}) + \rho_\downarrow(\vec{r})$, equation (2.24) now reads

$$E_{XC}^{LSDA}[\rho_\uparrow,\rho_\downarrow] = \int \rho(\vec{r})\epsilon_{XC}(\rho_\uparrow,\rho_\downarrow,\vec{r})d\vec{r} \tag{2.29}$$

2.2.3.2 The generalized gradient approximation GGA

An inspection of the LDA functional shows that it is only the first term in an expansion of the exchange-correlation energy in terms of the gradient of the density. A more systematic way to extend the ability of the LDA functional is to include nonlocal corrections by adding additional terms from this expansion. This means constructing a functional that depends not only on the value of the density ρ at each point in space but also upon the magnitude of gradient of the density $|\nabla\rho|$. This new functional is known as gradient expansion approximation GEA and was originally proposed by Kohn and Sham [102] and used later by Herman *et al.* [103]. However, the GEA does not lead to consistent improvement over LDA and sometimes produces worse results than the LDA. There are various sum rules that must be satisfied by the true exchange-correlation

functional, such as the fact that the exchange hole should displace exactly one electron. The basic problem is that gradients in real materials are so large that the expansion breaks down. To solve this problem, generalized gradient approximations (GGA) were designed [104]. The basic idea of GGA is employing functionals that tame the behavior at large gradients while still preserving the desired properties of sum rules. The exchange-correlation functional within the framework of the GGA can be written as

$$E_{XC}^{GGA}[\rho_\uparrow,\rho_\downarrow] = \int f(\rho_\uparrow,\rho_\downarrow,|\nabla\rho_\downarrow|,|\nabla\rho_\uparrow|,...)d\vec{r} \tag{2.30}$$

where the function f is chosen according to some criteria and a variety of different forms are proposed and employed in the literature for it.

$$\begin{aligned} E_{XC}^{GGA}[\rho_\uparrow,\rho_\downarrow] &= \int \rho(\vec{r})\epsilon_{XC}(\rho_\uparrow,\rho_\downarrow,|\nabla\rho_\downarrow|,|\nabla\rho_\uparrow|,...)d\vec{r} \\ &\equiv \int \rho(\vec{r})\epsilon_X^{hom}(\rho)F_{XC}(\rho_\uparrow,\rho_\downarrow,|\nabla\rho_\downarrow|,|\nabla\rho_\uparrow|,...)d\vec{r} \end{aligned} \tag{2.31}$$

where F_{XC} is dimensionless quantity known as the exchange-correlation enhancement factor, and ϵ_X^{hom} is the exchange energy of the unpolarized HEG given in equation (2.26). For the exchange term, it can be proved that [105]

$$E_X[\rho_\uparrow,\rho_\downarrow] = \frac{1}{2}\Big(E_X[2\rho_\uparrow] + E_X[2\rho_\downarrow]\Big) \tag{2.32}$$

where $E_X[\rho]$ is the exchange energy for an unpolarized system of density ρ. Hence, the spin-unpolarized factor $F_X(\rho,|\nabla\rho_\uparrow|)$ is only to be considered in the case of the exchange energy. An analytical expression for the F_X has been formulated

$$F_X = 1 + \frac{10}{81}s_1^2 + \frac{146}{2025}s_2^2 + ... \tag{2.33}$$

where s_m is a dimensionless quantity given by

$$s_m = \frac{|\nabla^m\rho|}{\rho(2k_F)^m} = \frac{|\nabla^m\rho|}{2^m(3\pi^2)^{m/3}\rho^{1+m/3}} \tag{2.34}$$

with the Fermi wavevector $k_F = \sqrt[3]{3\pi^2\rho} = \sqrt[3]{18\pi}/r_s$.

A variety of different forms for $F_X(n,s)$, where $s = s_1$, have been proposed and three

of the most widely employed ones in the literature are illustrated in Figure 2.1. The (B88) form was proposed by Becke in 1988, which was followed by the formulation of Perdew and Wang (PW91), and Perdew, Burke, and Enzerhof [106, 107]. The later was revised three years later by Hammer *et al.* [108]. Generalization of these functions falls between B88 and PBE curves [109]. For more details, see ref. [110] where a very interesting analysis of the GGAs is provided.

The correlation energy is more difficult to cast in terms of a functional, but its contribution to the total energy is typically much smaller than the exchange. For large density gradients the magnitude of the correlation energy decreases and vanishes as $s_1 \to \infty$. This decrease can be qualitatively understood since large gradients are associated with strong confining potentials that increase level spacings and reduce the effect of interactions compared to the independent-electron terms.

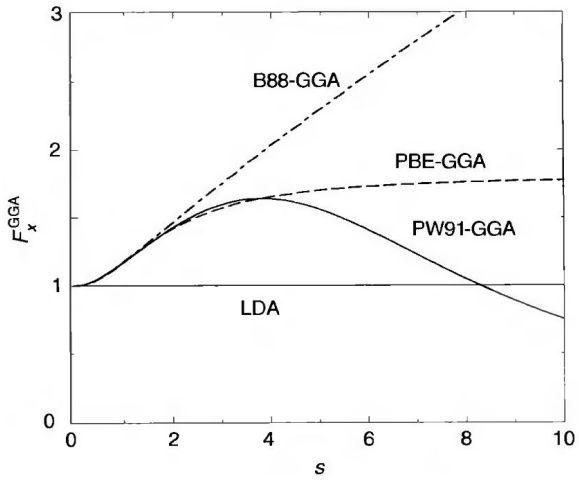

Figure 2.1: Exchange enhancement factor F_X as a function of the dimensionless density gradient s for various GGAs. (Adopted from ref. [111])

2.2.3.3 Hybrid functionals

Usually the exchange contributions are significantly larger than the corresponding correlation effects. Therefore, an accurate expression for the exchange functional is a prerequisite for obtaining meaningful results from density functional theory. In this sense, it is important to note that the exchange energy of a Slater determinant can be computed exactly. This fact has motivated the construction of what is called hybrid functionals because they are a combination of orbital-dependent Hartree-Fock and an explicit density functional. These are the most accurate functionals available as far as

energetics is concerned and are the method of choice in the chemistry community. The hybrid functionals differ in the way in which the exchange HF energy is mixed with the exchange-correlation energy of a density functional. Becke [112] argued that the total exchange-correlation energy can be approximated by

$$E_{XC} = \frac{E_X^{HF} + E_{XC}^{DFA}}{2}, \tag{2.35}$$

where DFA denotes an LDA or GGA functional. Later Becke presented parameterized forms that are accurate for many molecules, such as “B3P91" [112, 113], a three-parameter functional that mixes Hartree-Fock exchange, the exchange functional of Becke (B88), and the correlation of Perdew and Wang (PW91). Currently the most popular hybrid functional is the so called B3LYP [2] that uses LYP correlation functional [114]. In this case the definition of the exchange-correlation energy is

$$E_{XC} = E_{XC}^{LDA} + a_0 \left[E_X^{HF} - E_X^{DFA}\right] + a_X E_{XC}^{Becke} + a_C E_C \tag{2.36}$$

where the coefficients a_i are empirically adjusted to fit atomic and molecular data.

2.2.4 The pseudopotential method

The fundamental idea of a “pseudopotential" is the replacement of one problem with another. The primary application in electronic structure is to replace the strong Coulomb potential of the nucleus and the effects of the tightly bound core electrons by an effective ionic potential acting on the valence electrons. A pseudopotential can be generated in an atomic calculation and then used to compute properties of valence electrons in molecules or solids, since the core states remain almost unchanged. Furthermore, the fact that pseudopotentials are not unique allows the freedom to choose forms that simplify the calculations and the interpretation of the resulting electronic structure. The advent of “ab initio norm-conserving" and “ultrasoft" pseudopotentials has led to accurate calculations that are the basis for much of the current research and development of new methods in electronic structure [105].

Most modern pseudopotential calculations are based upon ab initio norm-conserving

[2] B3LYP stands for Becke, 3-parameter, and Lee-Yang-Parr.

potentials. The requirement of norm-conservation is the key step in making accurate, transferable pseudopotentials, which is essential so that a pseudopotential constructed in one environment (usually the atom) can faithfully describe the valence properties in different environments including atoms, ions, molecules, and condensed matter.

Pseudopotentials generated by calculations on atoms (or atomic-like states) are termed “ab initio" because they are not fitted to experiment. The concept of norm-conservation has a special place in the development of ab initio pseudopotentials; at one stroke it simplifies the application of the pseudopotentials and it makes them more accurate and transferable. Quantum chemists and physicists have devised pseudopotentials called, respectively, shape-consistent [115, 116] and norm-conserving [117]. The starting point for defining norm-conserving potentials is the list of requirements for a good ab initio pseudopotential given by Hamann, Schluter, and Chiang (HSC) [117]:

1. All-electron and pseudo valence eigenvalues agree for the chosen atomic reference configuration.

2. All-electron and pseudo valence wavefunctions agree beyond a chosen core radius R_c.

3. The logarithmic derivatives of the all-electron and pseudo wavefunctions agree at R_c.

4. The integrated charge inside R_c for each wavefunction agrees (norm-conservation).

5. The first energy derivative of the logarithmic derivatives of the all-electron and pseudo wavefunctions agrees at R_c.

From points 1 and 2, it follows that the norm-conserving pseudopotential equals the atomic potential outside the core region of radius R_c; this is because the potential is uniquely determined (except for a constant that is fixed if the potential is zero at infinity) by the wavefunction and the energy ε, that need not be an eigenenergy. Point 3 follows since the wavefunction $\psi_l(r)$ and its radial derivative $\psi_l^{'}(r)$ are continuous at R_c for any smooth potential. The dimensionless logarithmic derivative D is defined by

$$D_l(\epsilon, r) \equiv \frac{r\psi_l^{'}(\epsilon, r)}{\psi_l(\epsilon, r)} = r\frac{\mathrm{d}}{\mathrm{d}r}\ln\psi_l(\epsilon, r) \tag{2.37}$$

Inside the core region the pseudopotential and radial pseudo-orbital ψ_l^{PS} differ from their all-electron counterparts; however, point 4 requires that the integrated charge,

$$Q_l = \int_0^{R_c} r^2 |\psi_l(r)|^2 \mathrm{d}r, \tag{2.38}$$

is the same for ψ_l^{PS} as for the all-electron radial orbital ψ_l^{AE} for a valence state. The conservation of Q_l insures that the total charge in the core region is correct, and the normalized pseudo-orbital is equal to the true orbital outside of R_c (equality can be strictly enforced only for local functionals).

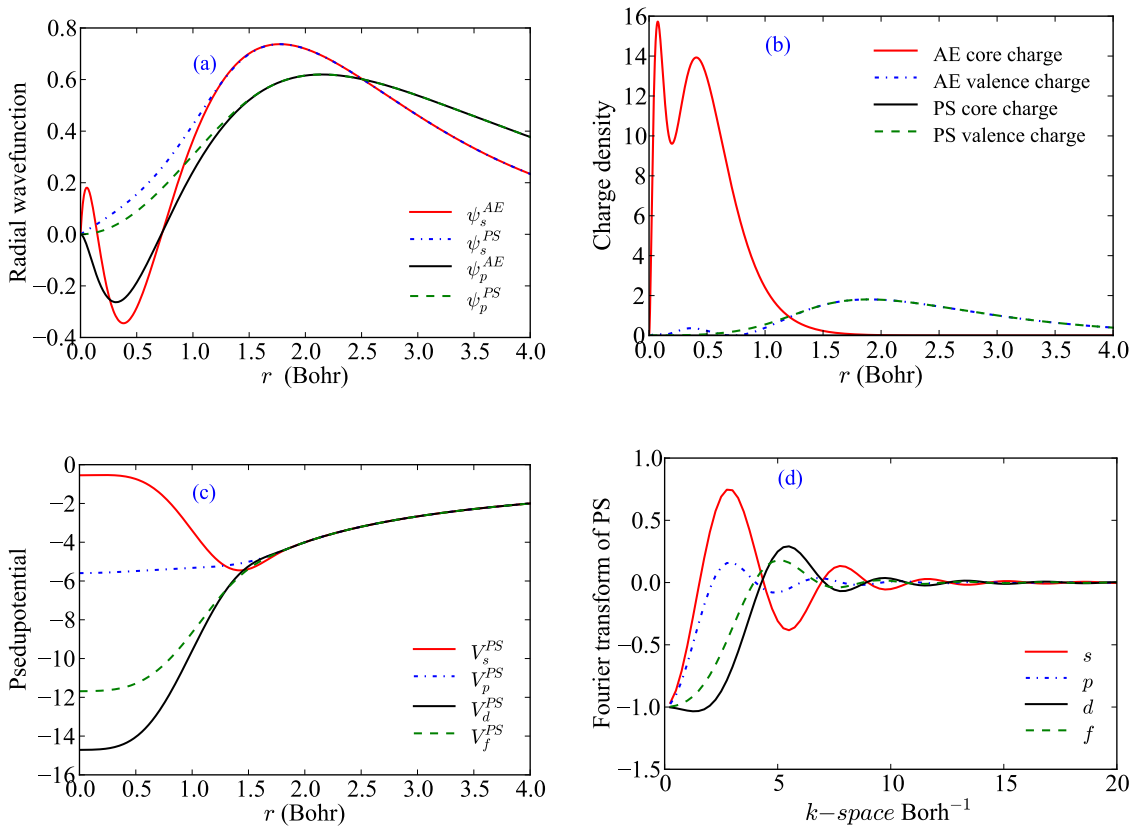

Figure 2.2: The wave functions, charge density, pseudopotetials and their Fourier transform for silicon. (a) Comparison of the radial all electron and pseudo wave function of s and p orbitals. (b) The valence and core charge density for all electron and pseudopotentials. (c) The real space representation of the pseudopotentials for the s, p, d, and f orbitals, and (d) their corresponding Fourier transform. These graphs were calculated using ATOM utility built-in SIESTA package (section 3.5) where Troullier-Martins scheme and LDA with Ceperley-Alder exchange-correlation flavour were implemented.

2.3 The tight binding model

The tight binding model (TBM) is one of the many methods used to solve for the electronic structure in molecules and solids. It was first proposed by Bloch [118] in 1929. The TB model is primarily suited to description of low-lying narrow bands for which the shell radius is much smaller than the lattice constant. An example is the 3d band in transition metals. The spirit of TBM is expressing the total wavefunction as a linear combination of atomic-like orbitals localized (centered) around the different atomic positions. Therefore, the TB is known as the linear combination of atomic orbitals (LCAO) method. In the TB model, the total potential through the crystal is assumed to be represented by the superposition of the individual atomic potentials. As the name suggests, the TB model supposes that the electrons bound tightly to the atom to which they belong. When an electron is captured by an ion during its motion through the lattice, it remains there for a long time before tunnelling to the next ion. During this capture, its state is essentially that of an atomic orbital for isolated atom, uninfluenced by the surrounding atoms. Moreover, the full periodic Hamiltonian of the crystal, in the vicinity of each lattice point, can be approximated by that of a single atom located at that lattice point with the Schrödinger equation

$$\hat{H}\Phi = E\Phi \tag{2.39}$$

The one-electron wavefunction Φ can be determined depending upon the system under study which can be either finite (isolated) such as a molecule or an infinite periodic system as crystallized materials. In the first case, the wavefunction can be expressed as

$$\Phi(\vec{r}) = \sum_{j\beta} c_{j\beta}\varphi_{\beta}(\vec{r} - \vec{R}_j) \tag{2.40}$$

where $c_{j\beta}$ are the expansion coefficients and $\varphi_{\beta}(\vec{r} - \vec{R}_j)$ represents the state that corresponds to the localized atomic orbital β that is centered around the atomic position $\vec{R}_j$. Substituting $\Phi(\vec{r})$ in equation (2.39) and multiplying it from left by $\Phi^*(\vec{r})$ yields the following set of equations for the coefficients c's

$$\sum_{i\alpha,j\beta} \left[\boldsymbol{H}_{i\alpha,j\beta} - E\boldsymbol{S}_{i\alpha,j\beta}\right] c_{i\alpha,j\beta} = 0 \tag{2.41}$$

where $\boldsymbol{S}_{i\alpha,j\beta}$ (the overlap between the orbitals φ_α and φ_β centered on $\vec{R}_i$ and $\vec{R}_j$) and $\boldsymbol{H}_{i\alpha,j\beta}$ are given respectively by

$$\boldsymbol{S}_{i\alpha,j\beta} = \int d\vec{r}\varphi^*_\alpha(\vec{r}-\vec{R}_i)\varphi_\beta(\vec{r}-\vec{R}_j) \tag{2.42}$$

and

$$\boldsymbol{H}_{i\alpha,j\beta} = \int d\vec{r}\varphi^*_\alpha(\vec{r}-\vec{R}_i)\hat{H}\varphi_\beta(\vec{r}-\vec{R}_j) \tag{2.43}$$

The set of equations (2.41) have non trivial solution if only

$$\left|\boldsymbol{H}-E\boldsymbol{S}\right| = 0 \tag{2.44}$$

The roots of this secular equation yield the eigenvalues (energy levels) of the finite system and the eigenfunctions are the corresponding wavefunctions (molecular orbitals) of the system. The dimension of the matrices in equation (2.44) is simply the total number of the orbitals employed in the calculation. In the case of a periodic system, the wavefunction is constructed using Bloch's theorem as follows

$$\Phi_{i\alpha}(\vec{k},\vec{r}) = \frac{1}{\sqrt{N}}\sum_l e^{i\vec{k}.\vec{R}_l}\varphi_\alpha(\vec{r}-\vec{R}_l-\vec{b}_i) \tag{2.45}$$

where N is the number of unit cells, $\varphi_\alpha(\vec{r}-\vec{R}_l-\vec{b}_i)$ is the atomic-like orbital of type α centered on the position $(\vec{R}_l+\vec{b}_i)$, and $\vec{R}_l$ is the position vector of the lattice point that associates with the l^{th} unit cell within which the position of i^{th} atom is defined by $\vec{b}_i$ as illustrated in Figure 2.3. Inserting the wavefunction $\Phi_{i\alpha}(\vec{k},\vec{r})$ in the Schrödinger equation leads to the following secular equation

$$\left|\boldsymbol{H}(\vec{k})-E\boldsymbol{S}(\vec{k})\right| = 0 \tag{2.46}$$

This eqaution differs from equation (2.44) as the former depends on the wave vector $\vec{k}$. The matrix elements of the overlap and Hamiltonian matrices are given by

$$\boldsymbol{S}_{i\alpha,j\beta}(\vec{k}) = \sum_l e^{i\vec{k}.\vec{R}_l}\int d\vec{r}\varphi^*_\alpha(\vec{r}-\vec{R}_l-\vec{b}_i)\varphi_\beta(\vec{r}-\vec{b}_j) \tag{2.47}$$

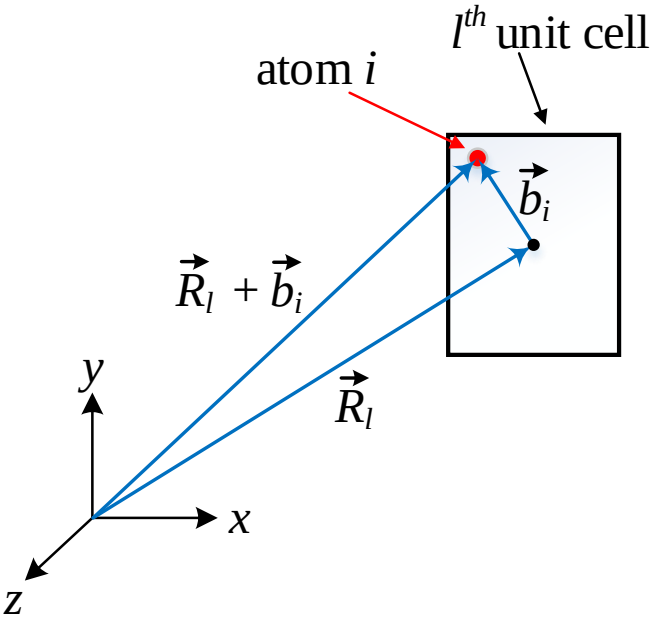

Figure 2.3: Schematic diagram shows how the vectors $\vec{r}$, $\vec{R}$ and $\vec{b}_i$ are related.

and

$$\boldsymbol{H}_{i\alpha,j\beta}(\vec{k}) = \sum_l e^{i\vec{k}.\vec{R}_l} \int d\vec{r}\varphi^*_\alpha(\vec{r}-\vec{R}_l-\vec{b}_i)\hat{H}\varphi_\beta(\vec{r}-\vec{b}_j) \tag{2.48}$$

Here the origin point of our coordinate system is fixed at some lattice point with adopting the unit cell associated to it as a reference unit. The element matrix $\boldsymbol{S}_{i\alpha,j\beta}(\vec{k})$ describes the overlap between the orbital α that belongs to atom i within the unit cell l and the orbital β of atom j in the reference unit cell as shown in Figure 2.4. It is clear that in the case of one unit cell, these equations are reduced to that of an isolated system where only the Γ point is considered. Obtaining the band structure $\epsilon_\mu(\vec{k})$ and the corresponding eigenvectors $\boldsymbol{Q}_\mu(\vec{k})$ of the periodic system requires solving the generalized eigenvalue problem (2.46) at each k-point in reciprocal space. An important quantity for many purpose is the density of states per unit energy. The partial density of states (PDOS) projected onto a given atom, orbital and spin (represented by the index v) is defined as follows:

$$\begin{aligned} PDOS_v(E) &= \frac{1}{N_k}\sum_{\vec{k},\mu}\left|\boldsymbol{Q}_{v,\mu}\right|^2\delta(\epsilon_\mu(\vec{k})-E) \\ &= \frac{\Omega_{cell}}{(2\pi)^d}\sum_\mu\int_{BZ}d\vec{k}\left|\boldsymbol{Q}_{v,\mu}\right|^2\delta(\epsilon_\mu(\vec{k})-E) \end{aligned} \tag{2.49}$$

where Ω_{cell} is the volume of the unit cell and d is the dimensionality of the system.

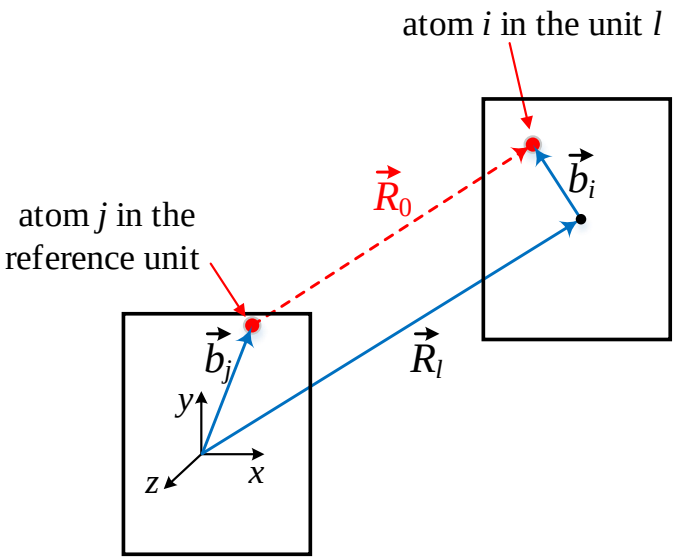

Figure 2.4: Schematic diagram shows how the position vectors are related in a periodic system.

2.3.1 Extended Hückel Theory

Extended Hückel Theory [119] (EHT) is the semi-empirical version of the tight binding method. As the name suggests, EHT is an extension of an earlier (non-extended) Hückel theory (NEHT). The latter was developed by Erich Hückel [120–123] in 1930s as linear combination of atomic orbitals (LCAO) method. Hückel used this simple method to investigate the energies of molecular orbitals of the π electrons in conjugated hydrocarbons systems, such as ethene, benzene, and butadiene. In NEHT, all the electrons are ignored but π electrons which determine most electronic properties of conjugated hydrocarbons molecules. In the extended version of Hückel theory that was developed later in 1963 by Roald Hoffmann [119], the σ orbitals were included. This increases the applicability of the Hückel theory beyond the conjugated hydrocarbons. NEHT uses no explicit real-space orbitals and instead assumes that the overlap matrix is the identity matrix, and then the Hamiltonian is parametrised based on atomic type and position. By comparison, the defining feature of EHT is the assumption that each element of the Hamiltonian matrix $\boldsymbol{H}_{ij}$ is directly proportional to the corresponding element of the (non-diagonal) overlap matrix $\boldsymbol{S}_{ij}$

$$\boldsymbol{H}_{ij} = \langle \psi_i | \hat{H} | \psi_j \rangle \approx c_{ij} \langle \psi_i | \psi_j \rangle = c_{ij} \boldsymbol{S}_{ij}, \tag{2.50}$$

where ψ are the basis set functions and c_{ij} are some parametrised constants that are independent of the basis set properties, removing the requirement for any complex three or higher central integrals. The Slater type orbitals (STOs) are often used as the basis set in an EHT calculation. The STO, $\chi(\vec{r}-\vec{R}_o)$, centered at atomic position $\vec{R}_o$, is taken to be the product of a radial wave function and an appropriate spherical harmonic term

$$\chi_{nlm}(\vec{r}-\vec{R}_o) = (2\zeta_{nl})^n \sqrt{\frac{2\zeta_{nl}}{(2n)!}} |\vec{r}-\vec{R}_o|^{n-1} \mathrm{e}^{-\zeta_{nl}(\vec{r}-\vec{R}_o)} Y_l^m(\vec{r}-\vec{R}_o) \tag{2.51}$$

where $\vec{R}_o$ is the position vector of the atom and n, l, and m are the principle, angular and magnetic quantum numbers respectively, ζ_{nl} is the Slater exponent (an empirical chosen parameter). Figure 2.5 shows the radial part of the STO with $n = 3$ and various values for the exponents ζ. It is clear that, the more the Slater exponent the narrower the curve and more localized the orbital is. On other hand, increasing the value of the n makes the orbital spread away from the nucleus.

For more accurate representations of the real atomic orbital, a linear combination of STOs can be used:

$$\phi_{nlm} = \sum c_i \chi_i(\vec{r}-\vec{R}_o) \tag{2.52}$$

The number of the STOs used in construction gives the name to the resulting ϕ_{nlm} orbital. For instance, using two STOs gives the double zeta orbital (DZO) and three of STOs gives the triple zeta orbital (TZO). In most cases, DZO is accurate enough to perform the EHT calculation.

The key approximation in the EHT is the assumption that the diagonal elements of

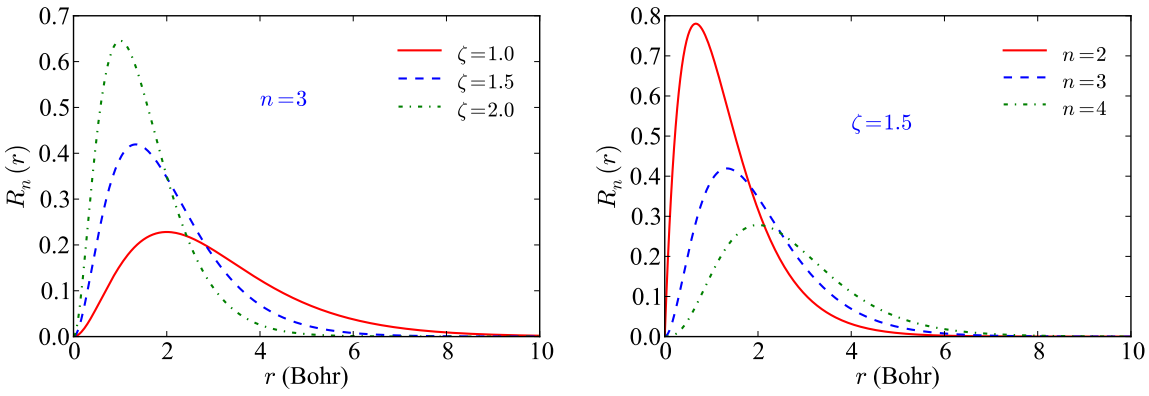

Figure 2.5: The radial part of the STO for (left) $n = 3$ and different values of exponent ζ and (right) for $\zeta = 1.5$ and various values of the quantum number n.

the Hamiltonian matrix $\boldsymbol{H}$ are set equal to $\mathscr{J}$, an empirically chosen parameter. That is

$$\boldsymbol{H}_{ii} = \langle \psi_i | \hat{H} | \psi_i \rangle \approx \mathscr{J}_i \tag{2.53}$$

The parameter $\mathscr{J}_i$, entering the expression for c_{ij} in equation (2.50), is regarded as the ionisation potential of the state ψ_i. For each orbital of each atomic species included in the calculation, a value for $\mathscr{J}_i$ is assigned. While the off-diagonal elements $\boldsymbol{H}_{ij}$ are taken to be either the arithmetic or the geometric average of $\mathscr{J}_i$ and $\mathscr{J}_j$

$$\boldsymbol{H}_{ij} = \begin{cases} \kappa\, \boldsymbol{S}_{ij} \dfrac{\mathscr{J}_i + \mathscr{J}_j}{2} & \text{arithmetic average,} \\ \kappa\, \boldsymbol{S}_{ij} \sqrt{\mathscr{J}_i + \mathscr{J}_j} & \text{geometric average,} \end{cases} \tag{2.54}$$

Here κ is an additional scaling factor known as the Wolfsberg-Helmholtz constant and the commonly used value is 1.75.

Bonding atoms of different electonegativities with each other causes charge to transfer between them. This transfer of charge modifies the ionisation potentials of the orbitals which has negative effects on transferability of the EHT parameters. To cope with this problem, an iterative scheme is employed, in which corrections to the Hamiltonian are determined at each iteration, and the new Hamiltonian used to compute new corrections until self-consistency is reached. Various schemes are used to calculate the atomic charges, such as the Mulliken population analysis [124], natural charges [125], and integrating the electronic charge density in real space. Once the excess charge on each atom has been specified, the ionisation potential $\mathscr{J}_{\alpha i}$ can be calculated using the formula [3]

$$\mathscr{J}_{\alpha i}(q) = \mathscr{J}^{o}_{\alpha i} + \beta_{\alpha i}(\delta q_i) \tag{2.55}$$

in which the ionisation potential $\mathscr{J}_{\alpha i}$ of the orbital α in the atom i is assumed to be a linear function of the excess charge (δq_i). $\mathscr{J}^{o}_{\alpha i}$ is the α orbital energy of the neutral atom i, and $\beta_{\alpha i}$ is the change in the orbital energy of atom i due deviation from charge

[3] Higher powers of δq_i with additional parameters can be added to obtain more accurate values of ionisation potentials. The physical meaning of the expression for $\mathscr{J}_{\alpha i}(q)$ is that an electron in an orbital α on atom i has a binding energy $\mathscr{J}^{o}_{\alpha i}$ corresponding to a neutral system and experiences a potential due to the accumulation of charge on that site.

neutrality. Other schemes for calculating the potentials also exist like Poisson solvers [126] or Non-equilibrium Green function (NEGF) methods [127].

2.3.1.1 Computing the overlap matrix

Computing the overlap matrix is the heart of the EHT calculation. The element $\boldsymbol{S}_{ij}$ of the overlap matrix is given by

$$\boldsymbol{S}_{ij} = \int \phi_i^* \phi_j \, dv = \langle \phi_i | \phi_j \rangle \tag{2.56}$$

where $\boldsymbol{S}_{ij}$ represents the overlap integral between the orbitals i and j. As mentioned before, STOs are usually employed in EHT calculation to approximate the real atomic orbital such that

$$\phi_{nlm}(\vec{r} - \vec{R}_o) \approx \chi_{nlm}(\vec{r} - \vec{R}_o) \tag{2.57}$$

The overlap integral $\boldsymbol{S}_{ij}$ can be computed either using numerical techniques, which are time consuming, or by using more efficient analytical expressions, whenever they are available, especially for large physical systems. One of the analytical expressions for overlap integrals of STOs was developed by Talman [128] and is used in this work. According to Talman, the overlap integral between two Slater orbitals centered at different points in space is given by

$$\begin{aligned} \mathscr{I}(n_1, l_1, m_1, \zeta_1, n_2, l_2, m_2, \zeta_2, \vec{R}) = (-1)^{m_1} \sum_{\Lambda} A_\Lambda \begin{bmatrix} l_1 & l_2 & \Lambda \\ 0 & 0 & 0 \end{bmatrix} \\ \times \begin{bmatrix} l_1 & l_2 & \Lambda \\ m_1 & -m_2 & m_2 - m_1 \end{bmatrix} Y_\Lambda^{m_1 - m_2}(\vec{R}) \end{aligned} \tag{2.58}$$

where $(n,\ l,\ m)$ and ζ are the quantum numbers and the Slater exponents of the two overlapped orbitals respectively, the vector $\vec{R}$ is joining the first orbital center to the second one, $Y_\Lambda^{m_1 - m_2}$ are the standard complex spherical harmonics, the quantities in square brackets are the $3-j$ coefficients and finally the factor A_Λ is given as

$$A_\Lambda(n_1, l_1, m_1, \zeta_1, n_2, l_2, m_2, \zeta_2, \vec{R}) = \sum_{\lambda=0}^{l_1} \sum_{L} \Upsilon_{\Lambda\lambda L} Q_{\lambda L} \tag{2.59}$$

where

$$\Upsilon_{\Lambda\lambda L} = (-1)^{l+\lambda}(2L+1)\,[4\pi(2\Lambda+1)(2l_1+1)(2l_1+1)]^{1/2} \times \frac{\Theta(l_2 L;\lambda)\Theta(L\Lambda;l_1-\lambda)}{\Theta(\Lambda l_2;l_1)} \tag{2.60}$$

Let $t = i + j + k$, then

$$\Theta(ij;k) = \frac{(t/2)!(t-2k)!}{(t+1)![(t-2i)/2]![(t-2j)/2]![(t-2k)/2]!} \tag{2.61}$$

Here any non-integer values resulting from the divisions by 2 are rounded towards zero before performing the factorial. The second factor $Q_{\lambda L}$ in equation (2.59) is defined as follows:

$$Q_{\lambda L} = \sum_{k=0}^{[L/2]} \sum_{p=0}^{L-2k} D_{Lkp} |\vec{R}|^{l_1-\lambda+L-2k-2p-1} \Xi(n_2+\lambda+2k-L, n_1-l_1, p) \tag{2.62}$$

where $[L/2]$ is the largest integer less than or equal to $L/2$, D and J are given respectively by

$$D_{Lkp} = \frac{(-1)^k(2L-2k)!}{2^{2L-2k}k!(L-k)!p!(L-2k-p)!} \tag{2.63}$$

$$\Xi(M,N,P) = |\vec{R}|^{M+N+2p+2} \sum_{\mu=0}^{M+N} B_{MN\mu} F_{\mu+p}(u) \Pi_{M+N-\mu+p}(v) \tag{2.64}$$

in which

$$B_{MN\mu} = \frac{1}{2^{M+N+1}} \sum_{b=\min(\mu,M)}^{\max(0,\mu-N)} (-1)^{N-\mu+b} \begin{pmatrix} M \\ b \end{pmatrix} \begin{pmatrix} N \\ \mu-b \end{pmatrix} \tag{2.65}$$

here the bracketed quantities represent the binomial coefficients,

$$F_s(u) = s! \frac{e^{-u}}{u^{s+1}} \sum_{i=0}^{s} \frac{u^i}{i!} \tag{2.66}$$

and

$$\Pi_s(v) = \frac{s!}{2v^{s+1}} \left[e^v \sum_{i=0}^{s} \frac{(-v)^i}{i!} - e^{-v} \sum_{i=0}^{s} \frac{v^i}{i!} \right] \tag{2.67}$$

where

$$u = \frac{(\zeta_2+\zeta_1)|\vec{R}|}{2} \tag{2.68}$$

and

$$\upsilon = \frac{(\zeta_2 - \zeta_1)|\vec{R}|}{2} \tag{2.69}$$

The limits of the summations [4] over Λ and L in equations (2.58) and (2.59) respectively are given by

$$\max(|l_1 - l_2|, |m_1 - m_2|) \leq \Lambda \leq l_1 + l_2 \tag{2.70}$$

$$\max(|l_2 - \lambda|, |\Lambda + \lambda - l_1|) \leq L \leq \min(|l_2 + \lambda|, |\Lambda + l_1 - \lambda|) \tag{2.71}$$

In the case of equation (2.67), numerical instabilities can arise from adding terms of opposite signs and which leads to non-convergent results. There are three special cases depending on the value of υ which are listed below:

1. For large value of υ, equation (2.67) can be used to compute the $\Pi_s(\upsilon)$ without any difficulty.

2. For small value of υ, equation (2.67) is used for the values of s that satisfies the following condition

$$e^{-\upsilon} \sum_{i=0}^{s} \frac{\upsilon^i}{i!} < 0.9 \qquad . \tag{2.72}$$

   Otherwise, the following alternative formula for $\Pi_s(\upsilon)$ is used

$$\Pi_s(\upsilon) = \frac{s!}{2\upsilon^{s+1}} \left[e^{-\upsilon} \sum_{i=s+1}^{\infty} \frac{\upsilon^i}{i!} - e^{\upsilon} \sum_{i=s+1}^{\infty} (-1)^i \frac{\upsilon^i}{i!} \right] \tag{2.73}$$

3. For $\upsilon = 0$, both expressions (2.67) and (2.73) give 0/0. This case is very common, occurring in any system with more than one atom of the same atomic species. Hence giving rise to overlaps for which $\zeta_1 = \zeta_2$. For this special case the following equation will be used

$$\Pi_s(\upsilon = 0) = \begin{cases} 0 & \text{if } s \text{ is odd,} \\ \dfrac{1}{s+1} & \text{if } s \text{ is even} \end{cases} \tag{2.74}$$

[4] The limits are bounded by the range of possible values, e.g. by the range of values for which the $3-j$ coefficients are defined in the case of λ.

One final source of numerical divergence is the case of $\vec{R}$ approaching zero. This situation occurs when two atoms approach to each other closely which could not happen in real systems [5]. The other possibility of $\vec{R}$ being zero is the case of multiple orbitals centred on the same atom. The solution to this case is trivially given by

$$\mathscr{I}(n_1, l_1, m_1, \zeta_1, n_2, l_2, m_2, \zeta_2, \vec{R} = 0) = \delta_{n_1 n_2} \delta_{l_1 l_2} \delta_{m_1 m_2} \tag{2.75}$$

2.3.1.2 The real form of overlap integral

Up to this point the expression (2.58) for the overlap integral is in terms of the complex spherical harmonics. This yields a complex value for $\mathscr{I}$ and consequently for both the overlap and the Hamiltonian matrices. Performing the calculation with complex matrices would require further steps of computation as much as a factor of four [92]. Moreover, visualisation of any real space properties of a system following a calculation needs to know the exact representations of the orbitals in use in real space. Finally, for molecules or large systems where the unit cell is big enough to consider only the Γ point in calculation, it is preferable for $\mathscr{I}$ to have a real value in order to obtain real and symmetric overlap and Hamiltonian matrices at the Γ point. For these motivations it is worth recasting the result into a real form using tesseral spherical harmonics which are related to complex ones by the equations

$$Z_{lm} = \begin{cases} \dfrac{1}{\sqrt{2}}(Y_l^m + (-1)^m Y_l^{-m}) & \text{for } m > 0 \\ Y_l^0 & \text{for } m = 0 \\ \dfrac{1}{\mathrm{i}\sqrt{2}}(Y_l^{-m} - (-1)^m Y_l^m) & \text{for } m < 0 \end{cases} \tag{2.76}$$

By using these definitions, the real form of the overlap integral $\mathscr{I}_R$ takes nine different forms depending on the different ways of combination between the values of m_1 and m_2 as follows:

$$\mathscr{I}_R(m_1, m_2, ...) = \mathrm{sign}(m_2)(-1)^{l_1+l_2+m_1+m_2} \mathscr{I}_C(m_1, m_2, ...) \tag{2.77}$$

where

[5] In programming terms, this is implemented by making sure that any two atoms do not approach closely beyond a predefined specific distance, otherwise the code will stop.

- if $m_1 = 0$ and $m_2 = 0$,

$$\mathscr{I}_C(m_1, m_2) = \mathscr{I}(m_1, m_2) \tag{2.78}$$

- if $m_1 = 0$ and $m_2 > 0$,

$$\mathscr{I}_C(m_1, m_2) = \frac{1}{\sqrt{2}}[\mathscr{I}(m_1, m_2) + (-1)^{m_2}\mathscr{I}(m_1, -m_2)] \tag{2.79}$$

- if $m_1 = 0$ and $m_2 < 0$,

$$\mathscr{I}_C(m_1, m_2) = \frac{1}{\mathrm{i}\sqrt{2}}[\mathscr{I}(m_1, -m_2) + (-1)^{m_2}\mathscr{I}(m_1, m_2)] \tag{2.80}$$

- if $m_1 > 0$ and $m_2 = 0$,

$$\mathscr{I}_C(m_1, m_2) = \frac{1}{\sqrt{2}}[\mathscr{I}(m_1, m_2) + (-1)^{m_1}\mathscr{I}(-m_1, m_2)] \tag{2.81}$$

- if $m_1 > 0$ and $m_2 > 0$,

$$\begin{aligned}\mathscr{I}_C(m_1, m_2) = \frac{1}{2}[&\mathscr{I}(m_1, m_2) + (-1)^{m_1}\mathscr{I}(-m_1, m_2) \\ &+ (-1)^{m_2}\mathscr{I}(m_1, -m_2) + (-1)^{m_1+m_2}\mathscr{I}(-m_1, -m_2)]\end{aligned} \tag{2.82}$$

- if $m_1 > 0$ and $m_2 < 0$,

$$\begin{aligned}\mathscr{I}_C(m_1, m_2) = \frac{1}{2\mathrm{i}}[&\mathscr{I}(m_1, -m_2) + (-1)^{m_1}\mathscr{I}(-m_1, -m_2) \\ &- (-1)^{m_2}\mathscr{I}(m_1, m_2) - (-1)^{m_1+m_2}\mathscr{I}(-m_1, m_2)]\end{aligned} \tag{2.83}$$

- if $m_1 < 0$ and $m_2 = 0$,

$$\mathscr{I}_C(m_1, m_2) = \frac{1}{\mathrm{i}\sqrt{2}}[\mathscr{I}(-m_1, m_2) + (-1)^{m_1}\mathscr{I}(m_1, m_2)] \tag{2.84}$$

- if $m_1 < 0$ and $m_2 > 0$,

$$\begin{aligned}\mathscr{I}_C(m_1, m_2) = \frac{1}{2\mathrm{i}}[&\mathscr{I}(-m_1, m_2) - (-1)^{m_1}\mathscr{I}(m_1, m_2) \\ &+ (-1)^{m_2}\mathscr{I}(m_1, -m_2) - (-1)^{m_1+m_2}\mathscr{I}(m_1, -m_2)]\end{aligned} \tag{2.85}$$

- if $m_1 < 0$ and $m_2 < 0$,

$$\begin{aligned}\mathscr{I}_C(m_1, m_2) = -\frac{1}{2}[&\mathscr{I}(-m_1, -m_2) - (-1)^{m_1}\mathscr{I}(m_1, -m_2) \\ &- (-1)^{m_2}\mathscr{I}(-m_1, m_2) + (-1)^{m_1+m_2}\mathscr{I}(m_1, m_2)]\end{aligned} \tag{2.86}$$

As the double zeta orbitals are commonly used in EHT, especially for the d orbitals in the transition metals, extending the overlap expression $\mathscr{I}$ is required. The double zeta Slater orbital is expressed as a linear combination of two single standard orbitals, as

given by equation (2.51), each with different exponent ζ (but otherwise identical)

$$\chi_{nlm}^{DZ} = \sum_{i=1}^{2} c_i \chi_{nlm}(\zeta_i) \tag{2.87}$$

Hence the overlap integral ($\mathscr{I}^{DZ}$) between two DZSOs can be written as

$$\mathscr{I}^{DZ} = \sum_{i=1}^{2}\sum_{j=1}^{2} c_1^{(i)} c_2^{(j)} \mathscr{I}(\zeta_1^{(i)}, \zeta_2^{(j)}) \tag{2.88}$$

where $\zeta_1^{(i)}$ is the i^{th} exponent of the first DZSO. The inspection of the set of equations (2.58-2.69) shows that the only $F_s(u)$ and $\Pi_s(v)$ quantities are ζ dependence. As these two quantities appear only within the definition of the quantity Ξ in equation (2.64), performing the whole calculation more than once is not necessary. So using the DZ orbitals in EHT can be taken into account computationally by modifying the equation (2.64) into:

$$\begin{aligned}\Xi(M,N,P) = |\vec{R}|^{M+N+2p+2} \sum_{\mu=0}^{M+N} B_{MN\mu} \sum_{i,j=1}^{2} F_{\mu+p}\Big(u(\zeta_1^{(i)}, \zeta_2^{(j)})\Big) \\ \times \Pi_{M+N-\mu+p}\Big(v(\zeta_1^{(i)}, \zeta_2^{(j)})\Big) c_1^{(i)} c_2^{(j)}\end{aligned} \tag{2.89}$$

with

$$u(\zeta_1^{(i)}, \zeta_2^{(j)}) = \frac{\zeta_1^{(i)} + \zeta_2^{(j)}}{2} |\vec{R}| \tag{2.90}$$

$$v(\zeta_1^{(i)}, \zeta_2^{(j)}) = \frac{\zeta_2^{(i)} - \zeta_1^{(j)}}{2} |\vec{R}| \tag{2.91}$$

The coefficients c's may be treated as adjustable parameters like the ζ exponents, but usually their values are normalised such that the overlap of the DZ orbital with itself is set to one. This leads to

$$c_2 = \frac{1}{2} - b \mp \sqrt{b^2 + 4 - 4c_1^2} \tag{2.92}$$

with

$$b = c_1 \frac{2^{2n+2}(\zeta_1\zeta_2)^{n+0.5}}{(\zeta_1 + \zeta_2)^{2n+1}} \tag{2.93}$$

Hence, one of the two roots that yields $0 \leq c_2 \leq 1$ is chosen. In the case that the c's coefficients are determined in different way, the overlap is required to be less than one;

this is equivalent to normalise a triple zeta orbital to one where $\zeta_3 \rightarrow \infty$. In many cases a single zeta orbital is used with a value of c_1 less than one which is equivalent to a double zeta orbital with $\zeta_2 \rightarrow \infty$.

For an isolated system, a single unit cell is employed to perform the calculation of the overlap matrix $\boldsymbol{S}$ which holds the overlaps between all the atoms. In the case of periodic system, unlimited number of overlap matrices is required to fully describe it. Each one represents the overlap between atoms in the reference (original) unit cell with each atom in different cells. However, exploiting the fact that the overlap $\mathscr{S}$ goes to zero when the distance $|\vec{R}|$, separated overlapped orbitals, is large, provides a limit on how many of the matrices are required to be constructed. Hence, for those unit cells whose centres are located outside of a sphere centred at the reference unit cell with radius equal to some cut off distance R_c will be ignored (Figure 2.6) [6]. For large unit cell with their three dimensions being greater than the cut off distance, only the nearest neighbour cells are needed, giving 3, 9, and 27 overlap matrices in total for 1D, 2D, and 3D case respectively. After constructing the overlap matrices, the final $\boldsymbol{S}$ matrix can be calculated using the formula

$$\boldsymbol{S}_{ij} = \sum_{\ell} \boldsymbol{S}^{\ell}_{ij} \mathrm{e}^{\mathrm{i}(\vec{k}.\vec{R}_{\ell})} \tag{2.94}$$

where the sum runs over all the unit cells that considered in calculation. The phase factor $\mathrm{e}^{\mathrm{i}(\vec{k}.\vec{R}_{\ell})}$ is computed at each k point for all the lattice positions $\vec{R}_{\ell}$.

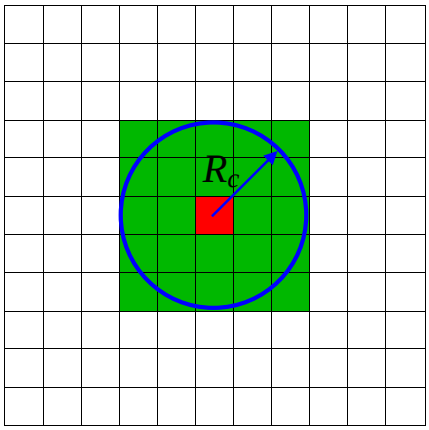

Figure 2.6: Schematic diagram of 2D square lattice showing the original unit cell in red and the cells to be considered in constructing the overlap matrix in green.

[6] It has been assumed here that the lattice vectors are orthogonal.

CHAPTER 3

THEORY OF MOLECULAR CONDUCTANCE

3.1 Introduction

According to Ohm's law, the resistance $\mathscr{R}$ of a conductor is directly proportional to its length L and inversely proportional to its cross sectional area A; that is,

$$\mathscr{R} = \frac{V}{I} = \frac{\rho L}{A} \tag{3.1}$$

where ρ is the resistivity and it is characteristic of the conductor material. The reciprocal of the resistance is the conductance $\mathscr{G}$

$$\mathscr{G} = \frac{1}{\mathscr{R}} = \sigma \frac{A}{L} \tag{3.2}$$

where $\sigma = 1/\rho$ is the conductivity. Equation (3.2) suggests that the conductance of a conductor increases indefinitely by decreasing its length. However, the experimental results showed that this ohmic behaviour breaks down at some critical value of the conductor length. Below this specific length, the conductance reaches its maximum value and decreasing the length has no effect on $\mathscr{G}$. In other words, as illustrated schematically in Figure 3.1, the resistance of any conductor cannot be reduced to less than a minimum finite value $\mathscr{R}_0$. The question raised here is intriguing: what is the origin of this resistance? The proper answer of this question was first pointed out by Imry [130], who associated the finite resistance with the resistance arising at the interfaces between leads and the sample in between them. As the length of the conductor is reduced to the atomic scale such that the conductor is just an individual

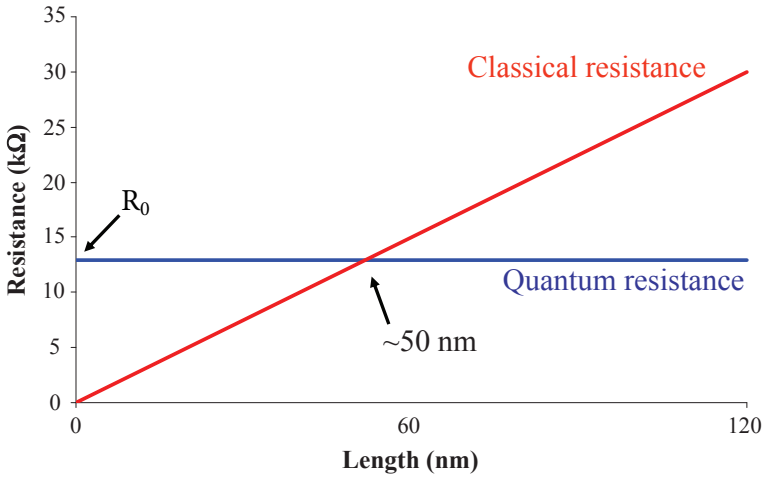

Figure 3.1: The resistance of a conductor vs its length. Adapted from ref. [129].

molecule, the effect of quantum phenomena becomes more important and dominates the conducting process. This can lead to an unexpected and incongruous behaviour to the classical one, such as a resistance that is independent of molecule length [131], non-linear I-V characteristics and even negative differential resistance [132]. One of the most interesting and important results is the quantization of conductance [133]; for any energy level within a conducting channel, the conductance cannot exceed a finite value $\mathscr{G}_0$ which can be introduced as “a quantum of conductance". This value is defined in terms of two fundamental physical quantities: the elementary charge e and Planck's constant h, as

$$\mathscr{G}_0 = \frac{e^2}{h} = 38.7\mu S = (25.8\text{k}\Omega)^{-1} \tag{3.3}$$

In some descriptions, an extra factor of 2 is included to account for spin up and down quanta.

A conductor would exhibit various transport regimes depending upon its dimensions relative to three characteristic length scales: the phase relaxation (coherent) length L_ϕ, the mean free path ℓ and the de Broglie wavelength λ. These regimes can be summarized as the following [95]:

1. Mesoscopic if $\lambda << L < L_\phi$,
2. Diffusive if $L >> \lambda$ and $L >> \ell$,
3. Ballistic if $\lambda << L < \ell$,
4. Quantum transport if $\lambda \sim L$.

The diffusive and ballistic transport can be described using classical or semi-classical laws, whereas quantum transport phenomena (where the typical dimensions of the sample are within atomic-scale) are fully governed by quantum mechanics. The mesoscopic regime would be a separate kingdom governed by separate laws that are neither purely quantum nor purely classical; rather, a synthesis of the two. If the dimensions of the conductor are much larger than each of the three length scales, the conductor shows ohmic behaviour. The above classification of the different transport regimes should not be taken as completely rigorous and one may imagine situations where the electrons in a device behave ballistically at low temperature and diffusively at high temperature.

3.2 One level model

To study the quantum transport through an individual molecule, we will introduce a simple model for electronic transport which is the one level model. We will follow the derivation given by Paulsson *et al.* [134]. Figure 3.2 shows the energy level diagram of a molecule with single energy level sandwiched between metal leads. Both leads are assumed to contain a completely flat continuum of states, which extends to all energies, and which is filled up to some Fermi level μ_L and μ_R. The molecule is coupled to both leads with coupling constants Γ_L and Γ_R which have units of energy. Physically, Γ_L and Γ_R (divided by $\hbar$) represent the rate at which an electron in the molecule's energy level ε would escape into left lead and right lead, respectively. The stronger coupling the higher probability for escaping. If the energy level of the molecule was in equilibrium with the left lead, then the number of electrons occupying the level would be given by

$$N_L = 2f(\varepsilon, \mu_L) \tag{3.4}$$

where the factor 2 is for spin up and down and

$$f(\varepsilon, \mu) = \frac{1}{1 + \exp\left[\dfrac{\varepsilon - \mu}{k_B T}\right]} \tag{3.5}$$

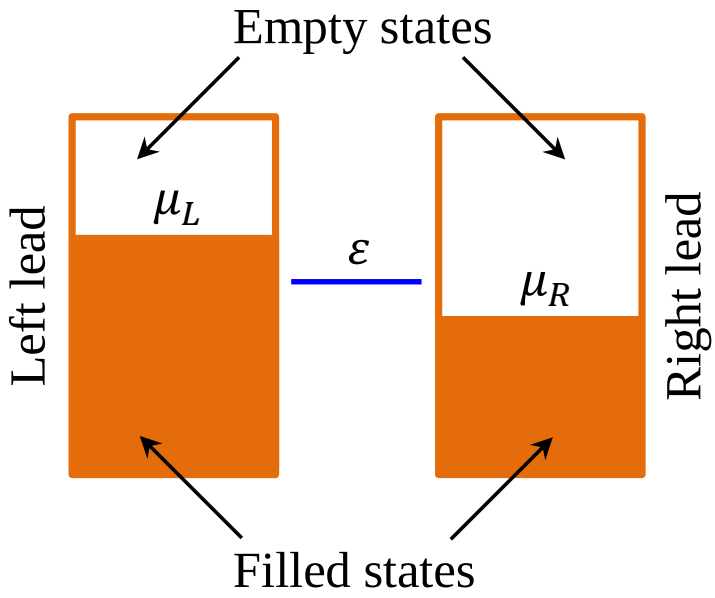

Figure 3.2: A molecule with one energy level in between two leads.

is the Fermi distribution function. Similarly, if the level was in equilibrium with the right lead, the number of electrons occupying the level would be

$$N_R = 2f(\varepsilon, \mu_R) \tag{3.6}$$

Under non-equilibrium conditions, the number of electrons N will be somewhere in between N_L and N_R. To determine this number, we write the net current I_L at the left junction:

$$I_L = \frac{e\Gamma_L}{\hbar}(N_L - N) \tag{3.7}$$

and the net current at the right junction:

$$I_R = \frac{e\Gamma_R}{\hbar}(N - N_R) \tag{3.8}$$

Steady state requires $I_L = I_R$, from which we obtain

$$N = 2\frac{\Gamma_L f(\varepsilon, \mu_L) + \Gamma_R f(\varepsilon, \mu_R)}{\Gamma_L + \Gamma_R} \tag{3.9}$$

So that from equation (3.7) or equation (3.8) we obtain the current:

$$I = \frac{2e}{\hbar}\frac{\Gamma_L\Gamma_R}{\Gamma_L+\Gamma_R}\left[f(\varepsilon,\mu_L) - f(\varepsilon,\mu_R)\right] \tag{3.10}$$

Equation (3.10) illustrates few basic facts about the process of current flow:

1. No current will flow if $f(\varepsilon,\mu_L) = f(\varepsilon,\mu_R)$.

2. A level that is at lower energy than both Fermi levels μ_L and μ_R will have $f(\varepsilon,\mu_L) = f(\varepsilon,\mu_R) = 1$ and will not contribute to the current.

3. A level that is at higher energy than the μ_L and μ_R and has $f(\varepsilon,\mu_L) = f(\varepsilon,\mu_R) = 0$ will not contribute also to the current.

4. It is only when the molecule's level lies between μ_L and μ_R (or within a few $k_\mathrm{B}T$ of μ_L and μ_R) that we have $f(\varepsilon,\mu_L) \neq f(\varepsilon,\mu_R)$, and a current flows.

From equation (3.10) we can see that, the maximum current that can flow through one molecular level is equal to

$$I_{max} = \frac{2e}{\hbar}\frac{\Gamma_L\Gamma_R}{\Gamma_L+\Gamma_R} \tag{3.11}$$

Figure 3.3 shows a typical I-V characteristics of one energy level calculated from equation (3.10) for different parameters. It can be seen that, at small bias voltages, the current is zero because both μ_L and μ_R are above the molecule energy level. When the voltage becomes sufficiently high, the μ_R drops below the energy level and the current increases to the maximum value I_{max}. It is worth noting that, the size of the gap in the current-voltage curve is equal to $4|E_f - \varepsilon_0|$. E_f is the Fermi level of the system (left lead + molecule + right lead) at equilibrium, i.e. $V = 0$.

3.2.1 Charging effects

When the current flows through the molecule of single energy level, electrons are added to or removed from the level continuously leading to what is called "charging effects". These effects have not been taken into account in the simple picture provided in the previous section. The change in electron occupation of the energy level modifies the

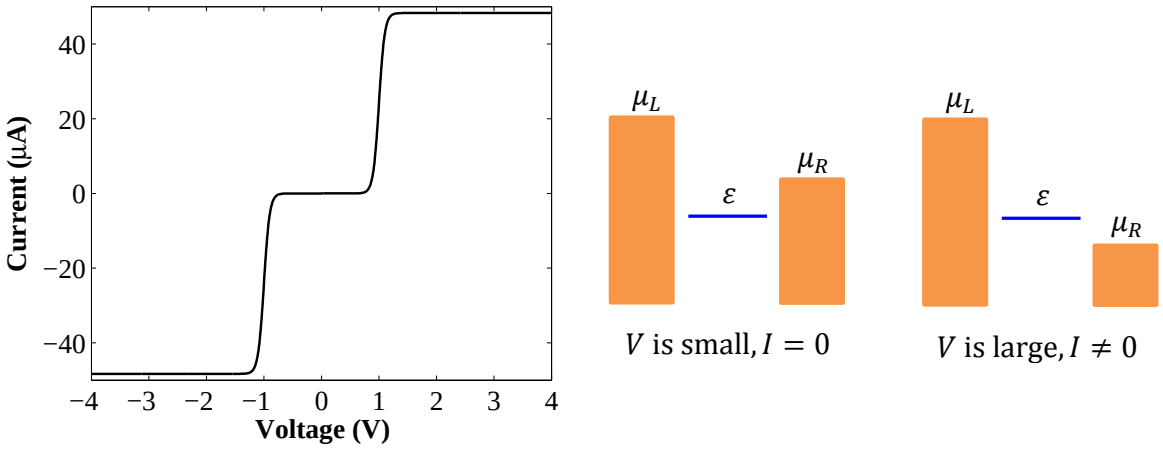

Figure 3.3: (Right) The current-voltage (I-V) characteristics of a single energy level with $\mu_L = E_f - \frac{eV}{2}$, $\mu_R = E_f + \frac{eV}{2}$, $E_f = -5.0$ eV, $\varepsilon_0 = -5.5$ eV and $\Gamma_L = \Gamma_R = 0.2$ eV. (Left) The voltage dependence position of the energy level relative to the μ_L and μ_R.

potential in the molecule. In order to make our one level model more realistic, we should include effects of charging. This can be done by assuming that the single energy level has the following form

$$\varepsilon = \varepsilon_0 + U_{SC} \tag{3.12}$$

That is, the energy level ε floats up or down by the amount of the potential U_{SC}, calculated self-consistently, which is given by

$$U_{SC} = U(N - 2f(\varepsilon_0, E_f)) \tag{3.13}$$

where $f(\varepsilon_0, E_f)$ is the Fermi distribution function of the initial occupation of the molecule at zero bias voltage. N is the electronic population at a particular bias voltage V. Because of the mutual dependence of the potential (U_{SC}) and the electronic population (N) on each other, both need to be calculated self-consistently by iterating over equations (3.9), (3.12) and (3.13). Figure 3.4 shows the current and conductance versus voltage with ($U = 1.0$ and 2.0 eV) and without ($U = 0.0$ eV) charging effects.

3.2.2 Unrestricted model

Up to this point, we have assumed that the two electrons, with spin up and down, occupy the energy level with the same population and hence they feel the same potential U_{SC}. But in reality there is no such restriction. This effect can be included in our model by

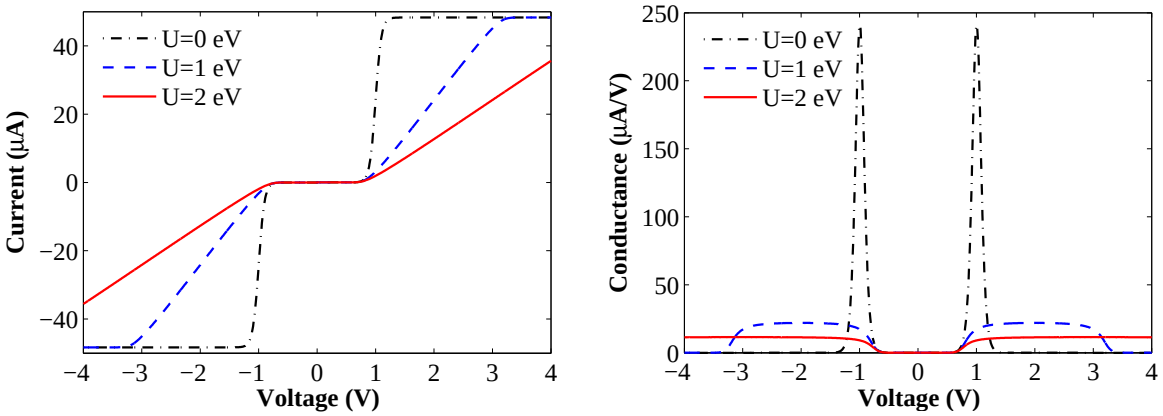

Figure 3.4: The current-voltage (I-V) characteristics (left) and conductance-voltage (G-V) (right) of a single energy level with $E_f = -5.0$ eV, $\varepsilon_0 = -5.5$ eV and $\Gamma_L = \Gamma_R = 0.2$ eV.

replacing equation (3.12) with the following two equations for spin up and down

$$\varepsilon_\uparrow = \varepsilon_0 + U(N_\downarrow - f(\varepsilon_0, E_f)) \tag{3.14}$$

$$\varepsilon_\downarrow = \varepsilon_0 + U(N_\uparrow - f(\varepsilon_0, E_f)) \tag{3.15}$$

These equations tell that, the up-spin level experiences a potential due to the down-spin electrons and vice-versa. Equations (3.14) and (3.15) reduce back to the case of restricted model represented by equation (3.12) when the U approaches zero. However, for a large value of the potential U, it is very likely that the occupation of one level, with either spin up or down, is large. This shifts the other level, with the opposite spin, to some position out of the window $(\mu_L - \mu_R)$ between the two leads. Hence, this shifted level is not involved in conduction until the bias voltage becomes large enough to overcome the effect. This effect is known as a Coulomb blockade and it is illustrated in Figure 3.5.

3.2.3 Broadening of the energy level

In addition to the effects of charging and differing in spin population of the energy level, there is still another important factor that we have not considered yet, the broadening effect. The broadening of the level is caused by the coupling to the leads as shown in Figure 3.6. This causes part of the energy level to spread outside the energy range between μ_L and μ_R where current flows. The actual current is then reduced below what

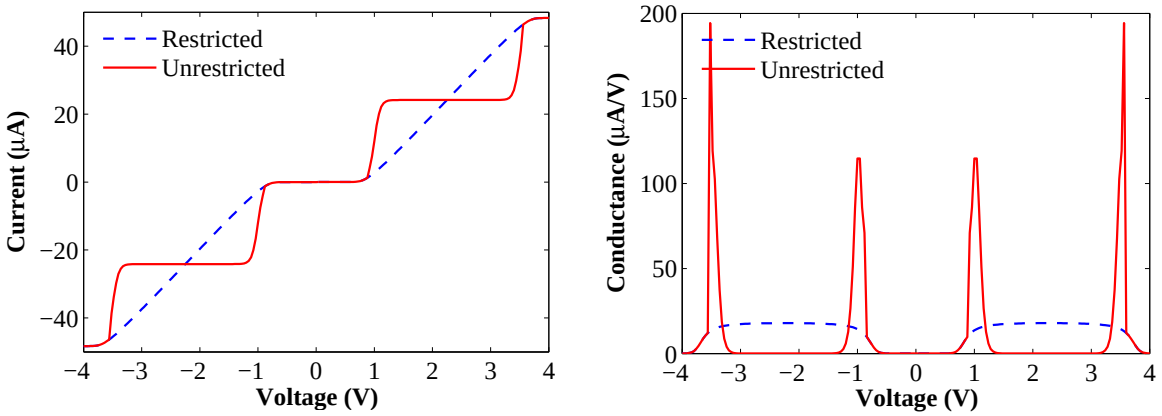

Figure 3.5: The current-voltage (I-V) (left) and conductance-voltage (G-V) (right) characteristics for restricted (dashed line) and unrestricted models (solid line) of a single energy level with $E_f = -5.0$ eV, $\varepsilon_0 = -5.5$ eV, $\Gamma_L = \Gamma_R = 0.2$ eV and U = 1.25 eV.

is expected from equation (3.10) by a factor representing the fraction of the level that lies in the window between μ_L and μ_R.

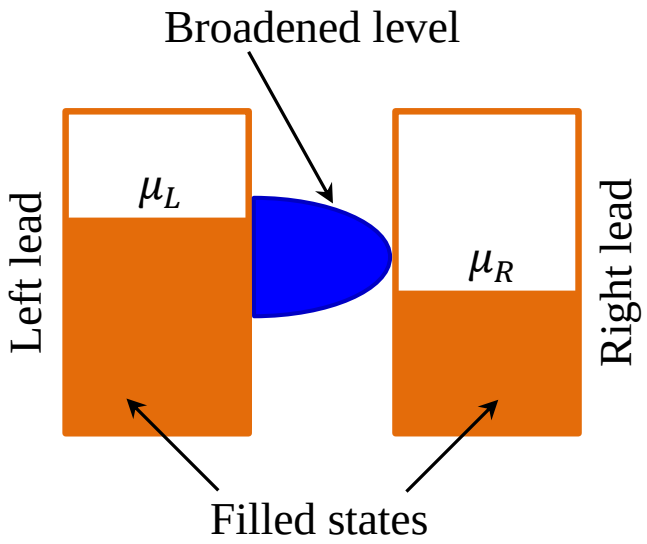

Figure 3.6: The broadening of one energy level because of the coupling to the leads.

The broadening effect can be taken into account by replacing the discrete energy level with an appropriate density of states function. The DOS of the broadened level could in principle have any shape, but the simplest one is the Lorentzian function centered around $E = \varepsilon$:

$$D_\varepsilon(E) = \frac{1}{2\pi} \frac{\Gamma}{(E-\varepsilon)^2 + (\Gamma/2)^2} \tag{3.16}$$

where $\Gamma = \Gamma_L + \Gamma_R$ is the broadening parameter. When the broadening tends to zero ($\Gamma \to 0$), the $D_\varepsilon(E)$ tends to take the shape of delta function. Clearly D_ε should have

the property to hold only one electron, hence its energy integral is equal to one. It is then quite intuitive to re-define the expressions for the number of electrons N and the current across the two terminals in terms of the DOS associated to D_ε as follows

$$N = 2\int_{-\infty}^{\infty} \mathrm{d}E D_\varepsilon(E) \frac{\Gamma_L f(E,\mu_L) + \Gamma_R f(E,\mu_R)}{\Gamma_L + \Gamma_R} \tag{3.17}$$

and

$$I = \frac{2e}{\hbar}\int_{-\infty}^{\infty} \mathrm{d}E D_\varepsilon(E) \frac{\Gamma_L \Gamma_R}{\Gamma_L + \Gamma_R}\left[f(E,\mu_L) - f(E,\mu_R)\right] \tag{3.18}$$

The Γ's have been intentionally left inside the integral since the broadening can be a function of the energy in general. It is worth mentioning that, the argument of the integral in equation (3.17) is nothing but the electron charge density at the steady state

$$\rho(E) = D_\varepsilon(E) \frac{\Gamma_L f(E,\mu_L) + \Gamma_R f(E,\mu_R)}{\Gamma_L + \Gamma_R} \tag{3.19}$$

To see the broadening effect on conduction, the I-V characteristics of a molecule with a single energy level are depicted in Figure 3.7 for restricted and unrestricted models. In

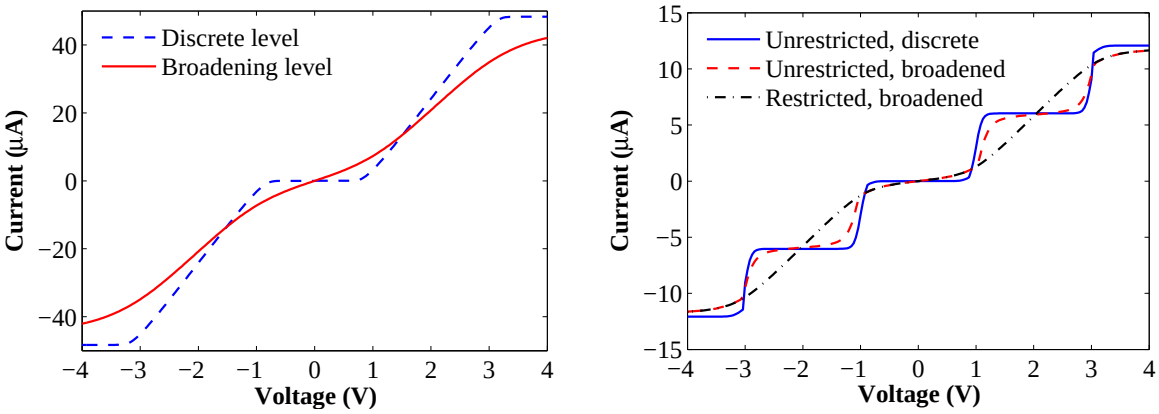

(a) Restricted model

(b) Unrestricted model

Figure 3.7: The current-voltage (I-V) characteristics of a molecule with a single energy level showing the broadening effects, in the case of restricted (left) and unrestricted (right) model. For both figures, the following parameters were used; $E_f = -5.0$ eV, $\varepsilon_0 = -5.5$ eV, $U = 1.0$ eV and $\Gamma_L = \Gamma_R = 0.2$ eV (a) and $\Gamma_L = \Gamma_R = 0.05$ eV (b).

the case of the restricted model, the main effect of broadening is to make the I-V curve smother as shown in Figure 3.7a. The same is true for the unrestricted model as long

as the broadening is much smaller than the charging energy Figure 3.7b. But moderate amounts of broadening can destroy the Coulomb blockade effects completely and make the I-V characteristics look identical to the restricted model.

3.3 NEGF formalism

Although the simple model introduced in the previous section shed some light on basic factors that influence molecular conduction, it does not describe two important aspects of a real device: the electronic structure of the contacts and the details of the scattering region Hamiltonian. These are replaced respectively by the Fermi distribution functions and by a single energy level. In reality, the molecular devices typically have multiple energy levels that broaden and overlap with each other and with the contacts levels. A general formalism is needed to include these details. The non-equilibrium Green's function (NEGF) formalism described in this section does just that.

Figure 3.8 shows a typical molecule in between two metal leads. To investigate the electrical conduction through the molecule, the system is divided into three regions: the left lead, the right lead, and the scattering (central) region where the molecule of interest is located. The part of the scattering region where the atom positions follow the periodic arrangement of the leads is called the left and right lead extension. A sufficient fraction of the leads are included in the scattering region to screen out the perturbation of the scatterer , i.e. the molecule, in the outermost part of the scattering region. Since the two leads are semi-infinitely extended to the left and right sides (where the periodic boundary conditions are applied), the Hamiltonian of the whole system will be infinite in size. However, it can be computed by exploiting the periodic nature of the leads from smaller calculable components.

To calculate the Hamiltonian of the system, for each lead a principal unit cell of calculation is chosen, which is at minimum the smallest number of atomic layers required so that no coupling exists between next nearest unit cells. As illustrated in Figure 3.9, each principal unit cell now has a finite Hamiltonian $\boldsymbol{H}_L$ and $\boldsymbol{H}_R$, and another matrix which describes the coupling between each principal unit cell and its next nearest unit $\boldsymbol{H}_{LC}$ and $\boldsymbol{H}_{RC}$. The scattering region also has a finite Hamiltonian $\boldsymbol{H}_S$ and coupling matrices between itself and each lead $\boldsymbol{H}_{SLC}$ and $\boldsymbol{H}_{SRC}$. The infinite

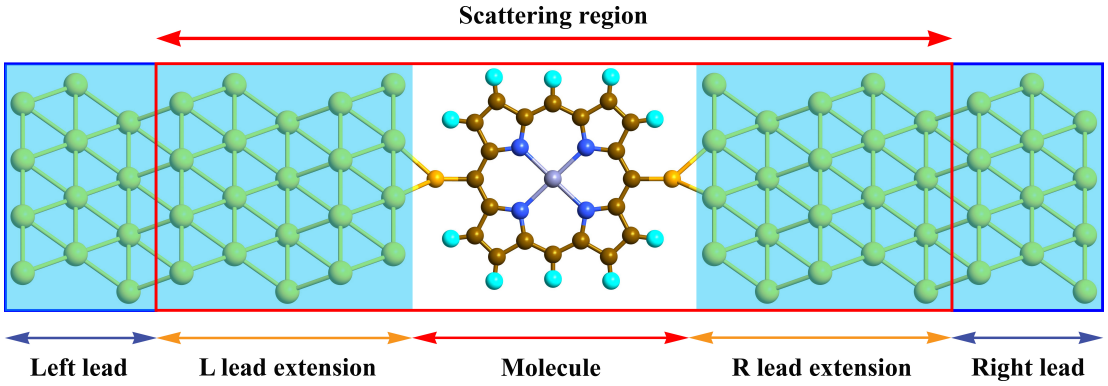

Figure 3.8: Zinc porphyrin molecule sandwiched between two bulk gold leads.

Hamiltonian describing the system can then be written as

$$H = \begin{bmatrix} \ddots & H_{LC} & 0 & 0 & 0 & 0 & \iddots \\ H_{LC}^{\dagger} & H_L & H_{LC} & 0 & 0 & 0 & 0 \\ 0 & H_{LC}^{\dagger} & H_L & H_{SLC} & 0 & 0 & 0 \\ 0 & 0 & H_{SLC}^{\dagger} & H_S & H_{SRC} & 0 & 0 \\ 0 & 0 & 0 & H_{SRC}^{\dagger} & H_R & H_{RC} & 0 \\ 0 & 0 & 0 & 0 & H_{RC}^{\dagger} & H_R & H_{RC} \\ \iddots & 0 & 0 & 0 & 0 & H_{RC}^{\dagger} & \ddots \end{bmatrix} \tag{3.20}$$

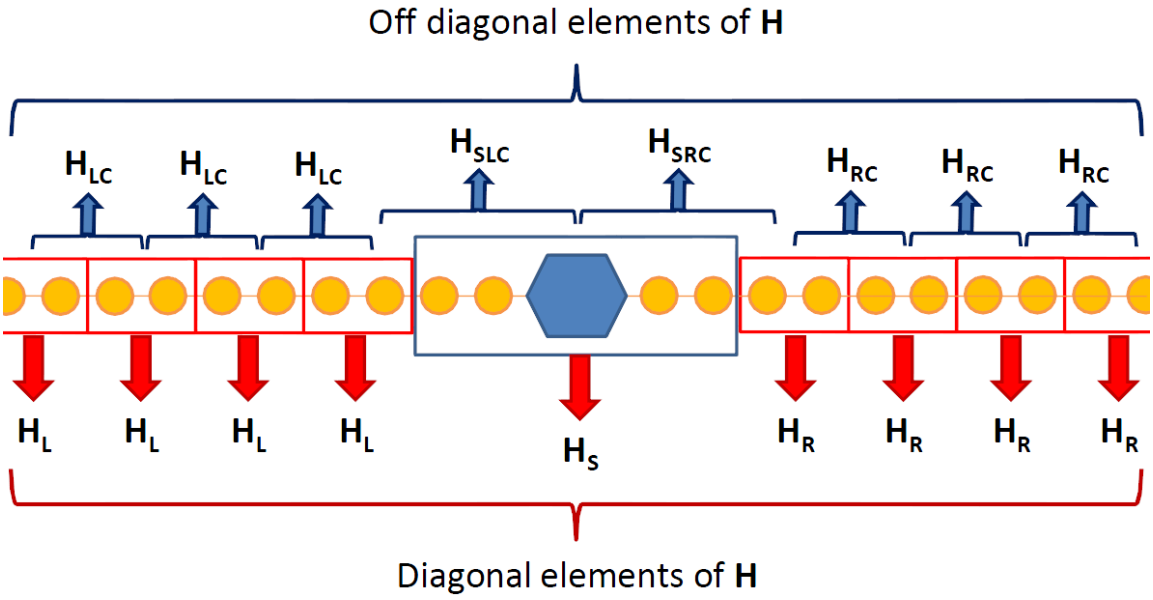

Figure 3.9: Schematic diagram shows how the Hamiltonian of the one dimensional system is built up. In this example, each red rectangle, with two atoms, represents one principal unit cell of the lead, and the blue rectangle represents the scattering region which consists of left and right lead extensions and the molecule of interest.

The overlap matrix $\boldsymbol{S}$ can be obtained in the same manner:

$$\boldsymbol{S} = \begin{bmatrix} \ddots & \boldsymbol{S}_{LC} & 0 & 0 & 0 & 0 & \iddots \\ \boldsymbol{S}_{LC}^{\dagger} & \boldsymbol{S}_{L} & \boldsymbol{S}_{LC} & 0 & 0 & 0 & 0 \\ 0 & \boldsymbol{S}_{LC}^{\dagger} & \boldsymbol{S}_{L} & \boldsymbol{S}_{SLC} & 0 & 0 & 0 \\ 0 & 0 & \boldsymbol{S}_{SLC}^{\dagger} & \boldsymbol{S}_{S} & \boldsymbol{S}_{SRC} & 0 & 0 \\ 0 & 0 & 0 & \boldsymbol{S}_{SRC}^{\dagger} & \boldsymbol{S}_{R} & \boldsymbol{S}_{RC} & 0 \\ 0 & 0 & 0 & 0 & \boldsymbol{S}_{RC}^{\dagger} & \boldsymbol{S}_{R} & \boldsymbol{S}_{RC} \\ \iddots & 0 & 0 & 0 & 0 & \boldsymbol{S}_{RC}^{\dagger} & \ddots \end{bmatrix} \tag{3.21}$$

Because of the infinite size of the overlap matrix $\boldsymbol{S}$ and the Hamiltonian $\boldsymbol{H}$, the problem is insoluble. However, these matrices can be converted into something tractable by using the non-equilibrium Green's function (NEGF) formalism. For a single energy level ε, the Green's function is defined as:

$$G(E) = \left(E - \varepsilon + \mathrm{i}\frac{\Gamma_L + \Gamma_R}{2} \right)^{-1}, \tag{3.22}$$

and in the case of the whole (infinite) system, the Green's function equation is given by

$$\left[(E + \mathrm{i}\tau)\boldsymbol{S} - \boldsymbol{H} \right] \boldsymbol{G}(E) = \boldsymbol{I} \tag{3.23}$$

where τ is infinitesimal small positive number added to avoid singularity in calculation. $\boldsymbol{I}$ is the identity matrix with the same size of $\boldsymbol{S}$ and $\boldsymbol{H}$. Equation (3.23) can be written in full form as follows:

$$\left((E + \mathrm{i}\tau) \begin{bmatrix} \ddots & \boldsymbol{S}_{LC} & 0 & 0 & \iddots \\ \boldsymbol{S}_{LC}^{\dagger} & \boldsymbol{S}_{L} & \boldsymbol{S}_{LC} & 0 & 0 \\ 0 & \boldsymbol{S}_{LC}^{\dagger} & \boldsymbol{S}_{S} & \boldsymbol{S}_{RC} & 0 \\ 0 & 0 & \boldsymbol{S}_{RC}^{\dagger} & \boldsymbol{S}_{R} & \boldsymbol{S}_{RC} \\ \iddots & 0 & 0 & \boldsymbol{S}_{RC}^{\dagger} & \ddots \end{bmatrix} - \begin{bmatrix} \ddots & \boldsymbol{H}_{LC} & 0 & 0 & \iddots \\ \boldsymbol{H}_{LC}^{\dagger} & \boldsymbol{H}_{L} & \boldsymbol{H}_{LC} & 0 & 0 \\ 0 & \boldsymbol{H}_{LC}^{\dagger} & \boldsymbol{H}_{S} & \boldsymbol{H}_{RC} & 0 \\ 0 & 0 & \boldsymbol{H}_{RC}^{\dagger} & \boldsymbol{H}_{R} & \boldsymbol{H}_{RC} \\ \iddots & 0 & 0 & \boldsymbol{H}_{RC}^{\dagger} & \ddots \end{bmatrix} \right) \times \begin{bmatrix} \ddots & \vdots & \iddots \\ \cdots & \boldsymbol{G}_S(E) & \cdots \\ \iddots & \vdots & \ddots \end{bmatrix} = \boldsymbol{I} \tag{3.24}$$

What is required to calculate the current is the central block of the Green's function that corresponds to the scattering region (i.e. the molecule + leads extensions). A reduced version of the last equation then could be written in the following form:

$$\left[(E+\mathrm{i}\tau)\boldsymbol{S}_S - \boldsymbol{H}_S - \boldsymbol{\Sigma}_L - \boldsymbol{\Sigma}_R\right]\boldsymbol{G}_S(E) = \boldsymbol{I} \tag{3.25}$$

Inverting this equation yields:

$$\boldsymbol{G}_S(E) = \left[(E+\mathrm{i}\tau)\boldsymbol{S}_S - \boldsymbol{H}_S - \boldsymbol{\Sigma}_L - \boldsymbol{\Sigma}_R\right]^{-1}, \tag{3.26}$$

where $\boldsymbol{\Sigma}$ is a new matrix added such that the matrix $\boldsymbol{G}_S$ becomes equal to that results from equation (3.24). This new matrix is known as the leads self-energy matrix, and can be calculated (for left lead) as follows:

$$\boldsymbol{\Sigma}_L = \left[(E+\mathrm{i}\tau)\boldsymbol{S}_{LC}^{\dagger} - \boldsymbol{H}_{LC}^{\dagger}\right]\boldsymbol{G}_L\left[(E+\mathrm{i}\tau)\boldsymbol{S}_{LC} - \boldsymbol{H}_{LC}\right] \tag{3.27}$$

where $\boldsymbol{G}_L$ represents the surface Green's function of the left lead, which is the bottom right block of the full semi-infinite Green's function representing the lead. The self-energy matrices, $\boldsymbol{\Sigma}_L$ and $\boldsymbol{\Sigma}_R$, are generally complex energy dependence matrices containing all the details of the electronic structure of the leads and their coupling with the molecule. The broadening in the molecule levels can be described using two matrices, $\boldsymbol{\Gamma}_L$ and $\boldsymbol{\Gamma}_R$, which are defined as the anti-hermitian parts of the corresponding self-energy matrix:

$$\boldsymbol{\Gamma}_{L(R)} = \mathrm{i}\left[\boldsymbol{\Sigma}_{L(R)} - \boldsymbol{\Sigma}_{L(R)}^{\dagger}\right] \tag{3.28}$$

Knowing the Green's function of the scattering region allows us to calculate the current through a molecule by integration over energy spectrum:

$$I = \frac{2e}{h}\int_{-\infty}^{\infty} \mathrm{d}E\,\mathrm{Trace}\left\{\boldsymbol{\Gamma}_L\boldsymbol{G}_S\boldsymbol{\Gamma}_R\boldsymbol{G}_S^{\dagger}\right\}\left[f(E,\mu_L) - f(E,\mu_R)\right] \tag{3.29}$$

The trace term, $\mathrm{Trace}\left\{\boldsymbol{\Gamma}_L\boldsymbol{G}_S\boldsymbol{\Gamma}_R\boldsymbol{G}_S^{\dagger}\right\}$, represents the electronic transmission through the scattering region at the particular energy E and it is of a central importance to the

calculation. Thus in terms of transmission, equation (3.29) becomes

$$I = \frac{2e}{h}\int_{-\infty}^{\infty} \mathrm{d}E\, T(E)\big[f(E,\mu_L) - f(E,\mu_R)\big] \tag{3.30}$$

The transmission $T(E)$ through the scattering region can be expressed as the product of transmission probability per a channel, $T_m(E)$, and the total number of channels available for conduction, $M(E)$. Then equation (3.30) takes the following form:

$$I = \frac{2e}{h}\int_{-\infty}^{\infty} \mathrm{d}E\, T_m(E)M(E)\big[f(E,\mu_L) - f(E,\mu_R)\big] \tag{3.31}$$

This is the voltage and temperature generalised Landauer formula for an electric current flows through a molecular conductor in between two electrodes. At low-temperature, the Fermi-Dirac distributions (3.5) are reduced to step functions, and the integral in equation (3.31) is evaluated between μ_L and μ_R. Also, for low applied biases, the integral is confined to the vicinity of the Fermi level, so that $T_m(E)$ and $M(E)$ may be assumed to take the constant values $T_m(E_f)$ and $M(E_f)$, respectively. Under these conditions, the current can now be written as:

$$I = \frac{2e}{h}T(E_f)(\mu_L - \mu_R) \tag{3.32}$$

Using the fact that $\mu_L - \mu_R = eV$, the conductance ($\mathscr{G} = I/V$) is given by the following two terminals Landauer formula:

$$\begin{aligned}\mathscr{G} &= \frac{2e^2}{h}T(E_f)\\ &= \mathscr{G}_0 T(E_f)\end{aligned} \tag{3.33}$$

In the case of a ballistic regime, i.e. when the mean free path of the electrons in the conductor is much less than the object's length, the transmission probability for all channels is unity, and it follows from equation (3.33) that the conductance will be an integer multiple of $\mathscr{G}_0$. This behaviour was first observed using semiconductor structures at 4 K [135, 136] and also was demonstrated at room temperature on gold contacts [133]. This implies that even a perfect conductor will exhibit a resistance of approximately

$(12.9/M(E_f))$ kΩ. This resistance arises from the interface between the conductor and the contacts. The current is carried in the contacts by infinite number of channels but inside the conductor by only a few channels. This requires the current to be redistributed to the limited number of current carrying channels, causing a bottleneck [135].

3.4 EHT parameters

Since EHT is an semi-empirical method, it depends on a set of parameters that must be chosen prior to performing any calculations. Commonly used values for the Slater coefficients and uncharged energy parameters exist and include the Hoffman [137, 138], Müller [139–141] and Cerda [142] parameter sets [1]. Most of these parameters are applicable to non-self consistent calculation and do not account for the charge transfer and consequently the energy changes owing to that. Owing to the absence of well-known and tabulated values of SC-EHT parameters, they are calculated using the ATOM script which is one of the SIESTA built-in utilities. The ATOM code performs all-electron DFT calculations on an isolated atom and computes the Kohn-Sham energies of each atomic orbital populated with a specific charge. By adding and removing different fractions of electronic charge from an orbital, we can obtain a set of data for the orbital energy against excess charge. Then the values of the parameters are calculated numerically by fitting the resulted data to second order polynomial. It is worth noting that the ATOM procedure fails if the eigenvalue of any occupied state becomes positive. As a result, the range of excess charge is somewhat limited. As shown in the Figure 3.10, a complete electron can be removed, but only fraction can be added to the system. However, the obtained data is sufficient to compute a best fit. It is worth mentioning that, there are separate EHT parameters values for each l quantum number; i.e. one for each of the s, p and d orbitals. The EHT parameters used in our calculations are tabulated in Table 3.1.

3.5 Software packages

Two software packages that are capable of computing transmission spectra were used: SIESTA [144–147] which stands for “Spanish Initiative for Electronic Simulations with

[1] A complete lists of the EHT parameter can be found on Quantumwise web site

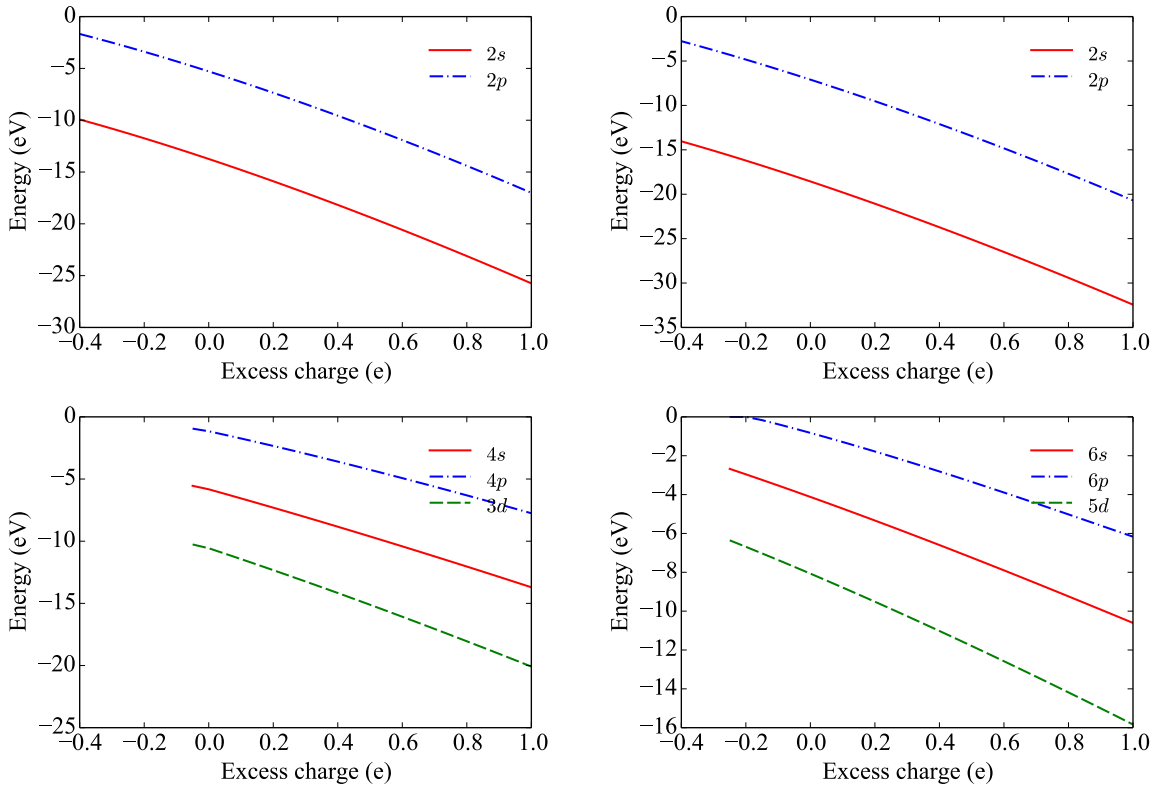

Figure 3.10: A plot of orbital energy against excess charge for the valence orbitals of a single isolated atom. From left to right and top to bottom, the atomic species are carbon, nitrogen, zinc and gold. Over the range shown, the curves are very close to quadratic.

Thousands of Atoms", and EHTransport. SIESTA is an MPI-based DFT code which uses a numerical localised basis set. This set has a strictly limited range (i.e.) rather than the exponentially decaying tail that may be expected for localised atomic orbitals. The basis set is constructed to be exactly zero beyond a certain cutoff distance [148, 149]. This is beneficial for the NEGF calculations for a number of reasons: firstly, the computed Hamiltonian is already in a localised form that makes the calculations straightforward; secondly, the strict cutoff ensures that the matrix is sparse which improves the efficiency of the matrix operations involved in the Green's function calculations. SIESTA also includes the subcomponents Transiesta and TBTrans, which perform the required Green's function calculations [150, 151].

TranSiesta provides the ability of modelling open-boundary systems where ballistic electron transport takes place. Using TranSiesta one can compute electronic transport properties, such as the zero bias conductance and the I-V characteristic, of a nanoscale system in contact with two electrodes at different electrochemical potentials. The method is based on using NEGFs, that are constructed using the density functional

Table 3.1: The EHT parameters set used in the calculations. The α_i and β_i are measured by (eV^{-1}) and the ionisation energies $\mathscr{J}$ in (eV), whereas the respective units of weights c_i and exponents ζ_i are $Bohr^{-3/2}$ and $Bohr^{-1}$. For graphene based systems and atomic chain of gold, the parameters sets are symbolized as $C^{\dagger}$ and $Au^{\ddagger}$ in the Table.

Species	Orbital	$\mathscr{J}$	α_i	β_i	ζ_1	ζ_2	c_1	c_2	κ
H[137]	1s	-13.6	-11.249	-2.454	1.300	NA	1	0	1.75
C[143]	2s	-21.4	-10.321	-1.896	2.100*	NA	1	0	1.75
	2p	-11.4	-9.874	-2.024	1.300*	NA	1	0	1.75
$C^{\dagger}$[137]	2s	-20.316	-10.321	-1.896	2.037	NA	0.741	0	2.25*
	2p	-13.670	-9.874	-2.024	1.777	3.249	0.640	0.412	2.80
B[142]	2s	-21.717	-8.484	-1.824	1.606	0	0.668	0	2.30
	2p	-14.168	-7.100	-1.964	1.636	0	0.990	0	2.30
	3d	-5.554	-0.302	-1.101	0.893	0	0.654	0	2.30
N[137]	2s	-26.0	-12.096	-2.026	1.950	NA	1	0	1.75
	2p	-13.4	-11.665	-2.140	1.950	NA	1	0	1.75
O[137]	2s	-32.3	-13.853	-2.072	2.275	NA	1	0	1.75
	2p	-14.8	-13.424	-2.186	2.275	NA	1	0	1.75
F[137]	2s	-40.0	-15.582	-2.115	2.425	NA	1	0	1.75
	2p	-18.1	-15.147	-2.229	2.425	NA	1	0	1.75
P[137]	3s	-18.6	-8.433	-0.979	2.122*	NA	1	0	1.75
	3p	-14.0	-7.853	-0.946	1.827*	NA	1	0	1.75
S[137]	3s	-20.0	-9.487	-0.994	2.122	NA	1	0	1.75
	3p	-11.0	-8.915	-0.963	1.827	NA	1	0	1.75
Fe[137]	4s	-9.10	-7.590	-1.221	1.900	NA	1	0	1.75
	4p	-5.32	-5.199	-3.229	1.000*	NA	1	0	1.75
	3d	-12.6	-12.113	-2.197	5.350	2.0	0.551	0.626	1.75
Zn[137]	4s	-12.41	-7.100	-1.142	2.010	NA	1	0	1.75
	4p	-6.530	-5.489	-1.412	1.700	NA	1	0	1.75
Au[142]	6s	-12.134	-6.945	-0.506	2.316	NA	0.603	0	2.30
	6p	-6.740	-4.943	-0.990	1.745	NA	0.627	0	2.30
	5d	-14.026	-7.807	-0.633	2.327	5.445	0.376	0.794	2.30
$Au^{\ddagger}$[92]	6s	-10.929	-6.945	-0.506	2.602	NA	1	0	1.75
	6p	-5.550	-4.943	-0.990	2.293	NA	1	0	1.75
	5d	-12.605	-7.807	-0.633	2.292	NA	0.596	0	1.75

* Customized values.

theory where the Hamiltonian is obtained from a given electron density. A new density is computed using the NEGF formalism, which closes the DFT-NEGF self consistent cycle.

EHTransport is a custom written OpenMP based code developed in Cardiff University by Gareth Jones. It uses the semi-empirical Extended Hückel Theory to compute the Hamiltonian of a given system in a localised basis set of Slater orbitals. It also uses the NEGF method to compute the transmission spectra. It is written in C++. For more details, see [92].

3.5.1 Modifications to the EHTransport

The original version of EHTransport code was developed using Microsoft Visual Studio (MVS) to work on Windows machines with the only option to compile the source code via GUI of the MVS. This limits the ability of using EHTransport only for Windows systems. Modifications to the original version of EHTransport were necessary to be made for the code to be compatible with Linux operating system. By doing this we were able to use the code on Raven, the HPC cluster at Cardiff, to run multi-jobs concurrently which increases the productivity of using the code.

The calculation of the band structure requires specifying the lines along which band energies are calculated. The EHTransport code considers only the k-points to be given in terms of the reciprocal lattice vectors. Within the code, these k-points are converted into units of $(2\pi/a)$ using a particular formula. A minor bug was found in the implementation of this formula which led to wrong values of k-points. While, in case of orthogonal unit vectors, this mistake has no effect on the calculations because the terms that contained the error turn to become zero. However, using any other unit vectors to define the lattice e.g. graphene, generates wrong values of k-points which in turn gives incorrect band structure of the system at hand.

It might happen sometimes that a calculation terminates before converging, examples for such cases include: if a job runs over its allocated walltime in a queue, the convergence is not reached within the set number of maximum iterations, etc... While in other cases, the calculation is convergent but a new smaller value for convergent criteria is required. In all these cases, it will be absolutely better to resume the job from the point it stopped or is intentionally terminated rather than starting the calculation from scratch. This important feature was missed in the original version of the EHTransport. Adding such utility requires storing all the necessary information to a hard disc which is necessary for resuming the run of the job. This information includes the overlap matrix, Hamiltonian matrix and the excess charge for each atomic orbitals that are involved in the calculation. The feature of resuming the calculation was added successfully and employed for various cases especially the ones that take long time such as DNA systems.

CHAPTER 4

PORPHYRIN MOLECULES

4.1 Introduction

There has been much interest in the study of quantum transport in molecular nanowires due to their possible importance in molecular electronic devices. As the devices become smaller, it is important to understand the factors that govern the electrical conductance across single molecules. In this chapter, we used the SC-EHT to investigate the effect of various factors on the conductance of the n-porphyrin molecules. In particular, we studied how the conductance varies with the length of the n-porphyrin molecule, the metal atom in the porphyrin ring and the in presence of explicit water molecules.

Since the seminal article by Aviram and Ratner [152], in which the authors demonstrated, by means of a theoretical model, that a single molecule could act as a rectifier, there has been much interest and activity directed towards the possible use of single molecules or molecular arrays in electronic devices. The promise of molecular electronics is in the possible exploitation of its two features: its size and its functionality. In principle, an electronic device can be as small as a single molecule, thus allowing for the fabrication of ultra-small devices. It is, however, the functional aspect that does not only distinguish molecular electronics from conventional electronics, but also allows for its greater flexibility. The prospect of adding molecular components to conventional electronic devices to enhance their function may indeed be the short term driver for greater research into molecular electronics. The molecular energy levels are highly sensitive to the molecular structure and its environment. Thus, it might be possible to engineer different functionalities by tuning the molecular electronic energy levels.

Over the last decade, there has been much interest in understanding the nature of quantum transport in molecular nanowires [153]. This has become more important as efforts in fabricating molecular electronic devices have increased. There have been many measurements of charge transport across single molecules or groups of molecules across metal contacts [154–156], and it is clear that molecular conduction depends on a number of different factors. These include the nature of the molecular bonding at the metal surface, the conformation of the molecule (which is especially important in the case of large organic molecules), the details of the environment and the details of the molecule.

Selzer *et al.* [157] showed that the conductance of a molecule can be orders of magnitude higher in a self-assembled monolayer, rather than as an isolated molecule. They attributed this behaviour to the importance of both environmental thermal effects and electrostatic interactions of neighbouring molecules. Fatemi *et al.* [158] found that solvents increase the conductance of 1,4 benzenediamine (BDA)-Au molecular junction. With reference to calculations, they explained this increase as resulting from a shift in the Au contact work function induced by the solvents. It is not clear if these environmental effects are important in all molecules and so it is of interest to develop a scheme whereby the effect of the various extrinsic factors may be determined and quantified.

The details of the molecule are also very important as they provide the means of tuning the molecule to its desired functionality. Among the many classes of molecules that have been investigated, the π-conjugated porphyrin oligomers have attracted serious attention because they allow for great flexibility in their specifications. Additionally, they can be synthesised into ring and square structures for "light harvesting". Oligomers comprising metal-porphyrin monomer units may be made arbitrarily long. Hence, this system is one in which the conductance as a function of molecular length may be studied in a consistent manner. Thus, the porphyrin group of molecules makes for an almost ideal test system to carry out the conductance calculations.

With this molecular group, thiol end groups may easily be introduced to bond to Au substrates and consequently have been the object of both experimental and theoretical/computational investigations [159, 160]. Another variable of the system is in the type of metal atom at the centre of the ring structure and it is of particular interest to

investigate how the electronic structure of the metal atom and consequently the charge distribution affects the conductance of the molecule. Much of the work reported has been on Zn-porphyrin structures and it is of interest to study other metal-porphyrins, such as the redox-active Fe-porphyrin structures. Finally, the effect of solvents on the conduction can be determined by performing calculations on systems which include water molecules as well as the porphyrin oligomers.

4.2 Results

The n-porphyrin systems studied, in the present work, consisted of porphyrin rings linked together by either two or four carbon atoms. These are referred to as the 2C-porphyrins and the 4C-porphyrins respectively. In order to make a good contact to the gold leads, thiol groups were attached to both ends of the porphyrin molecule. The electrodes were modelled as either Au linear chains or as the (111) surface of bulk gold. The former would correspond to a situation in which the S-atom is adsorbed on to a single Au atom chain, while the latter represents the contact made by the deposition of the molecule on to a Au (111) surface.

In performing the computations, periodic boundary conditions were applied. With the linear chain contact, each electrode comprised 4 Au atoms with spacing 2.51 Å while the extended molecule comprised the porphyrin molecule and 2 Au atoms on either side (Figure 4.1a). The bulk surface Au contacts were taken to be the (111) surface with the lead modelled as 3 layers, each layer consisting of 4×4 atoms. In this scenario, the extended molecule comprised the porphyrin plus 2 Au bulk layers on each side (Figure 4.1b).

4.2.1 Molecular bonding at the Au-contact interface

It is commonly recognised that the particulars of the contact can have a huge influence on the conductance of molecular wires. The interaction between the Au electrode and the molecule determines the electron energy levels and hence the transmission. So, before any conductance calculations were carried out, it was important to establish the optimal contact geometry of the system. In the case of the linear Au contacts, the

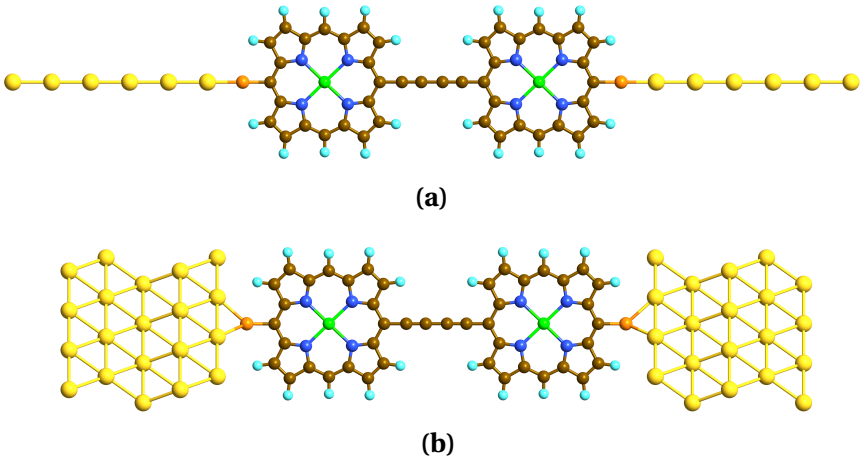

Figure 4.1: Atomic configuration of the porphyrin molecule with the (a) linear chain Au electrodes and (b) with Au(111) surface contacts.

only variable is the Au-S spacing. In order to determine this spacing, the structure of the isolated molecule was optimised by first using classical force fields followed by running the SIESTA code with PBE exchange-correlation and a 300 Ry mesh cutoff to minimise the total energy. Further total energy DFT calculations were carried out on the Au-molecule-Au system with the energy optimised molecular structure and the Au-S distance corresponding to the minimum energy was found to be 2.27 Å.

For the (111) Au-surface contact, there are 4 possible sites for the S-atom to position itself: the atop, the bridge or one of two hollow sites (FCC and HCP) (see Figure 4.2). Again, total energy DFT calculations with these geometries and varying the S-Au surface distances were performed. It was found that the FCC hollow site had the lowest energy, and in subsequent calculations with the bulk surface contact, this was taken as the

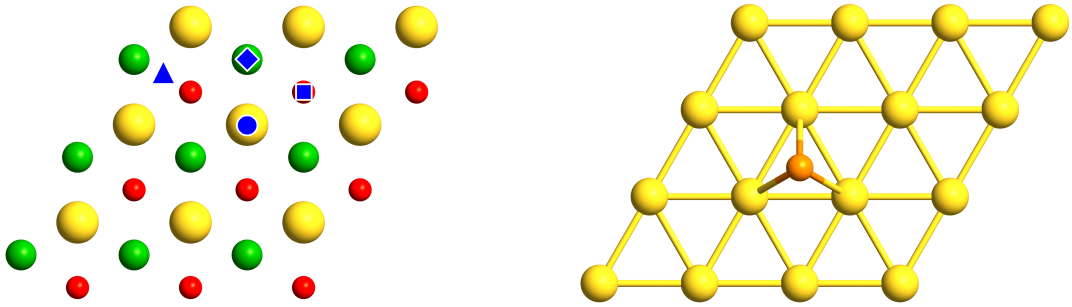

Figure 4.2: (Left) The four possible positions of the sulfur atom to be located on the Au (111) surface. Three layers of gold atoms are shown with C layer (the biggest yellow balls) being on the surface, followed by the B layer (bigger green balls) and A layer (big red balls). The four sites are as follows: atop (circle), bridge (triangle), HCP hollow site (diamond) and FCC hollow site (square). (Right) the top view of the S atom position relative to the Au(111) surface.

adsorption site. This is in accordance with other calculations (see, for example, the review by Häkkinen [161]).

4.2.2 The effect of molecular conformation on the conductance

Having established the contact geometries of the Au-porphyrin-Au system, we investigated the effect of the molecular conformation on the conductance. Previous studies [160] have suggested that at room temperature the molecule has sufficient energy for the two porphyrin rings to rotate, both with respect to the substrate and relative to each other. We considered two types of rotations. First the molecule as a whole was allowed to rotate around the molecular axis. This type of rotation probes the dependence of the local structure at the adsorption site on the density of states and hence the transmission. This effect was found to be very small when compared to the rotation of the porphyrin rings relative to each other. In considering this rotation, which is characterised by the dihedral angle (ϑ) between the two porphyrin ring planes (Figure 4.3a), the potential energy as a function of ϑ was calculated using the DFT code SIESTA. From the results shown in Figure 4.3b, we can see that the potential barrier for relative motion is about 70 meV. This is of a similar order to that found by Kocherzhenko *et al.* [160] in their study of Zn-porphyrin based molecular wires using a generalised charge transfer integral approach. At ambient temperature, the thermal energy $k_B T$ is equivalent to 25.6 meV which corresponds to a dihedral angle of 30° as shown in Figure 4.3b. This indicates that the structural fluctuations need to be considered in the transmission calculations.

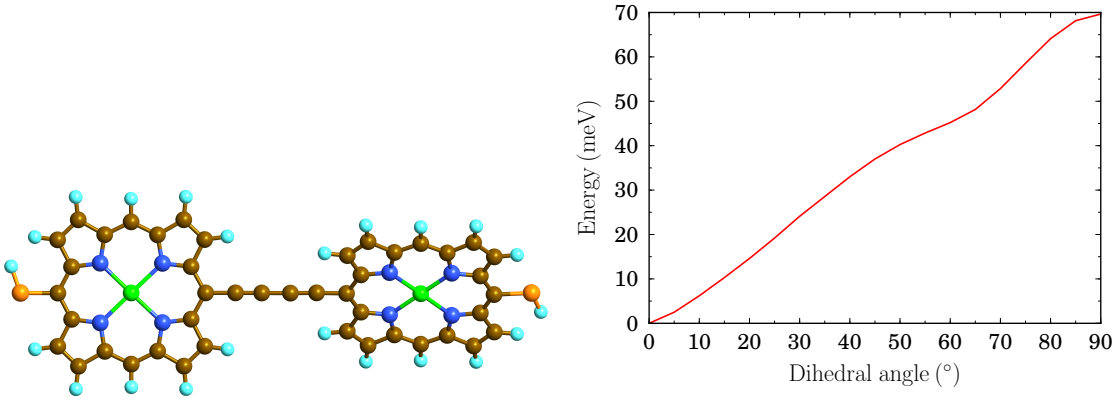

(a) **(b)**

Figure 4.3: (a) The Zn-diporphyrin molecular conformation for dihedral angle $\vartheta = 45°$ and (b) the energy barrier for rotation as a function of dihedral angle ϑ.

As the size of this system was not too large for carrying out DFT calculations, it was seen as a test system which could be used to test the validity of using our SC-EHT approach in conductance calculations. Hence, the electron density of states and the transmission function for varying ϑ were calculated using both the SC-EHT and SIESTA codes.

From the results depicted in Figure 4.4, we see that there is a fair agreement between the results using the two approaches giving confidence in the use of the SC-EHT for these type of calculations. This is especially the case where the interest is in identifying the relative importance of the various factors on the conductance of n-porphyrin molecules. However, there are some differences in the details between the two sets of results. While there is some ambiguity in assigning the Fermi level in a DFT calculation, in EHT, the Fermi levels are defined by the ionization energy. In order to provide a proper comparison between the two sets of results, the energy scale is shifted so that the main peak close to the Fermi level in both calculations are matched. The difference in the order of DOS magnitude appears between the SIESTA and SC-EHT calculations due to the small energy range over which the DOS is displayed. In fact the integration of the DOS over the whole energy range gives almost the same value which actually represents the total number of the electron in the system. The differences in the density of states are not unexpected, and are similar to that seen for example by Tada *et al.* [162] in their study of the transmission in molecular wires when using different basis sets and correlation functionals. Thus, we conclude that the SC-EHT method is a suitable method to use in conductance studies of organic molecules.

Both sets of results (Figure 4.4) show that the transmission reduces as the angle is increased indicating that thermal fluctuations would have the effect of reducing the transmission and hence the conductance. Also, the energy difference between highest occupied molecular orbital (HOMO) and lowest unoccupied molecular orbital (LUMO), E_{HL}, is found to increase with increasing ϑ going from 9.6 meV at $\vartheta = 0^\circ$ to 18.9 meV for $\vartheta = 90^\circ$. This is in contrast with what is observed in the isolated molecule in which E_{HL} is almost independent of the dihedral angle. This reinforces the notion of the importance of the Au contact geometry in determining the conductance and also demonstrates how the contact geometry can act as a constraint on the molecular conformation.

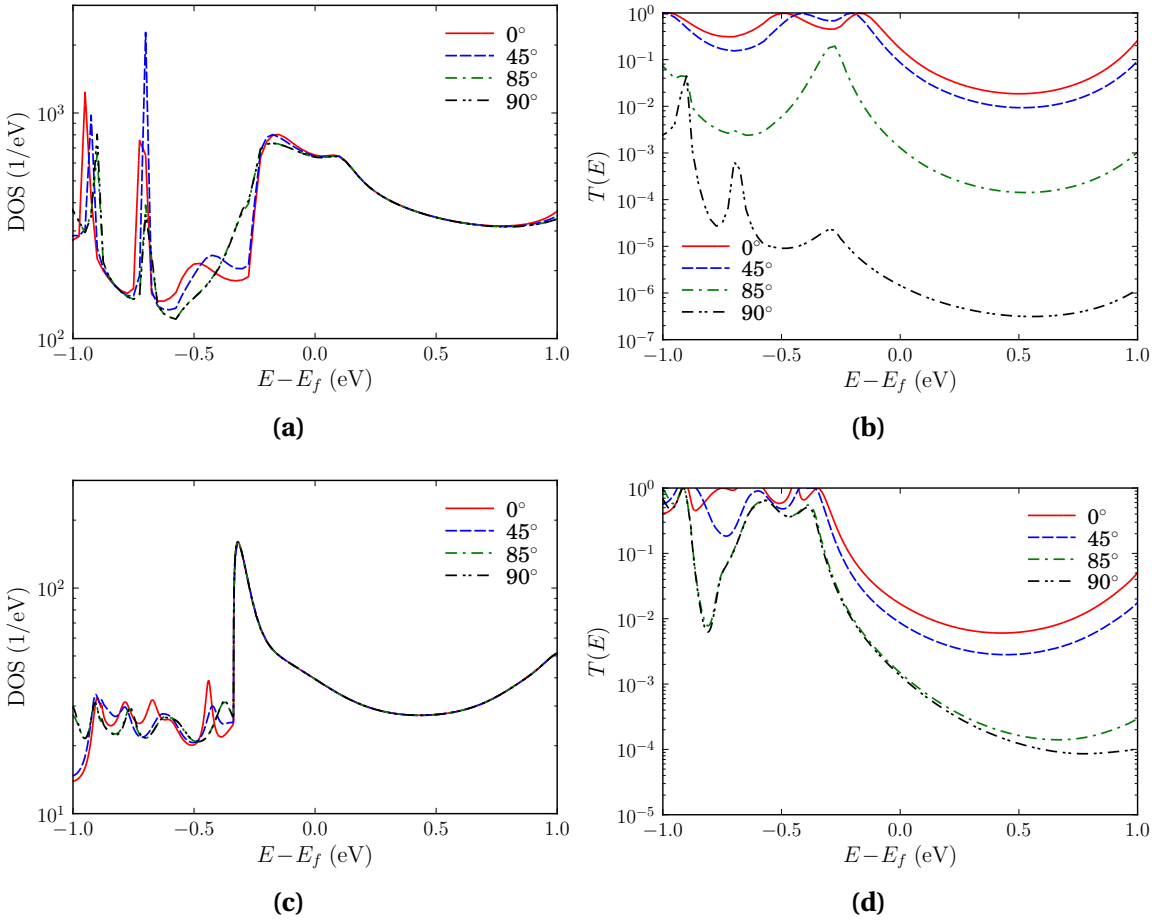

Figure 4.4: The density of states (DOS) and the transmission for different dihedral angles ϑ for the diporphyrin molecule using (a, b) SIESTA and (c, d) SC-EHT for bulk Au contacts.

4.2.3 The conductance as a function of polymer length

The SC-EHT method was then used to investigate the conductance of the 4C-n-porphyrins as a function of the number of porphyrin rings or molecular length. There have been many studies aimed at investigating the length dependence of charge transport in molecular wires not least because of the interest in identifying any crossover from tunnelling to hopping transport (see, for example, Sedghi *et al.* [163]). That particular question is beyond the scope of this thesis as we are using a method that does not take into account vibronic contributions or phonon baths. However, it is still of interest to examine how the conductance varies with length and in particular to see if it deviates greatly from the exponential dependence expected in simple barrier models.

Before investigating the Au-molecule-Au system, the isolated molecule was examined. Electronic structure calculations using the SC-EHT method were carried out on

isolated n-porphyrin molecules as a function of the porphyrin length (which is of course proportional to the number of monomers). The energy gap E_{HL} so determined is plotted in Figure 4.5 as a function of porphyrin length and is well fitted by the function

$$E_{HL}\,(\text{eV}) = 1.537\,e^{-0.028L} + 1.166 \tag{4.1}$$

Thus, the HOMO-LUMO gap for the infinite molecule is 1.166 eV which is good agreement with experiment.

Next, the n-porphyrins were then attached to the gold (111) surface contacts and the density of states, the transmission and the conductance at various energies close to the Fermi level are determined. While the HOMO energy level remains fairly constant with length, the LUMO energy level is found to shift towards the Fermi level resulting in a narrowing of the gap, E_{HL}. The magnitude of this gap energy is less than that seen for the isolated molecule.

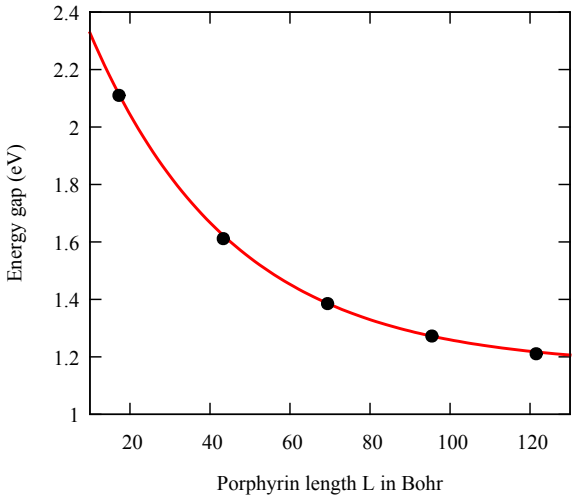

Figure 4.5: The variation of the energy gap, E_{HL} for the isolated molecule as a function of the n-porphyrin length. The line shows the exponential best fit curve.

The dependence of the transmission on molecular length is more complicated (Figure 4.6b). We see that in the energy region just below the Fermi level, there is sizeable decrease in transmission, but just above the Fermi level, the shift in LUMO energy level results in an increase in transmission at specific energies. This is a consequence of the downward shift of the LUMO energies. We would therefore expect non-linear I-V characteristics for these systems. In order to compare our results with those of other workers, the conductance as a function of molecular length was calculated for a few

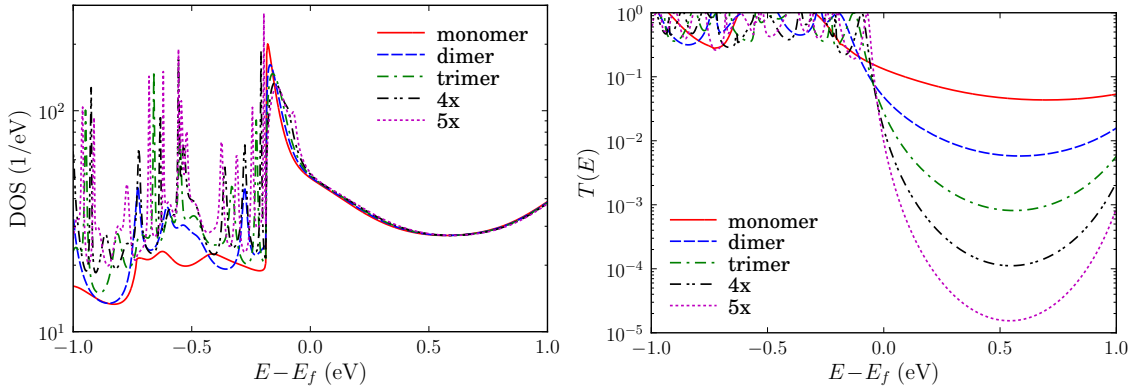

(a) **(b)**

Figure 4.6: The DOS (a) and transmission spectra (b) of a zinc-porphyrin wire of various lengths between two bulk Au electrodes.

energies in the region where the transmission decreases with increasing molecular size (Figure 4.7b).

The conductance, shown in Figure 4.7b, does display the expected exponential decay with length

$$\mathscr{G} = \mathscr{G}_0 \, \mathrm{e}^{-\beta L} \tag{4.2}$$

with β equals to 0.149 Å^{-1} and L is the separation between the two sulfur atoms. In their investigations on the tape porphyrin system, which would be expected to have a slower tail off, Tagami *et al.* [159] also found a exponential dependence with $\beta \approx 0.0095$ Å^{-1}. Sedghi *et al.* [164], in a study of a homologous series of butadiyne-linked oligo-porphyrins, found a remarkably shallow decay of the conductance with molecular length with an attenuation factor $\beta \approx 0.04$ Å^{-1}. This attenuation value is of course smaller than those found for oligo-para-phenylenes ($\beta \approx 0.4$ Å^{-1}) [165] or for the oligothiophenes $\beta \approx 0.1$ Å^{-1} [166].

4.2.4 The effect of changing the metal ion in the porphyrin ring

As mentioned in the introduction of this chapter, one of the advantages of introducing molecular wires in electronic devices is due to the potential changes in functionality arising from small modifications to the molecular composition and structure. In the metal-porphyrin system, the type of metal atom at the centre of the porphyrin rings can be viewed as a functional modifier. Most of the work done to date on the porphyrin systems has focussed on the Zn porphyrins. In order to get a better understanding

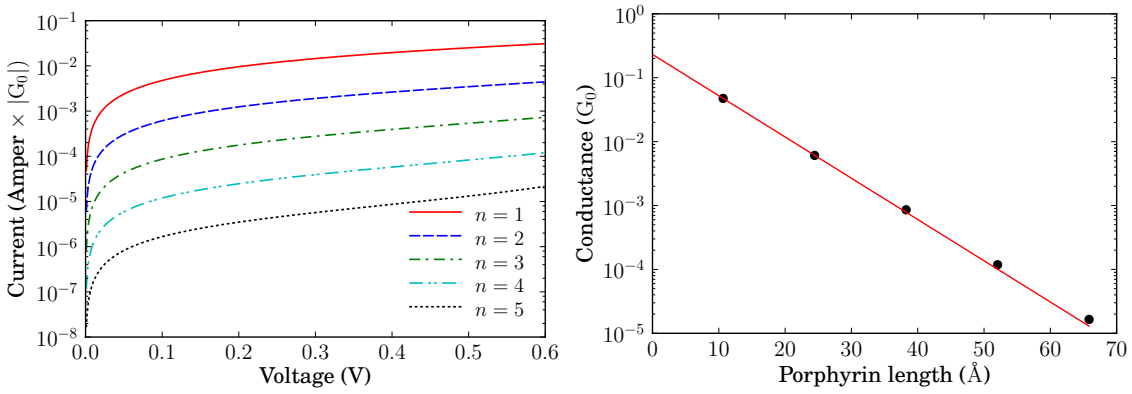

(a) **(b)**

Figure 4.7: The I-V characteristics at temperature 298 K (a) and conductance at bias voltage 0.25 V and temperature 298 K (b) for a zinc-porphyrin wire of various lengths between two bulk Au electrodes.

of the possible influence of the metal atom in the conductance process, we computed the bond current pathways and the localised charge distribution in the molecular wire complex with either Zn or Fe metal atoms occupying the centre of the ring structures. The bond current pathways show the bonds along which the electrons (holes) move during transmission. This is, of course, intimately connected to the localised charge densities on the molecule.

For the Zn-4C-porphyrin wire, the current flows along the bonds around both sides of the ring structure without passing through the metal atom (Figure 4.8a). A detailed analysis of the charge densities and conduction shows that the Zn atoms have an excess of 0.22 electrons and that the conduction around the ring structure is carried by the p-orbitals. So, the electrons on the C-skeleton (the π orbitals) are the primary conduits for charge conduction in this system.

With the Zn atoms replaced by Fe atoms, the electronic structure and density of states are modified such that metal atoms are now positively charged (charge excess of +0.15 e) and new localised states are seen around the Fermi energy (Figure 4.9a). These changes have a profound effect on the conductance. Now, the charge carriers no longer go around the ring structure, but instead pass through the metal atom due to coupling with Fe d-states (Figure 4.8b). The effect of this is to increase the conductance at E_f (Figure 4.9b).

The main conclusion to be drawn from this part of the present study is that the charge carrier paths depend on the nature of the metal atom at the centre of the ring. In particular, there is a clear distinction between donor and acceptor metal atoms. This

could have implications for molecular engineering, especially where the robustness of the molecule becomes an important factor.

4.2.5 Modifications of the conductance due to the inclusion of solvent molecules

Extrinsic or environmental factors have an important influence on the conductance of a molecule [167]. Recently, Fatemi *et al.* [158] measured the conductance at individual BDA-Au molecular junctions using a STM based on break junction techniques and found that the presence of solvents can increase the conductance by as much as 50%. They ascribed this increase to a shift in the Au contact work function resulting from solvent atoms binding to it. It is clear from this and other studies [167] that the solvent and counter-ions can have a profound effect on molecular conduction. We have endeavoured to address this issue by carrying out conductance calculations on the Zn-porphyrin molecular system in the presence of explicit water molecules representing the solvent. This was done by introducing water molecules directly into the computational cell. Water molecules were randomly placed throughout the unit cell with the proviso that there were no other atoms within a range of 4 Bohr of the O-atom or within 3 Bohr of the H-atom of each water molecule. The resulting system, with 59 water molecules added to the system and corresponding to a density near to 60% of normal density of water is shown in Figure 4.10.

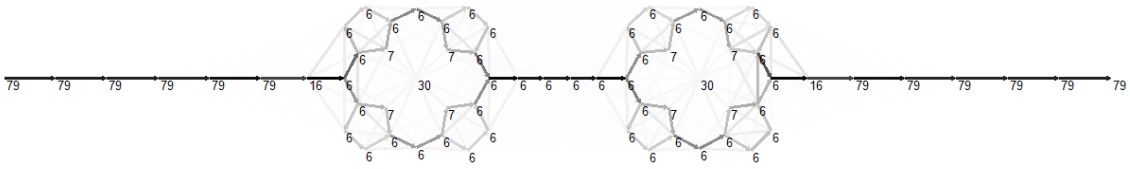

(a)

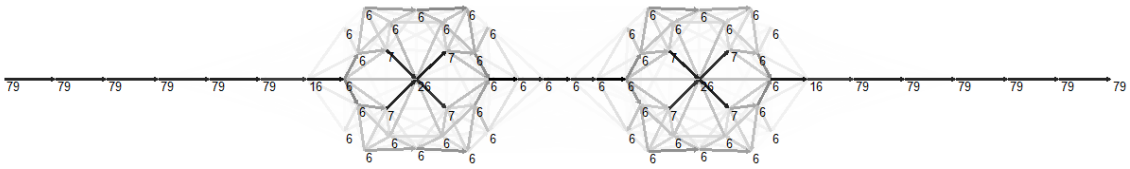

(b)

Figure 4.8: Bond current plots for (a) the Zn-porphyrin and (b) the Fe-porphyrin molecules between linear Au electrodes at energy equal to E_f.

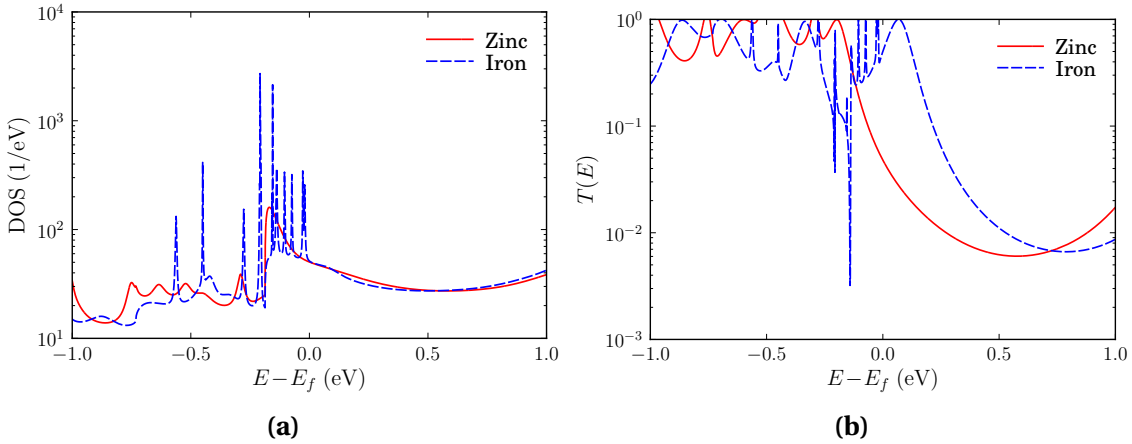

Figure 4.9: (a) Comparison of the electron density of states of the Fe-porphyrin and Zn-porphyrin molecules and (b) the transmission for the Fe-porphyrin molecule as compared with Zn-porphyrin between linear Au electrodes.

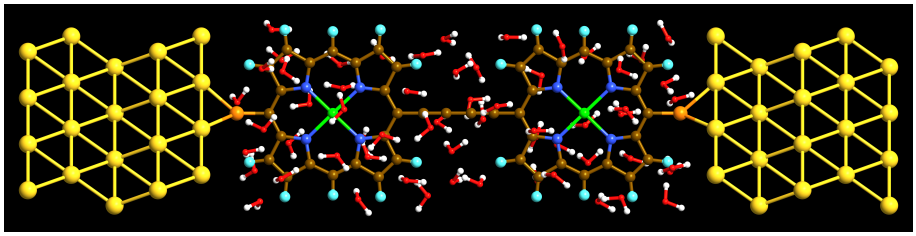

Figure 4.10: The computational unit cell with water molecules added to the Zn-porphyrin dimer in between bulk Au electrodes. For clarification, the hydrogen atoms of water molecules and those bonded to carbon have been visualised using white and cyan balls respectively.

Although the distribution of real water molecules in the vicinity of a molecule and a surface is known not to be random, these calculations are meant to illustrate the sensitivity of molecular conductance to the presence of water. Furthermore, in performing the calculations we have also considered the possible effects of the polarisability of the water molecules on the molecular conductance. To do this, two sets of calculations were carried out; one with the water molecules randomly oriented and the other with the water molecules polarised along the direction of the applied voltage.

A comparison of the density of states resulting from these separate calculations (Figure 4.11a) shows that most of the prominent features arising from the presence of water are to be found in the energy range −1 to −0.5 eV relative to E_f and around the Fermi energy. These new states cause the transmission to increase quite sharply around the Fermi level E_f.

The change in the DOS around the HOMO level results in the observed increase in transmission (Figure 4.11b), The effect of the LUMO level changes are barely noticeable

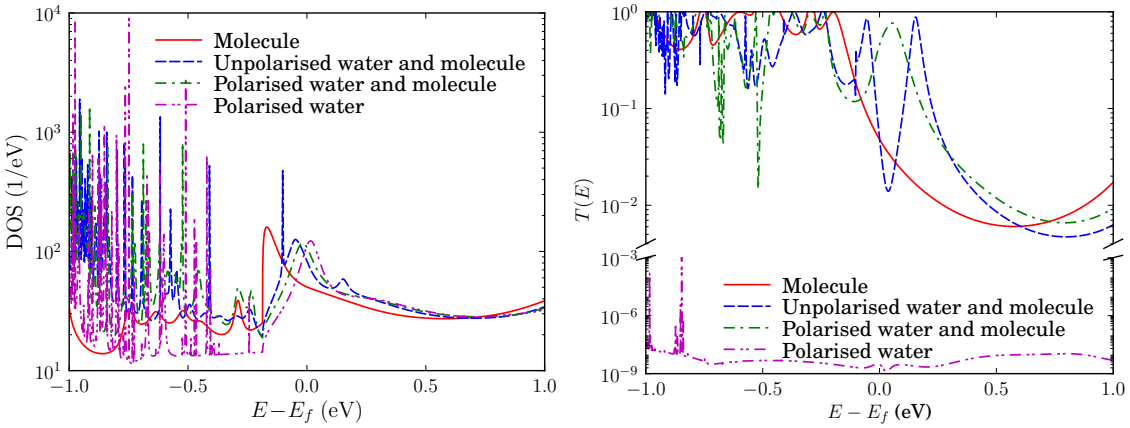

Figure 4.11: (a) The electron DOS and (b) transmission spectra for the Zn-diporphyrin molecule in unpolarised and polarised water. The results with the water on its own between the bulk Au electrodes are also shown. The y-axis of the transmission spectra was broken and different scale used for the transmission spectrum of water for better visualization.

as the shift in the LUMO energy is quite small. So, the presence of the water molecules appears to have more of an effect on hole transport for this molecular system. The increase in conductance at energies just below E_f is similar to that reported by Fatemi *et al.* [158]. In order to understand how the water molecules affect the transmission, a localised charge distribution plot was made and this is shown in Figure 4.12. The gold electrodes become charged inducing a shift in the surface work function. This is what gives rise to an upward shift in the HOMO energy level towards the Fermi energy. The increased conductance support the findings of Fatemi *et al.* [158].

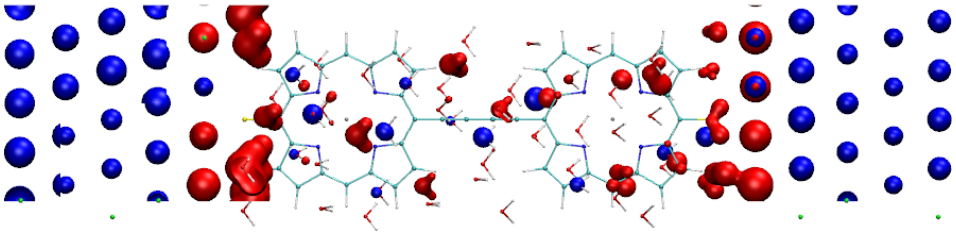

Figure 4.12: The localised charges in the computational unit cell containing polarised water molecules along with the Zn-diporphyrin between bulk Au electrodes. Here red denotes negative charge and blue is positive.

An examination of the bond current plots in Figure 4.13 for this system at E_f shows very little difference from that obtained without the presence of water. This is only to be expected as the transmission plots would suggest this. At 2 eV below E_f, the electron states of the water become dominant and can be accessed resulting in conduction

between the electrodes through the water. So, we see that at different biases, different components become important in charge transport.

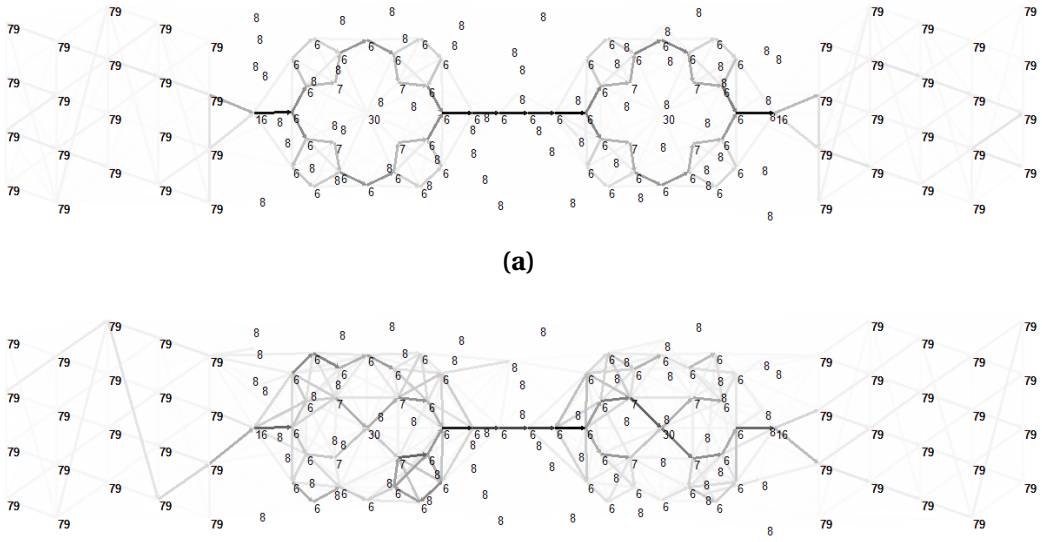

(a)

(b)

Figure 4.13: Bond current plots for the porphyrin molecule + water between bulk Au electrodes at energy equal to (a) E_f and (b) $E_f - 2$ eV.

4.3 Conclusions

We have undertaken a comprehensive study to investigate the relative influence of various factors on the electrical conductance of molecular wires, taking the Au-porphyrin contact as the test system. With a view to performing large system calculations beyond the scope of DFT *ab initio* calculations, we have employed a SC-EHT code that has been tested against the DFT code, SIESTA, for the Zn-di-porphyrin molecular wire. The relatively good agreement supports the tenet that this semi-empirical approach is useful in undertaking such studies.

The SC-EHT code was then used to investigate the transmission and conductance of the porphyrin system as a function of the molecular length and on the metal atom inside the ring structures. The length dependence was found to be exponential in form which is in broad agreement with the results of similar studies. The d-states of the Fe-ion in Fe-porphyrin are found to be responsible for the increased conduction around E_f. This, together with the observed conduction pathways, have implications in developing molecular electronics with varying functionality.

Finally the effect of environment in the form of introducing explicit water molecules on the molecular conductance was studied. The presence of the water molecules was found to induce shifts in the Au surface work function which in turn causes the HOMO level to shift closer to the Fermi level so increasing the conductance.

In conclusion, the SC-EHT method has been shown to be a useful approach in the study of electrical conduction of relatively large molecular systems. The importance of the environment on the single molecule junction transport has also been demonstrated.

CHAPTER 5

DNA BASED SYSTEMS

5.1 Introduction

Although the nucleic acids were first discovered in 1869 by Friedrich Miescher, their chemical structure were not fully perceived until the early 1940s. Basically, nucleic acids are divided into two main types: deoxyribonucleic (DNA) and ribonucleic (RNA). A DNA molecule is composed of two strands that twist together to form a double helix. Each individual strand is a repeated pattern of a small building unit called the nucleotide which in turn consists of three subgroups of molecules: pentose sugar, phosphate group, and organic base. The first two are bound to each other forming what is called the backbone to which the organic bases are attached. Two different kinds of pentose sugar exist in nucleic acids: ribose and deoxyribose which are solely present in RNA and DNA respectively. The only difference between them, as shown in Figure 5.1, is the absence of an oxygen atom in the deoxyribose sugar. The final piece of the nucleotide building unit is the base. Four different bases can be found in DNA (their structural formulas are shown in Figure 5.2): Adenine (A), guanine (G), cytosine (C) and thymine (T) [1]. Interestingly, although there are four bases, each base on one strand is always paired with just specific base on the opposite strand. In particular, adenine binds to thymine while cytosine binds only to guanine. The coupling between a base and its complimentary counterpart occurs through hydrogen bonds. This arrangement of the two bases binding together across the double helix is called a base pair and the list of bases attached to a single strand is known as base pair sequence.

[1] A fifth base uracil (U) also occurs in nature, but is typically found incorporated into RNA strands rather than DNA, where it substitutes for thymine.

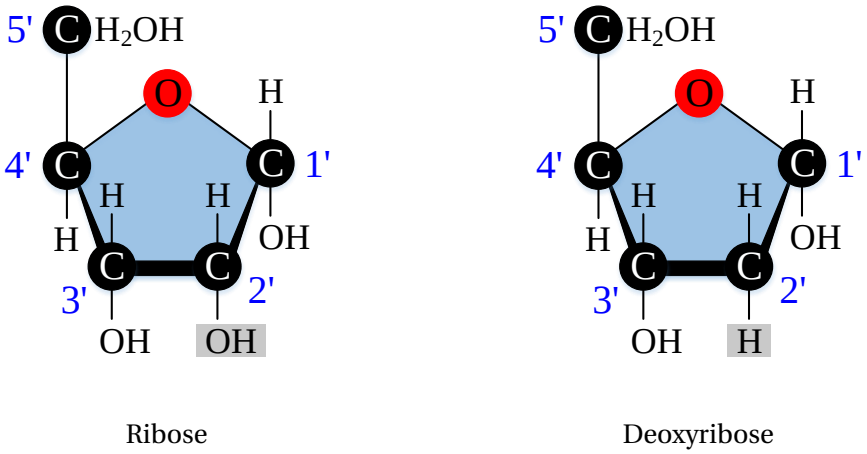

Ribose Deoxyribose

Figure 5.1: The two types of pentose sugar present in nucleic acids. The carbon atoms in the pentose ring are numbered from 1 to 5 with a small dash by each number. This labeling is necessary to distinguish conveniently where the other building units of the DNA and RNA are attached.

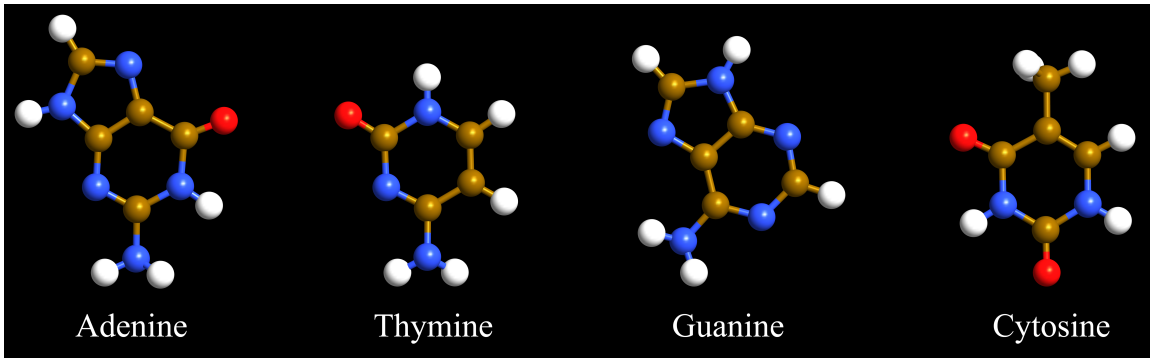

Figure 5.2: The structure of the four bases that form DNA. The atoms in the structures are: hydrogen (white), carbon (brown), oxygen (red) and nitrogen (blue).

DNA can exist in different conformations depending on several factors of which the hydration level and surrounding environment are the most important ones (Figure 5.3). The two main forms of DNA that are of interest in this study are known as A-DNA and B-DNA [168–170]. The B-DNA is the most common naturally formed which is found under physiological conditions that occurs at the high levels of hydration (more 90% [168]) and presents in living cells. When humidity levels drop below 75%, we have dry DNA and the structure of the molecule changes into the A form. Z-form is a third conformation of DNA which is found in a living cell with traces. The Z-DNA is unstable and is not found individually. Instead, it is a transient structure that is occasionally induced by biological activity and then quickly disappears [171].

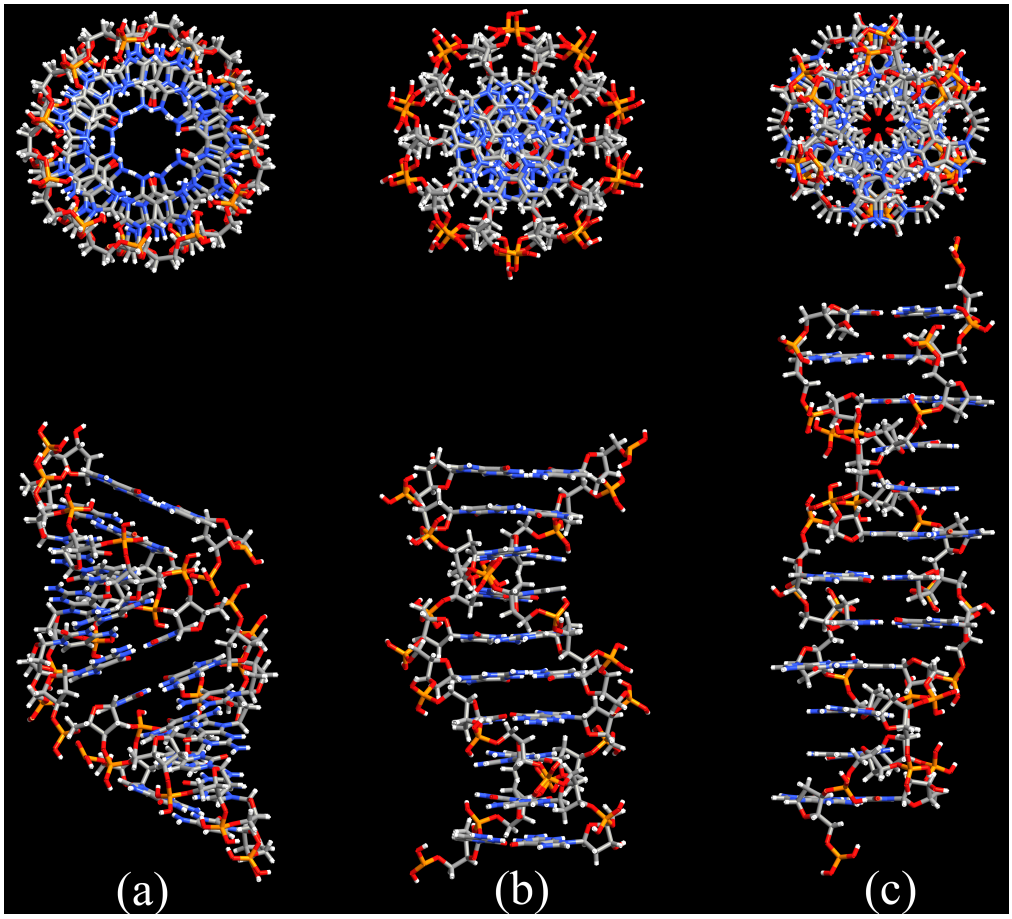

Figure 5.3: Top and side views of (a) A-, (b) B- and (c) Z-type DNA, where one full turn is formed by 11, 10 and 12 base pairs, respectively. When moving to the next base pair on A-, B- and Z-type DNA, the height increases by 2.56, 3.38 and 3.70 Å and the rotation angle by 32.7°, 36.0°, and 30.0°, respectively.

The side and top views of the three DNA forms are shown in Figure 5.3 with one full turn of each. We can notice that the atomic arrangements are significantly different. Firstly, the stacked bases are aligned perpendicular to axis of the helical structure in B- and Z-DNA and at an angle in the case of A-DNA. Secondly, the twisting angle has also changed. In the case of B-DNA, the angle between stacked base-pairs is 36° whereas in A-DNA, it is 32.7°. This means that we need ten base pairs in the former case and eleven in the latter in order to have one full turn of the double helix structure (a periodic cell) in the solid state sense.

Conduction through a DNA molecule of repeating base pair sequence is thought to occur through the π bonds of the base pairs [172]. This conduction mechanism is similar to what occurs in certain stacked aromatic crystals, like Bechgaard salts, which behave as metals. This mechanism of charge carriers transferring in DNA suggests that

the base sequence can be very important since the π-orbitals of the individual bases may be different. Moreover, the conformation is important because it determines the overlap between the base pairs. Finally, in order to have a measurable electrical current in a DNA junction, it is crucial to make sure that the π-system hybridizes strongly with the metallic states of the lead atoms.

Over the last twenty years, it was reported that it was possible to measure charge motion across a double helix DNA segment [172–179]. The charge transfers were found to occur over long distances (up to 4 nm) leading to the possibility of using DNA in nanodevices. However, many of the subsequent experimental findings appear to give seemingly contradictory results. Thus, it has been shown that DNA acts as an insulator [180], semi-conductor [181] or conductor [182–185] and even in some exceptional case induced-superconductor [186]. Different reasons can affect the DNA conductivity and lead to really complex behavior of the DNA and experimental discrepancies in the results:

1. The base sequence,

2. The DNA structure (A-, B-, or Z-type),

3. The DNA-contact interface topology,

4. The environment surrounding the examined DNA sample, and finally

5. The length of the DNA segment.

The first two dependences refer to the importance of the electronic structure and correspondingly to the orbital overlap across the molecule. The length dependence of the conductance gives some clues as to the mechanism for charge transport. With much interest in exploiting the functionality of biomolecules in molecular electronics, the self-assembling and self-recognition properties of DNA lends itself to being an important molecule in this field.

In performing the conductance calculations, there is a number of aspects that need to be considered. In this chapter, these aspects are discussed in detail.

5.2 Calculation details

5.2.1 The geometry of the leads

The (111) surface is often the one used in experiment, although the (100) surface is sometimes favoured in theoretical calculations due to the smaller repeating unit and typically smoother transmission spectra from the Green's function method [92]. In the (111) direction, the gold atoms form planes with a repeating ABC structure. The lead principal layer consists of 3 planes, i.e. one single ABC group which is the smallest possible repeating unit. The scattering region contains 5 gold layers, in an ABCAB - molecule - BCABC pattern. The repeat of the B layer allows for simple positioning of the molecule with symmetric contacts. A bulk gold calculation was carried out with SIESTA to compute the optimal unit cell size. This calculation utilised a single orthogonal FCC unit cell, containing two gold atoms. This cell was found to have length 4.134 Å which corresponds to 2.92 Å of Au-Au bond length. The calculations using bulk contacts used a $4 \times 4 \times 5$ gold surface for each contact in the scattering region, which was found to be sufficient to avoid (or neglect if any) interactions between periodic images of the DNA molecule. One principal layer of the lead consisted of three layers of gold atoms, or a single period of the periodic structure along the (111) lattice direction. In total, there were 160 gold atoms within the scattering region. Despite the periodicity, due to the large size of the DNA systems, calculations were performed at only one point- the Γ point.

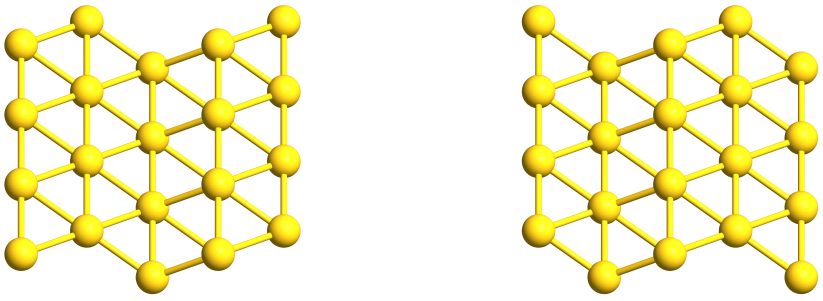

Figure 5.4: The pattern ABCAB-BCABC where the molecule of interest is sandwiched in between two gold bulk electrodes. The direction of conduction is from left to right.

5.2.2 DNA geometrical structure

In the present calculations, the DNA structures were generated via the web interface of the application W3DNA [187]. For our calculations, an initial base pair sequence was entered and a pdb [2] file containing the atomic coordinates created. This pdb file was fed back into W3DNA to generate a base pair file containing the sequence and positioning of the bases. This was modified as required in order to introduce mismatched base pairs or other alterations to the sequence and fed back to W3DNA to generate a second pdb file containing both atomic positions and bond information. The utility software package Avogadro [188, 189] was then utilised to add the H-atoms to the skeleton structure assuming a neutral pH. Avogadro is also used to add the thiol groups by replacing one of the hydrogen atoms at the ends of DNA strand by sulfur.

5.2.3 The position of thiol linker

Among the four different positions for the sulfur atom to be bound to the Au (111) surface as illustrated in Figure 4.2, the FCC site was found to be the most energetically favourable one [92, 161]. Since a DNA molecule consists of two interwoven strands, there is a choice as to which of the two backbones are connected to the Au leads. Calculations were carried with two configurations as shown in Figure 5.5: one with both Au leads attached to S-atoms on the same backbone using 3' and 4' carbon atoms (labeled 3'-4') and the other having the Au contacts attached to S-atoms on different backbones using 3' and 3' carbon atoms (labeled 3'-3'). The results for both configurations are broadly similar, although there are some differences which are referred to later.

5.2.4 Adding water molecules

To investigate the influence of water on the DNA conductivity, water molecules were added randomly to the Au-DNA-Au system using a python script. The water molecules were placed between the two gold leads within a virtual cubic box which contained the whole DNA fragment. Minimum distances of 4 and 3 Bohr have been employed to separate any oxygen or hydrogen atom of a water molecule from the other atoms

[2] pdb stands for Protein Data Bank. A pdb file is a textual file format describing structures of molecules.

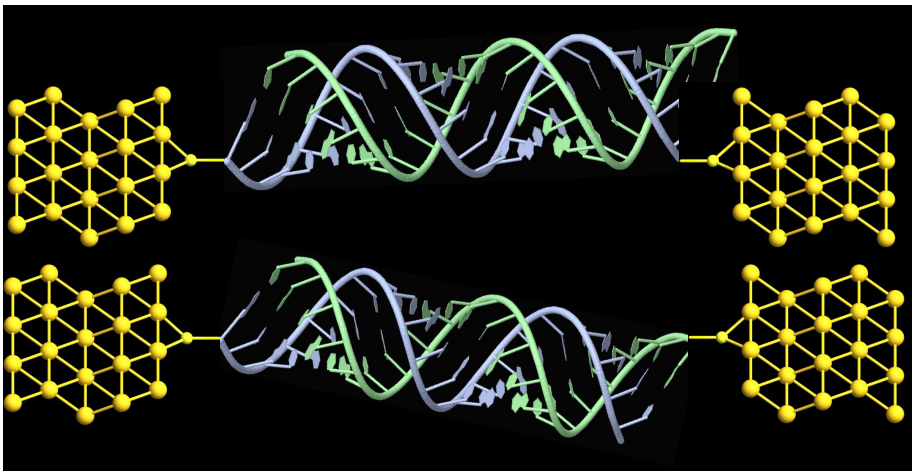

Figure 5.5: The two configurations of connecting a DNA molecule to Au(111) leads via the sulfur thoil (top) S-atoms are attached to different backbones using 3' and 3' carbon atoms (labeled 3'-3'). (bottom) S-atoms are attached to the same backbone using 3' and 4' carbon atoms (labeled 3'-4').

respectively. Different water density systems were considered. The density of water is determined by dividing the total volume of the cubic box by the effective volume occupied by a water molecule at the standard conditions. Table 5.1 shows the number of water molecules required to be added for each system to obtain a density of one gm/cm^3.

5.3 Results

The results of the SC-EHT and conductance calculations as the different factors were varied are presented below. In the first instance, the effect of the contact of the DNA molecule with the leads was investigated. This was followed by varying the DNA fragment length and sequence order. Finally, the effect of the environment was studied by the introduction of water molecules into the system.

Table 5.1: The total number atoms N_{total} for the system Au-S-[$(CG)_n$+H_2O]-S-Au and the number of water molecules N_{H_2O} added to obtain a density of one gm/cm^3.

DNA segment	N_{H_2O}	N_{total}
$(CG)_3$	491	2027
$(CG)_4$	625	2559
$(CG)_5$	696	2902
$(CG)_6$	687	3005

5.3.1 The importance of contact leads

The DNA sample is often connected, in experiments, to the electrodes by a thiol group [3] linker using 3' and 5' ends of the same backbone. This linker, with general the formula: R-SH where R is an alkyl or aryl group, contains many atoms meaning that is long enough for easy fabrication and for setting the system. However, in the current work we used only sulfur atom as a linker between the leads and the DNA sample. Our choice for using the carbon atoms 3'-3' and 3'-4' is determined by the best possible configurations among others to prevent any interfacing between DNA atoms and the leads.

The thiol linker was attached to the DNA by replacing one of the hydrogen atom in pentose sugar ring, at the two ends of the same backbone or the opposite ones, by sulfur atom. Then the semi-empirical geometry optimization algorithms in Avogadro was used to refine the S atom position. Among different positions of the S-atom, only two were suitable for the calculation. This is because the other positions make the DNA atoms very close to leads or even interfere leading to unphysical situation. Therefore, using a larger thiol has the advantage of offering more options and flexibility in selecting the carbon to which the thiol is attached. The DOS and transmission calculations were carried on $(CG)_n$ DNA sequence ($n = 3-6$) using the two configurations. Figure 5.6 shows a typical results for the $(CG)_4$ case. It is noticeable that using the same backbone to connect between the DNA and the leads produces higher transmission probability for the charge carriers especially above the Fermi level. This trend was found in all $(CG)_n$ sequence. These differences in the DOS and transmission might be caused by the short distance separating between the leads and the DNA in the case of (3'-4') as shown in Figure 5.5. This means that some of the current can follow into the DNA not only though the S-atom but also through DNA atoms itself.

5.3.2 The effect of DNA fragment length on the conductance

The conductance of DNA fragments comprising different sequences has been widely explored. These include measurements on polymer units comprising a single nucleobase, eg. poly(G), or single base pairs, eg. poly(CG), or indeed mixed base pair sequences. In

[3] Thiol group is a organic sulfur compound composed of an alkyl or aryl group and a sulfur-hydrogen group.

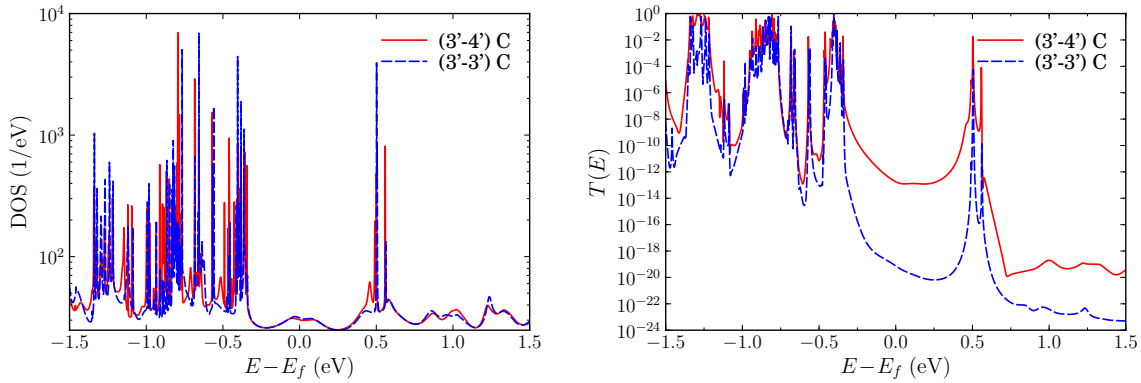

Figure 5.6: The DOS (left) and transmission spectra (right) of a DNA molecule of $(CG)_4$ strand trapped between gold surfaces (111) using different positions of attaching the sulfur atoms to the DNA backbones, namely, (3'-3') C of the same backbone and (3'-4') C of opposite backbone.

order to investigate the conductance dependence on fragment length, we have carried out calculations on $(CG)_n$ sequences for $n = 3$, 4, 5, and 6. The experiments indicate that a sequence of repeating CG base pairs give the best conductance and that this decreases with increasing length according to an inverse power relation [183].

As the HOMO and LUMO energies play a significant role in the transmission function, these are plotted in Figure 5.7a as a function of the number of CG units. We see the expected reduction in the HOMO-LUMO (H-L) gap which is consistent with measurements of Xu *et al.* on the thiophenes [190]. The excess charge plot on the $(CG)_3$ DNA fragment (Figure 5.8) shows a depletion of electrons from the Au electrodes which go to the DNA molecule.

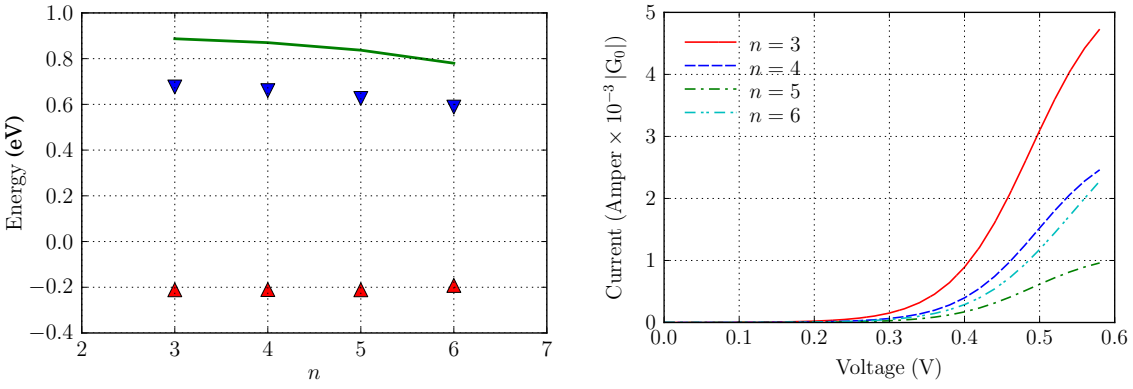

(a) **(b)**

Figure 5.7: (a) The HOMO (up triangle) and LUMO (down triangle) energies together with the H-L band gap (full line) as a function of (CG) base pairs. The HOMO-Fermi energy separation has been fixed. (b) The I-V characteristics of DNA molecule of various lengths in between Au (111) surfaces. The sulfur atoms are attached to (3'-3') C atoms of the opposite backbones.

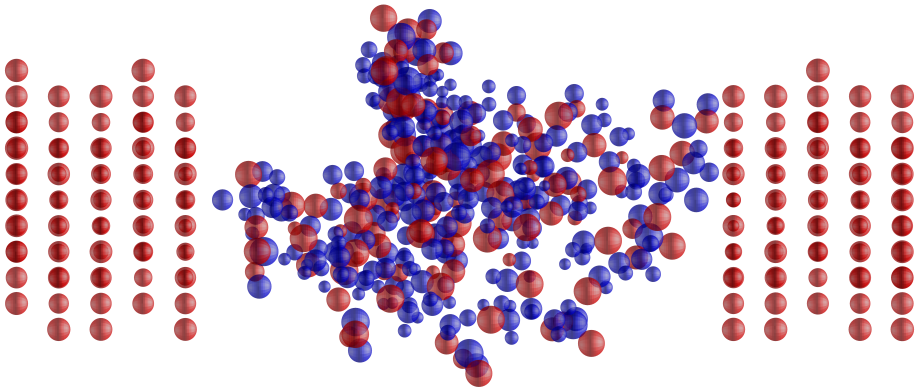

Figure 5.8: The xz view of the excess charge plot on the $(CG)_3$ DNA fragment between two gold electrodes. The spheres are centered on each atom with the blue denoting electron excess and the red pointing to a depletion of electrons. The size of each sphere was made proportional to the magnitude of the excess charge on each atom.

The DOS and transmission spectrum of various lengths of DNA fragments are depicted in Figure 5.9. Although the differences in $T(E)$, as the number of base-pairs is increased, is seemingly very small, the I-V plots shown in Figure 5.7b demonstrate the sensitivity of the conductance on the $T(E)$ resolution. From the I-V plots, the conductance is readily obtained and the results are given in Table 5.2 for varying base-pair numbers for both types of contacts to the Au surface. The general trend of the reduction in conductance with length is clear. Also, it may be seen that this is not an exponential decrease but is more in agreement with the inverse length dependence as reported by Xu *et al.* [183].

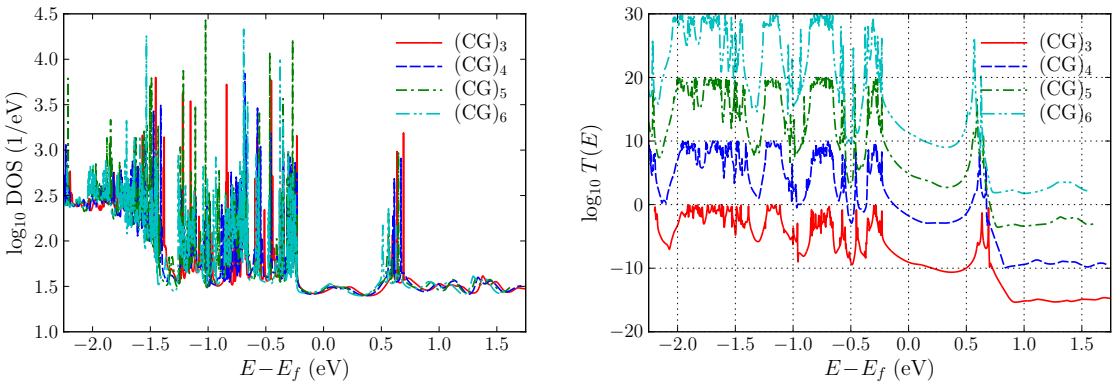

(a) **(b)**

Figure 5.9: (a) The logarithm of the DOS and (b) transmission coefficient for the $(CG)_n$ sequences at 298 K. The scale on the vertical axes is for the $n = 3$ sequence. The other transmission curves are shifted up by 10 units successively in order to display the changes.

Table 5.2: The conductance $\mathscr{G}$ in $10^{-3} \times \mathscr{G}_0$ unit at 298 K and 0.5 V for the varying lengths and different surface contact geometries.

DNA segment	3'-3'	3'-4'	Average
$(CG)_3$	6.187	8.431	7.309
$(CG)_4$	3.045	3.658	3.352
$(CG)_5$	1.233	6.349	3.791
$(CG)_6$	2.355	0.448	1.402

5.3.3 The effect of DNA sequence on the conductance

While the conductance of $(AT)_n$ sequences has been found to be of similar magnitude to $(CG)_n$ sequences, the addition of AT base pairs into a poly (CG) sequence has been found to reduce the conductance [183]. Other studies investigating sequence dependence considered the examining of the substitutional disorder effects and the removing or adding of nuleobases into a particular sequence. We investigated the effect of incorporating sequence disorder into the DNA fragment, by substituting (CG) base-pairs with (AT) base-pairs in the $(CG)_6$ hexamer. For this particular fragment, we carried out the calculations on the $(CG)_2AT(CG)_3$ and $(CG)_2(AT)_2(CG)_2$ hexamers and compared the results with the original $(CG)_6$ hexamer. We found that the effect of these substitutions is to induce a shift in the HOMO and LUMO energy states such that the H-L gap increases with the number of (AT) pairs. Although these findings are limited to fairly small number of base pairs, this trend should hold true for increasing the number of base pairs. Figure 5.10 shows the DOS and the transmission for the three different hexamers studied on the same axes to highlight the differences. As can be seen, the effect of introducing (AT) base pairs increases the H-L gap which reduces the conductance. The substitution of one (AT) base pair leads to a halving of the conductance from $2.4 \times 10^{-3}\ \mathscr{G}_0$ to $1.1 \times 10^{-3}\ \mathscr{G}_0$ and the inclusion of two (AT) base pair substitutions leads to a further reduction in the conductance to $0.8 \times 10^{-3}\ \mathscr{G}_0$.

5.3.4 The effect of DNA environment on conductance

Because of the excess charges on the atoms comprising the DNA (Figure 5.8), it might be expected that the presence of water molecules would have a very profound effect on the electron energy levels and consequently on the transmission and conductance. In order to make quantitative study of the effect of water on the conductance, calculations

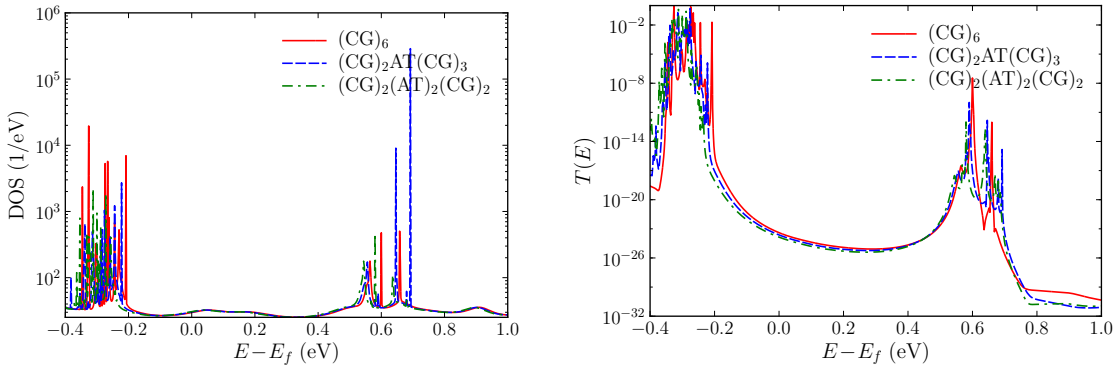

(a) **(b)**

Figure 5.10: The DOS (a) and transmission spectra (b) of a DNA molecule trapped between gold surfaces (111) showing the effect of replacing CG and CGCG sequence with an AT and ATAT respectively in a $(CG)_6$ strand. The sulfur atoms are attached to the 3' and 3' carbon atoms of the opposite backbones.

were carried out by adding water molecules in the computational cell containing a $(CG)_n$ trimer between two Au electrodes with $n = 3-6$. Figure 5.11 shows the results for $(CG)_3$ and $(CG)_4$ where 491 and 625 of water molecules were added to the cell respectively. These numbers of water molecules correspond to the density of water to being approximately one gm/cm^3 at STP.

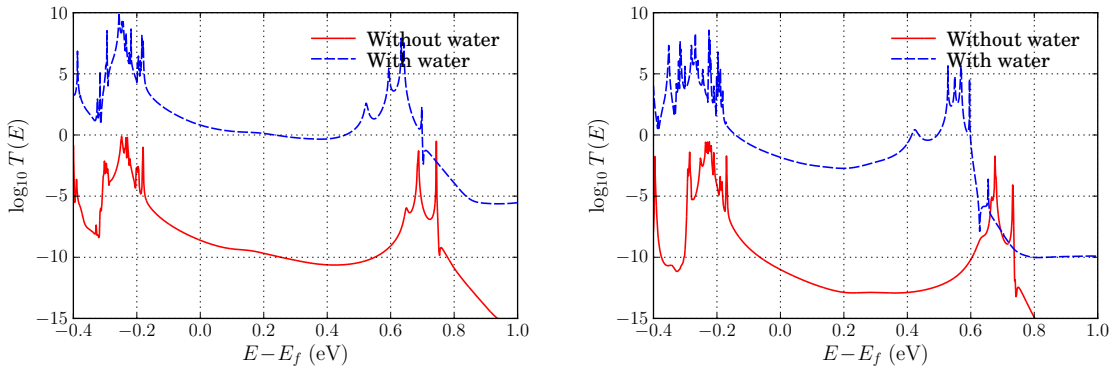

(a) **(b)**

Figure 5.11: The logarithm of transmission spectrum of a DNA molecule using (3'-4') contact geometry with (a) $(CG)_3$ and (b) $(CG)_4$ sequences. The results in presence of water compared with that with no water are represented by the dashed and solid lines, respectively. The scale on the vertical axes is for the DNA without water. The transmission curve for the DNA with water is shifted up by 10 units in order to display the changes.

The results of the calculations with water molecules were then compared with that without water molecules by analyzing the excess charge distributions across the molecule and Au electrodes and by studying the partial density of states. We found

that there is an increase in the electrode polarization which in turn affects those base pair atoms close to the contact region. The partial density of states showed that new energy states are formed in gap region which arise from both the base pair molecules and from the water molecules. The transmission function is dominated by the polarization field of water molecules affecting the electron energy levels of the base-pairs. This in turn causes a dramatic increase in the molecular conductance almost doubling it from $8.4 \times 10^{-3}\ \mathscr{G}_0$ to $0.0155\ \mathscr{G}_0$. This increase in conductivity is in general agreement with other experimental [167] and theoretical [191] findings. Although we have considered only one configuration of water molecules in this study, it is likely that the effect of water molecules would dominate the conductance. A more complete study would need to allow the water molecules to fluctuate in position but that is beyond the scope of this study.

5.3.5 The effect of the type of the leads

The Au(111) surface is often used as leads by theorists and experimentalists, but carbon nanotubes are good alternative to be used as leads [192, 193]. To investigate the effect of the leads on the DNA conductivity, we replaced the bulk gold leads by armchair carbon nanotubes. CNTs can be classified into three types depending on their energy gap [194]: metallic with zero energy gap, semi-metallic with very small gap (< 1.0 eV), and semiconductors with a moderate gap. All armchair CNTs show metallic behavior and this is the reason behind using armchair CNT (5,5) as leads in our calculations. We chose the DNA fragment $(CG)_3$ to carry on the calculations of DOS and transmission. As illustrated in Figure 5.12, the DNA fragment was connected to the capped ends of the CNT leads by using the same backbone and carbon atoms 3' and 4'.

Figure 5.13 shows a comparison between the Au(111) and CNT(5,5) leads for DOS and transmission of DNA fragment $(CG)_3$. As can be seen, the conductance of the DNA fragment reduces dramatically when the CNT(5,5) is used as leads instead of Au(111). Moreover, the DOS follows the same trend of transmission. This might be the main reason for this considerable reduction in conductivity especially that the H-L gaps in both cases are equal. In addition, the DOS for the CNTs leads is generally much less than that of Au leads. This also affects the transmission because the availability of electronic

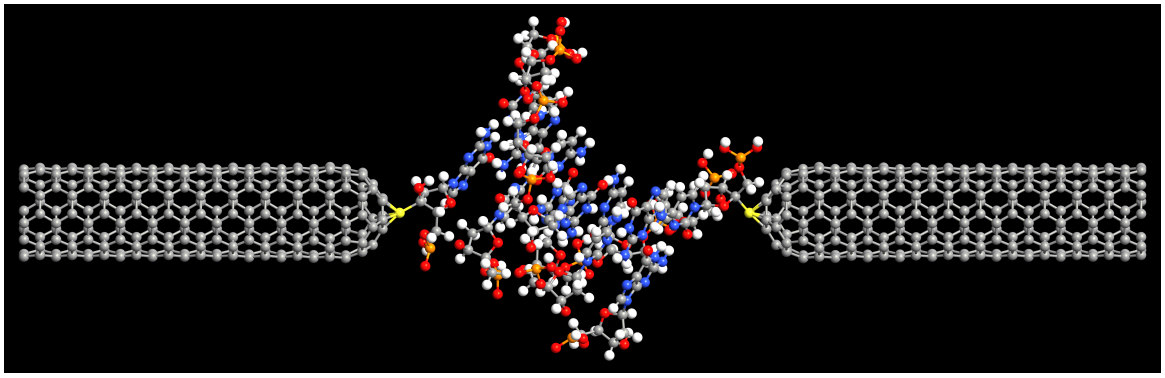

Figure 5.12: A DNA fragment of $(CG)_3$ sequence in between two leads of capped CNT (5,5). The DNA molecule is attached to leads via sulfur atoms (yellow balls).

states plays an important role in charge transfer through a molecule. Furthermore, the capped part of the CNT leads includes pentagon-heptagon pair which leads to orbitals hybridization from sp^2 to sp^3 and causes the armchair CNT to be imperfect metal. This might be also a reason for showing a low conductance. Therefore, using CNTs with open ends rather than capped ones could produce more comparable results for DNA with that of gold.

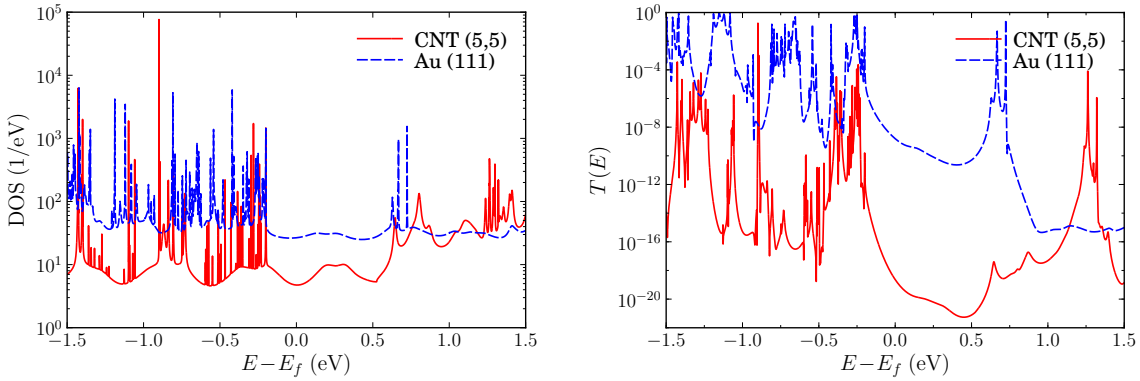

Figure 5.13: The DOS (left) and transmission spectrum (right) of DNA molecule with $(CG)_3$ sequences using two types of leads: Au (111) and armchair CNT (5,5). In both cases, the sulfur atoms are attached to (3'- 4') carbon atoms on the same backbone.

5.4 Conclusions

We used the Landauer formalism to calculate the conductance of DNA base pair polymers in different configurations and in different environments. We did not consider atomic vibrations and their contribution to the conduction through polaron effects. These are thought to be important in considering the electrical transport across

biological molecules. However, from the results of our study, we are able to demonstrate that the reduction in conductance across a base pair sequence with length can arise due to a non-uniform broadening of the density of states near the Fermi level. One of the problems we encountered in this study is in the determination of the Fermi level. Although this ought to be clearly defined in the EHT approach, as the number of atoms considered increases, there is a need to improve the energy resolution of the transmission function. This is in part responsible for the slightly ambiguous results shown in Table 5.2. The dependence of transmission on the sequence of the base pairs was found to be in general agreement with experiments for the hexamers considered. Finally, because the EHT method can be applied to systems not readily accessible to *ab initio* methods, we were able to investigate the effect of water on the conductance of these base pair polymers. The results for the conductance are also in agreement with both experimental and theoretical findings.

CHAPTER 6

GRAPHENE NANORIBBONS

6.1 Introduction

The nature of the semi-metalicity of pristine graphene with zero band gap does not allow it to be incorporated directly in the fabrication of electronic devices. Therefore, opening and tuning a small band gap in graphene is a fundamental step towards exploiting its remarkable thermal and electrical properties in future applications. The behaviour of charge carriers in 2D lattice of graphene changes dramatically when a gap is created. In the case of the zero gap, with linear energy dispersion relation around the Dirac points (K and K′) (Figure 6.1), the carriers move roughly as fast as photons because their effective mass is almost equal to zero. The onset of a gap causes charge carriers to travel slower because of the increase in their effective mass as well as their low conductivity. Over the last decade, various approaches have been proposed to accomplish this goal, such as quantum confinement [195–201], substrate interaction [202–205], chemical functionalization [206–210], doping [211–214], applying perpendicular electric field [215–218], straining the graphene layers [219–223], breaking the honeycomb lattice symmetry via introducing topological defects and grain boundaries [26, 50–68] (as presented in Chapter 7) and punching a graphene sheet with periodic holes [69–78] (as discussed in Chapter 8).

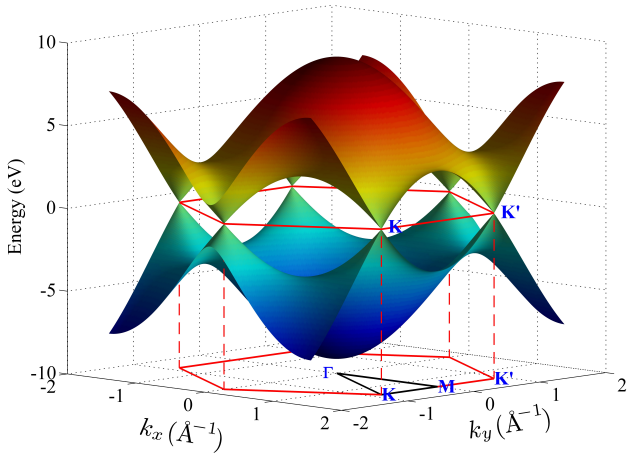

Figure 6.1: The electronic band structure of graphene as calculated using tight binding model with first neighbour interactions. Also shown are Brillouin zone (red hexagonal), reduced Brillouin zone (black triangle with vertexes Γ, K, and M). The six corners of the hexagonal Brillouin zone, where the conduction and valence bands touch each other, are known as Dirac points. Two of these six Dirac points (K and K') are inequivalent.

6.2 Band structure and DOS of pristine graphene

The most important step in performing EHT calculations is in the determination of the appropriate parameters. These parameters significantly affect the outcome of EHT calculations and play a crucial role in obtaining reliable results for the systems under study. So, the first step towards investigating graphene based materials was to reproduce the electronic band structure of 2D pristine graphene using EHT by comparing the results with that obtained by *ab initio* methods. Because of the different behaviours of carbon atoms in 2D systems from that of isolated molecules, the EHT parameters used for porphyrin and DNA are not appropriate in determining the correct band structure of graphene. Therefore, a different set of parameters are required. We have adapted the set proposed by Keilen *et al.* [143] which is tabulated in Table 3.1. For example, Keilen *et al.* used the value of 2.8 for the Wolfsberg-Helmholtz constant for both *s* and *p* orbitals. In our calculations, we have found that using the value of 2.25 for *s* orbital results in a band structure very similar to that obtained by the SIESTA code. In Figure 6.3, the results using EHTransport and SIESTA are plotted for the band structure and DOS of graphene. The agreement is very good [1].

[1] In the case of SIESTA calculation, we used the generalised gradient approximation (GGA) in flavour of the Perdew-Burke-Ernzerhof (PBE) for the exchange-correlation term. Moreover, the default built-in

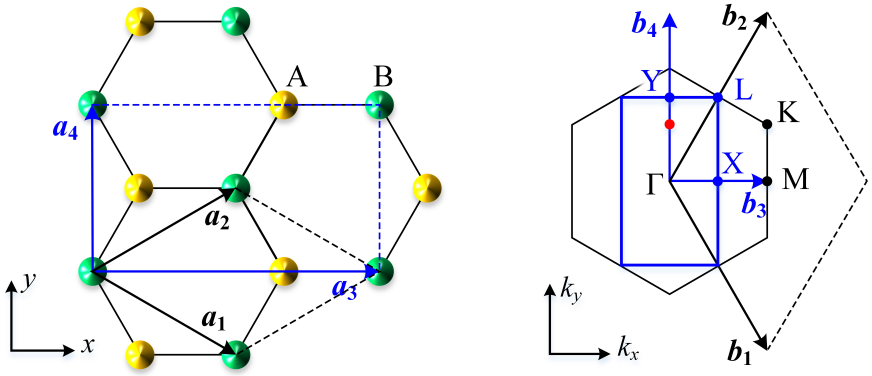

Figure 6.2: (Left) The two different unit cells used to define the honeycomb lattice of graphene. The lattice vectors $\vec{a}_1$ and $\vec{a}_2$ define a rhombic primitive unit cell with two carbon atoms, while the rectangular conventional cell contains four atoms and is defined by $\vec{a}_3$ and $\vec{a}_4$ lattice vectors. (Right) The corresponding Brillouin zones with the high symmetry points in k-space. The black hexagonal one is for the primitive cell, while the blue rectangular one corresponds to the conventional cell. The red point inside the conventional cell indicates the Dirac point.

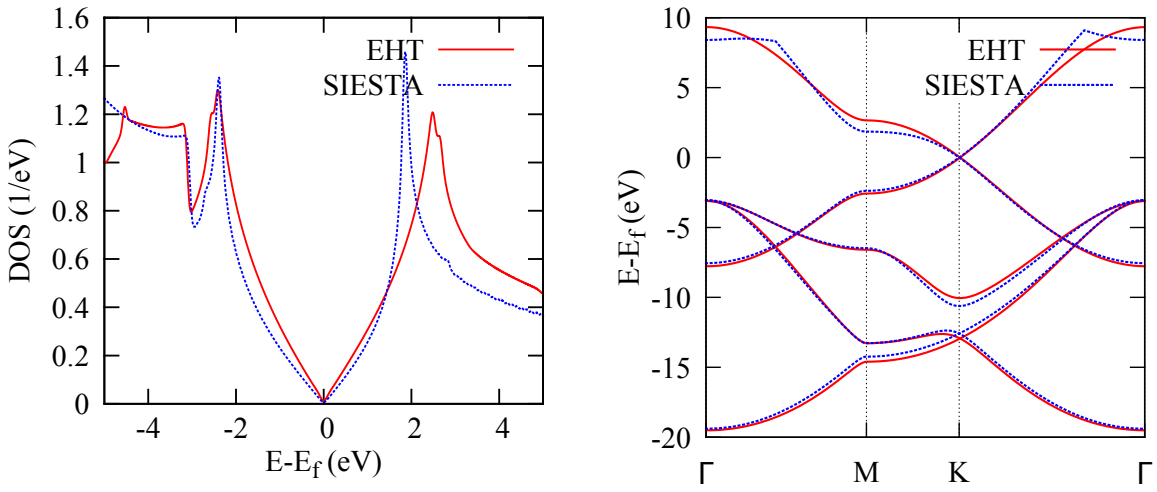

Figure 6.3: The DOS (left) and band structure (right) of pristine graphene calculated using EHTransport with the parameter set shown in Table 3.1 and SIESTA.

The band structure calculations were carried out using rhombic primitive unit cell with two carbon atoms as illustrated in Figure 6.2. The Monkhorst scheme [224] was used to sample the 2D Brillouin zone of graphene with a progressing denser grid of k-points. It was found that a minimum separation of 0.01 Å^{-1} in k-space was required to ensure convergent results for the DOS. This corresponds to a k-point grid of $300 \times 300 \times 1$. Moreover, in the case of EHTransport, the convergence of the result depends also on the

double-ζ polarized (DZP) basis set was employed to represent the valence orbitals of carbon atoms with an energy cutoff of 0.5 eV and mesh cutoff of 450 Ry. Tight tolerances of 10^{-5} and 10^{-5} eV on the density matrix error and the total energy, respectively, were used as combined criteria to achieve the convergence in the self-consistent cycle.

broadening parameter η that is employed to smooth the DOS curve shape. For instance, the DOS curve is smoother with $\eta = 0.04$ compared to $\eta = 0.02$ for the same grid of k-points as illustrated in Figure 6.4. In other words, a convergent DOS can be achieved with $150 \times 259 \times 1$ k-grid for $\eta = 0.04$, but denser grid is required for $\eta = 0.02$. In order to investigate the influence of the number of points in the energy window, the DOS over energy range (-5.0 to 5.0) eV was calculated by using 5001, 10001, and 20001 points which correspond to energy spacings of 0.002, 0.001, and 0.0005 eV, respectively. The calculations showed that no noticeable difference. Thus, an energy spacing of 0.002 eV was found to be sufficient for the DOS calculations.

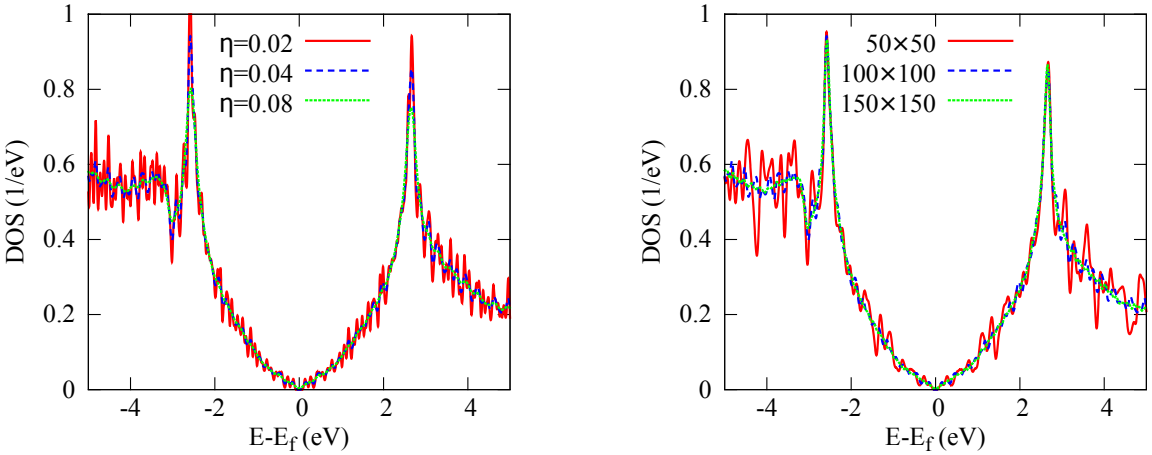

Figure 6.4: The DOS of pristine graphene calculated by EHTransport (left) with k-grid of $100 \times 100 \times 1$ and various broadening parameter η, and (right) with $\eta = 0.04$ and three different mesh of k-points.

6.3 Graphene nanoribbons (GNRs)

GNRs, which are sheets of graphene cut to make ribbons, have two basic edge shapes: zigzag and armchair. The corresponding ribbons are termed zigzag nanoribbons (ZGNRs) or armchair nanoribbons (AGNRs). These two edges have a 30° difference in their orientation within the graphene sheet. Large differences in the π-electronic structures are induced by these two types of graphene edges. In particular, a zigzag edge exhibits localized states, whereas an armchair edge does not exhibit such localized states. The appearance of graphene edge states may directly contribute to the peculiar magnetic, electronic and transport properties of nanoscale graphene as will be discussed in the following sections. The width of a graphene nanoribbon is defined by an integer

N, which represents, in the case of an armchair ribbon, the number of carbon atoms, while in the case of a zigzag ribbon, it is the number of dimer (two carbon sites) lines that are located along the cross section of the ribbon (Figure 6.5). The same number N for both types of ribbons does not mean that the ribbons have the same physical width when the same unit of length are used to measure them. Therefore, to compare the physical quantities of armchair and zigzag ribbons, it is more convenient to define the width of a ribbon in terms of the lattice constant a or C-C bond length a_{C-C} as follows [43]:

$$W_A = \frac{N-1}{2}\,a \equiv \frac{\sqrt{3}}{2}(N-1)\,a_{C-C} \qquad \text{for the AGNR,} \tag{6.1}$$

and

$$W_Z = \left(\frac{\sqrt{3}}{2}N - \frac{1}{\sqrt{3}}\right)a \equiv \left(\frac{3}{2}N - 1\right)a_{C-C} \qquad \text{for the ZGNR.} \tag{6.2}$$

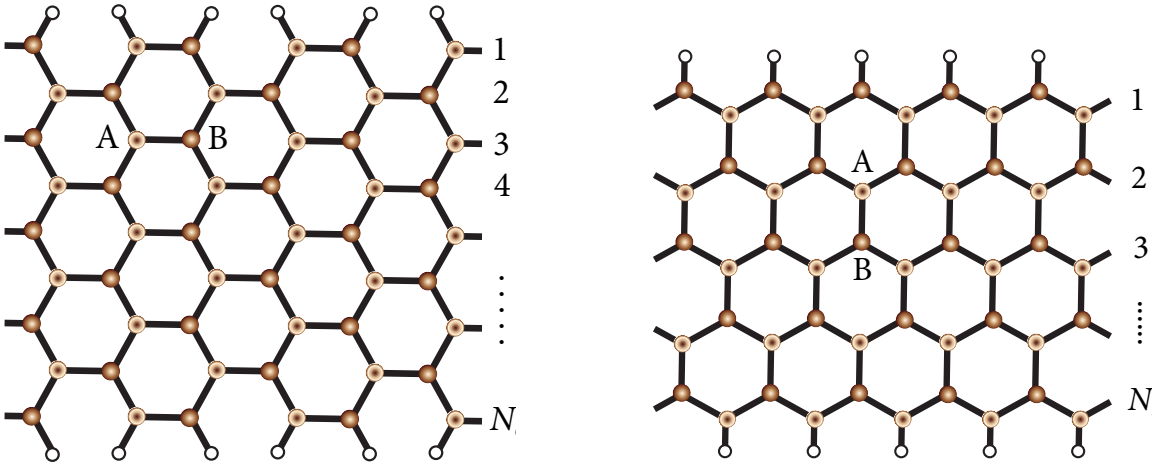

Figure 6.5: The two types of graphene nanoribbons: (left) armchair and (right) zigzag. A and B represent the two sublattice sites. Adapted from ref. [43].

Tight-binding calculations have shown [225] that the conductivity of graphene nanoribbons is highly dependent on their width and edge type. For AGNRs, when $N = 3m-1$ (with $m = 1,2,3,...$) the ribbons turn out to be metallic. For $N = 3m$ and $N = 3m+1$, they are semiconductors with their energy gaps decreasing almost exponentially as N increases and approaches zero in the limit of very large N. By contrast, all the zigzag nanoribbons are metallic. This is mainly due to the additional energy states which appear at their edges [44].

6.3.1 Electronic band structure of GNRs

Figure 6.6 shows the electronic band structure of ZGNR (N=2) and AGNR (N=3) calculated using both EHTransport and SIESTA codes. It is clear that, both codes give very comparable results. This provides us with the confidence to use EHTransport with the defined parameter set to study larger systems of GNRs. Accordingly, The EHTransport code used to calculate the electronic band structure and density of states of both nanoribbon structures with $3 \leq N \leq 30$ for AGNRs and $2 \leq N \leq 30$ for ZGNRs. Typical results for both types of GNRs are shown in Figures 6.7 and 6.8.

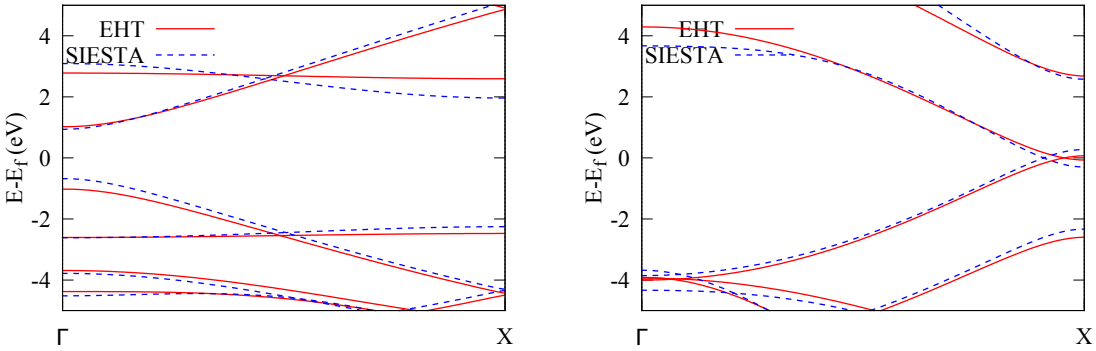

Figure 6.6: The band structure of zigzag (left) and arm chair (right) nanoribbons with width N=2 and 3, respectively. The calculations were performed using both SIESTA and EHTransport.

As already mentioned, the presence of a graphene edge has a strong impact on the electronic states of Dirac electrons. In this section, we will see that graphene exhibits a significant nanoscale edge effect by studying the electronic structures of the graphene nanoribbon using the tight binding model. It is assumed that all dangling bonds at graphene edges are terminated by hydrogen atoms and thus do not contribute to the electronic states near the Fermi level.

Figure 6.7 shows the band structure and DOS of armchair ribbons for four different ribbon widths. In all these instances, the top of the valence band and the bottom of the conduction band are located at Γ point ($ka = 0$). However, the ribbon width determines whether the system is metallic or semiconducting. From Figure 6.7 ($N = 8$ and $N = 26$), we see that the system is metallic (i.e. when $N = 3m - 1$, where $m = 1, 2, 3, ...$). For semiconducting ribbons, the direct bandgap decreases with increasing ribbon width and approaches zero in the limit of very large N.

For zigzag ribbons, however, a remarkable feature arises in the band structure, as

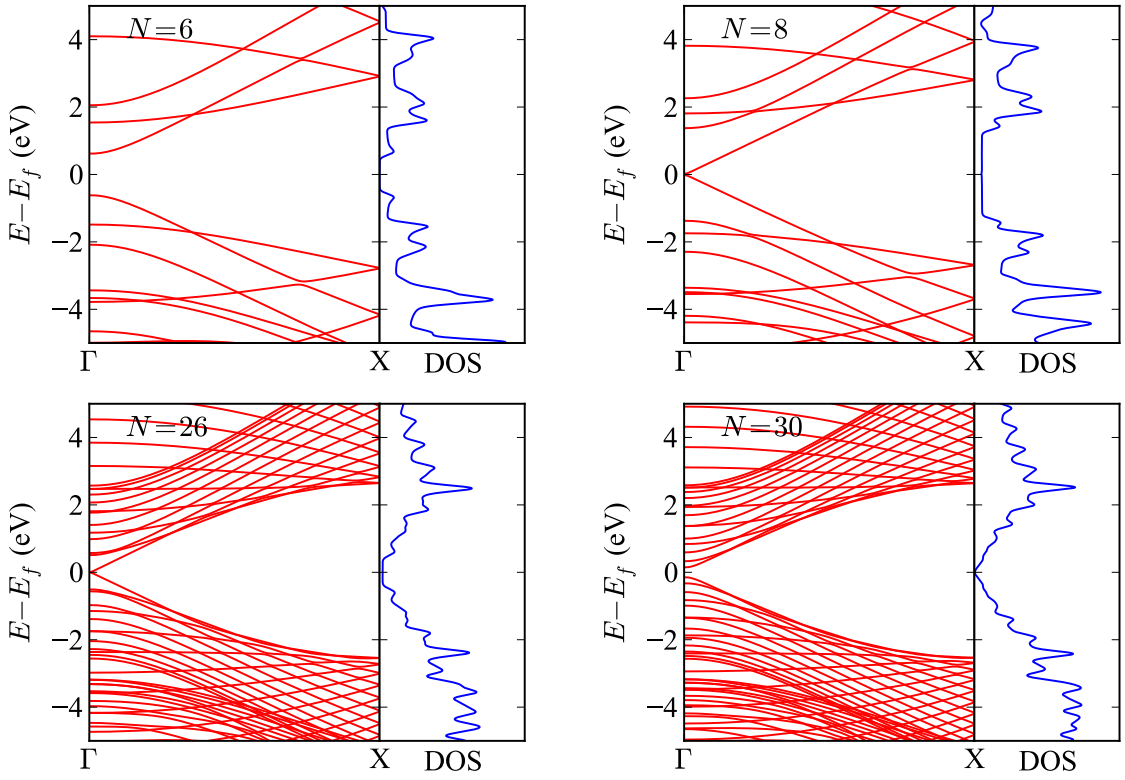

Figure 6.7: The band structure and DOS of armchair nanoribbons with various widths: $N = 6$, 8, 26, and 30 calculated using EHT.

can be seen in Figure 6.8. The top of the valence band and the bottom of the conduction band are always degenerated at the boundary of the Brillouin zone $ka = \pi$ (X point), and the degeneracy of the center bands at $ka = \pi$ does not originate from the intrinsic band structure of the graphene sheet. These two special center bands flatten with increasing ribbon width. A pair of partial flat bands appears within the region $2\pi/3 \leq |ka| \leq \pi$ (from 2/3 Γ X to X), where the bands are located in the vicinity of the Fermi level. The electronic states in the partial flat bands region of the zigzag ribbons can be understood as localized states near the zigzag edge. Examining the charge density distribution theoretically [43, 44, 79] and experimentally [226–228] has shown that these bands are completely localized at the edge site when $ka = \pi$ and starts to gradually penetrate into the inner sites when ka deviates from π, reaching an extended state at $ka = 2\pi/3$.

6.3.2 The energy bandgap

From the tight binding analysis of GNRs considering only the nearest neighbor interactions, the following formula for the energy gap that occurs at Γ in an AGNR can

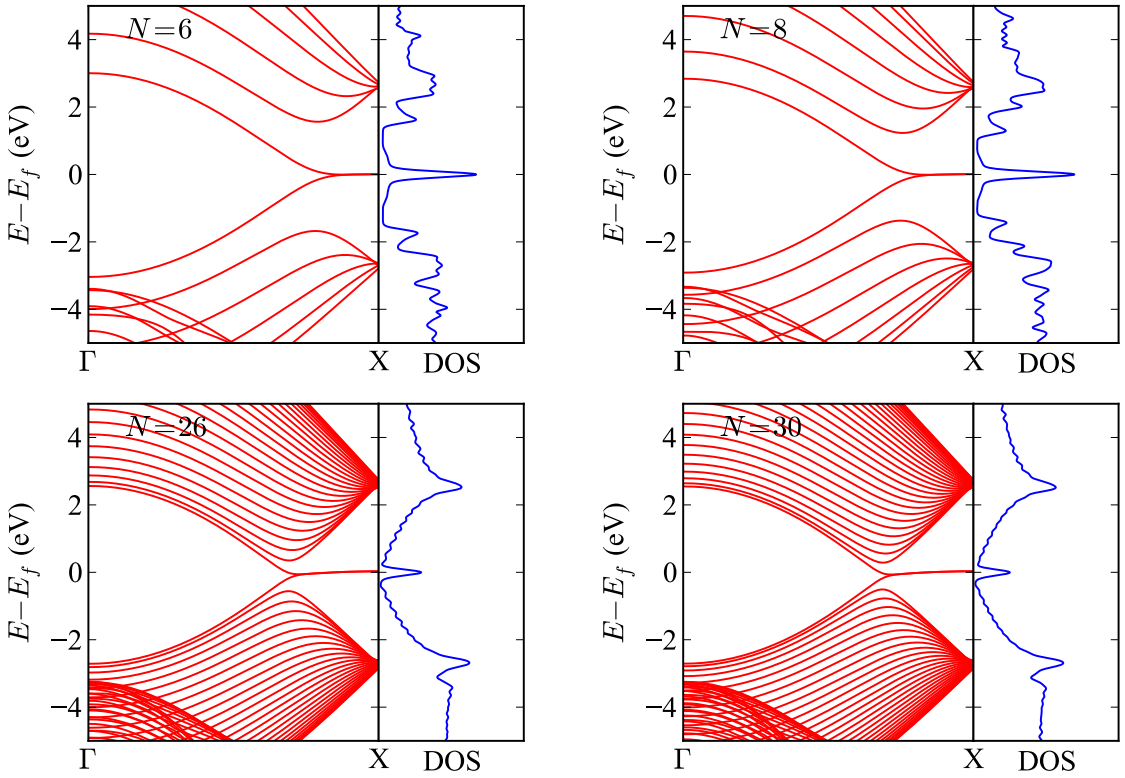

Figure 6.8: The band structure and DOS of zigzag nanoribbons with various widths: $N = 6$, 8, 26, and 30 calculated using EHT.

be obtained [45]:

$$\Delta_a = \begin{cases} 2\gamma\left[1+2\cos\left(\dfrac{2m+1}{3m+1}\pi\right)\right] & \text{if } N = 3m, \\ 0 & \text{if } N = 3m-1, \\ 2\gamma\left[1+2\cos\left(\dfrac{2m+1}{3m+2}\pi\right)\right] & \text{if } N = 3m+1. \end{cases} \tag{6.3}$$

where γ is the tight binding nearest neighbor interaction parameter and m is positive integer. By expressing N in terms of the ribbon width W_A (equation (6.3)) and performing the Taylor expansion under the condition $1/W_A \ll 1$, the leading order of Δ_a/γ for $N \neq 3m-1$ behaves as

$$\frac{\Delta_a}{\gamma} \sim \frac{\pi}{W_A/a} \tag{6.4}$$

It is clear that, the energy gap is inversely proportional to width of the graphene ribbon. This suggests that the physical quantities related to the energy gap can be scaled by the ribbon width. For the case of armchair nanoribbons with $N = 3m-1$, the energy gap closes in the tight-binding scheme. However, the incorporation of the electron-phonon

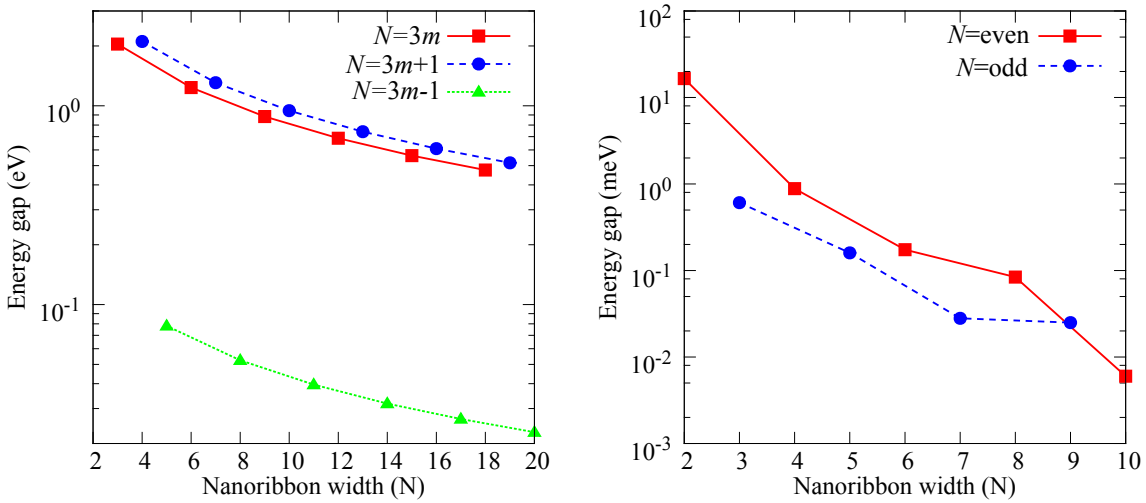

Figure 6.9: The energy band gap of armchair (left) and zigzag (right) ribbons as a function of ribbon width N calculated using EHT.

interaction results in an opening of the gap [46]. This behavior is also confirmed from the first principle DFT calculations with the local density approximation (LDA) [47]. This feature is also reproduced in the SC-EHT calculations as shown in Figure 6.9.

In the case of ZGNRs, the TB analysis gives the following expression for the energy gap which appears at $k = 2\pi/3$ [45]

$$\Delta_z = 4\gamma \cos\left(\frac{N}{2N+1}\pi\right). \tag{6.5}$$

A Taylor expansion with employing the condition $1/N \ll 1$ yields

$$\frac{\Delta_z}{\gamma} \sim \frac{\pi}{N} = \frac{\pi}{\frac{2}{\sqrt{3}}\frac{W_Z}{a} - \frac{2}{3}}. \tag{6.6}$$

Here W_Z is the ribbon width in terms of the lattice constant as defined in equation (6.2). Thus, the energy gap Δ_z is also inversely proportional to the ribbon width. Figure 6.9 shows how the energy gap varies with the width for both the armchair and the zigzag ribbons as calculated using SC-EHT.

6.3.3 Conductance of GNRs

To investigate the electrical transport properties of perfect GNRs, the transmission spectra was calculated for both types of edges with various widths. The results for

AGNR (N = 3,6) and ZGNR (N = 2,5) are depicted in Figure 6.10. As can be seen, the transmission spectra behaves as Heaviside step function for both types of GNRs showing the quantized nature of conductance. The value of transmission at a particular energy is simply the number of sub-bands available for conduction at that energy. This means that, the transmission for a GNR can be expressed by $T(E) = \mathscr{G}_0\, M(E)$, where $M(E)$ represents the number of sub-bands (number of available transport channels) with energy E. The act of the transmission reveals that the charge carriers transport ballistically without scattering across the perfect GNRs.

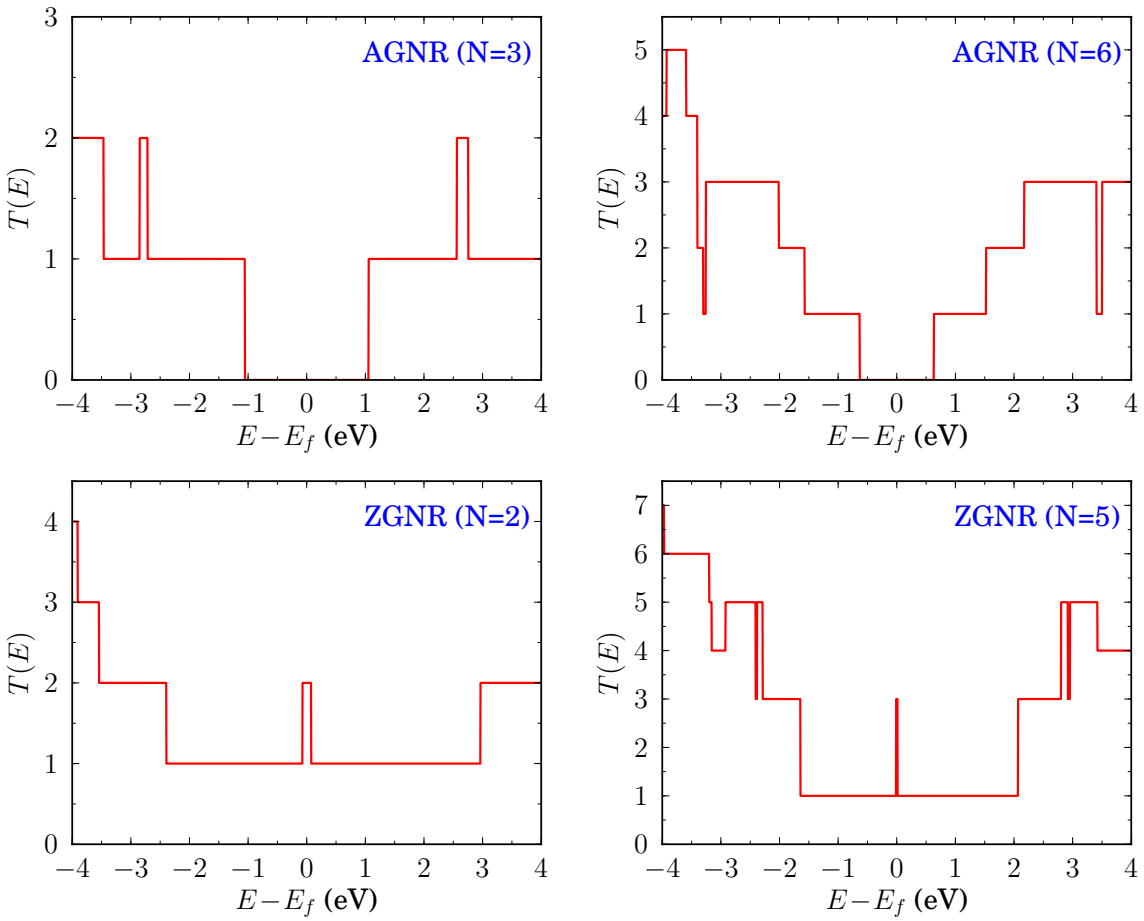

Figure 6.10: The transmission function of armchair (top) and zigzag (bottom) ribbons for different ribbon widths using EHT.

We can also see that, AGNRs show a transport gap, which is equal to that which appears in the band structure, with almost exponential dependence on the ribbon width. While ZGNRs exhibit zero transport gap with a minimum transmission value equal to $\mathscr{G}_0$ for all the ZGNRs regardless their widths. This entails that, in ZGNRs there is always at least one channel available for transport. In addition, there is an enhancement in

conductance at the Fermi level E_f which results directly from the edge states that are localised at E_f. Again, the characteristics of transmission are related directly to the electronic band structure. As an example of this relation, in the case of ZGNR ($N = 5$), the transmission at E_f is $3\mathscr{G}_0$. This indicates that three conduction channels exist at E_f. Indeed, a closer look at the band structure around the Fermi level revealed that a double crossing occurs to E_f by a sub-band.

6.3.4 GNRs with periodic nanoholes

Very recently the electronic band structure and transport properties of graphene nanoribbons with periodically hexagonal nanoholes have been investigated using DFT methods [48]. In their work, Tian *et al.* studied both types of the GNRs (armchair and zigzag) with various widths. We have carried out similar calculations using the SC-EHT code. To make a hexagonal nanohole in a ribbon, six carbon atoms (i.e. a single benzene ring) were removed and the resulted dangling bonds were passivated with hydrogen atoms. In addition, the outer edges of ribbons were also passivated by hydrogen. Figure 6.11 shows four examples of the superlattice models that we considered. The size of a supercell is determined by two factors: the width of the ribbon N and the neck width w. The neck width is defined as the minimum separation distance between opposite edges of the adjacent nanoholes. Hence, to distinguish between a perfect GNR and punched GNR, we refer to the former as A(Z)GNR (N) and the latter as A(Z)GNR (w,N) [2]. It can be seen from Figures 6.11a, 6.11c and 6.11d, a supercell has only one hexagonal hole, but the super cell shown in Figure 6.11b contains two nanoholes. The reason for that is, for the AGNR(w,N), the centers of the nanoholes do not align up in the same straight line when the neck width w is an odd number, therefore the supercell containing two nanoholes is the smallest repeatable unit.

As was mentioned earlier in this chapter, the quantum confinement can significantly modify the electronic band structure of 2D pristine graphene and introducing periodic nanoholes in GNRs strengthens this confinement. The details of the punched GNRs are controlled through various geometric parameters which include: the neck width w, the position of a hole relative to the outer edge of a ribbon, and the edge shapes of mini-

[2] Actually, the same representation used by Tian *et al.* is used here.

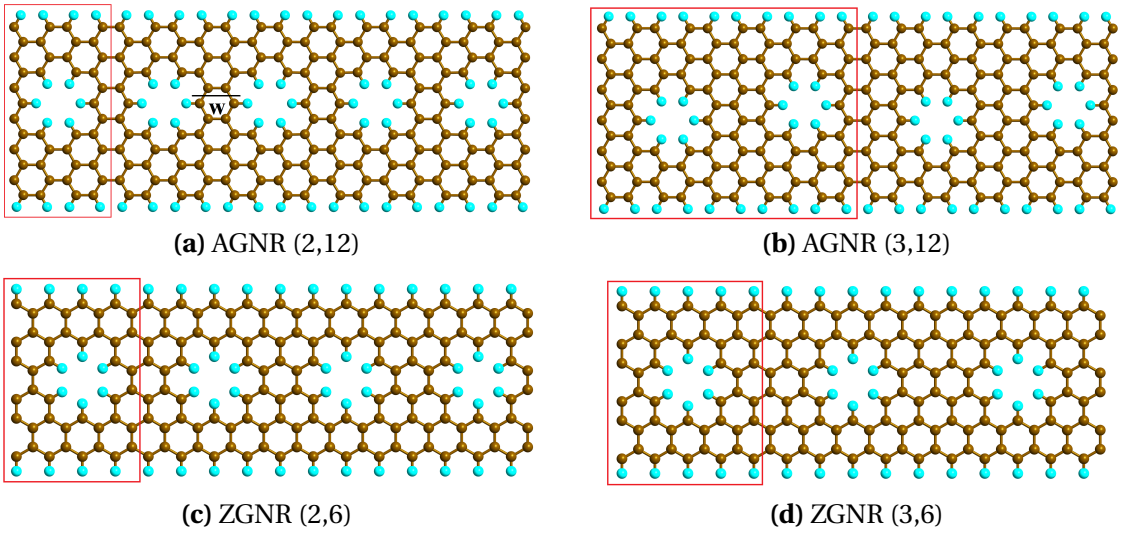

(a) AGNR (2,12) **(b)** AGNR (3,12)

(c) ZGNR (2,6) **(d)** ZGNR (3,6)

Figure 6.11: The superlattice models of GNRs with periodic nanoholes. The rectangle box indicates the supercell used in calculations.

nanoribbons along the ribbon axis and its width. The mini-ribbons in between two adjacent nanoholes and those in between edge of a hole and the outer edge of a ribbon are termed "neck-subprime nanoribbon (NSNR)" and "edge-subprime nanoribbon (ESNR)" respectively [48]. As can be seen from Figure 6.11, ESNR is orientated along the ribbon axis (i.e.) the direction of transport with the same edge shape as that for the prime ribbon. While NSNR has opposite edges shapes of that for prime ribbon and it is orientated along the ribbon width (i.e.) the perpendicular to the transport direction.

Figure 6.12 shows the electronic band structure and transmission spectra of ZGNR(w,6) with three different values of the neck width w = 2,3, and 4. The results of perfect ZGNR(6) is also plotted for comparison. It is clear that, the band structure of the punched ZGNR(w,6) is varied greatly from that of perfect ZGNR(6). However, the semi-metallicity is the common feature of both perfect and punched ZGNRs. This results from the fact that there are always sub-bands passing across the Fermi level regardless the neck width. Moreover, the region over which the bands are flattened is noticeably increasing. In other words, the edge states become more localised around the Fermi level when ZGNRs are punched with nanoholes. This is expected because punching holes increases the edge structures of a ribbon.

Regarding the transmission spectra of ZGNR(w,6), shown in the right panel of Figure 6.12, we can see that the transmission is actually nothing more than a reflection of

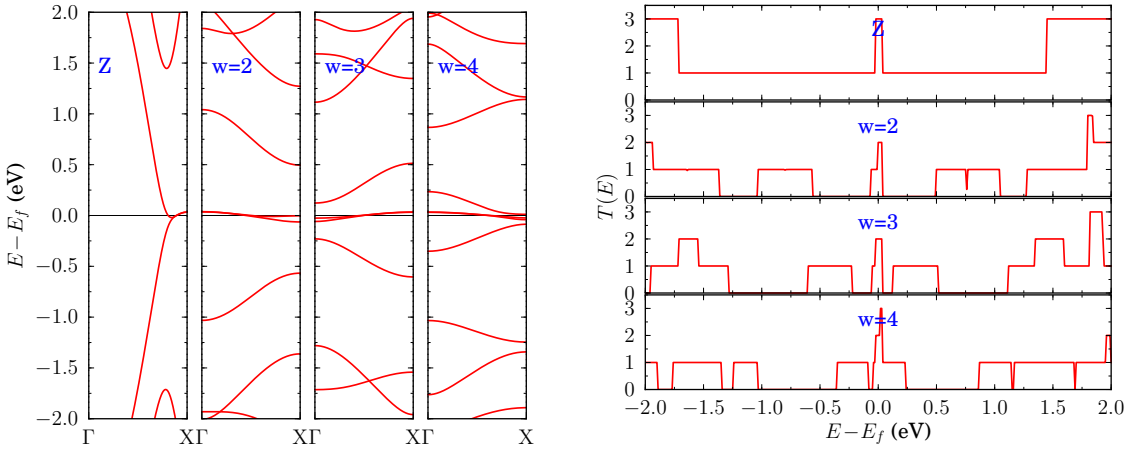

Figure 6.12: The energy band structure and transmission spectra of ZGNR(w,6) with different neck widths $w = 2$, 3, and4. The letter Z represents the case of the perfect ZGNR(6).

the electronic band structure. Moreover, the transmission coefficients of the punched ZGNR(w,6) still have high values in comparison with the perfect ZGNR(6). However, this trend of the transmission function is considerably deviated in the vicinity of the Fermi level. Hence, the presence of nanoholes in ZGNRs leads to lowering their metallicity due to the effect of quantum confinement [48].

The electronic band structure and transmission spectra were calculated for three widths of AGNRs. These include $N = 12, 14$ and 16 representing the three categories of AGNRs: $N = 3m$, $N = 3m-1$, and $N = 3m+1$ respectively. The results are depicted in Figure 6.13. Inspection of the band structure of AGNR(w,16) shows three main characteristics: firstly, the band gaps exist for the all values of neck width w. Secondly, the maximum band gap occurs at the neck width $w = 2$ which differs from that of perfect AGNR(16) by 0.36 eV. Thirdly, two different trends can be observed in the values of energy gaps of AGNR(w,16) depending on the neck width being an odd or even number. The reason for the large gaps in the punched AGNR(w,16) is ascribed to the influence of the ESNR. For AGNRs, as illustrated in Figure 6.11c, the ENSR has always armchair shaped edges which enhance the original band gap. In addition, the maximum band gap for AGNR(2,16) is due to the strongest effect of quantum confinement that occurs when $w = 2$ [48].

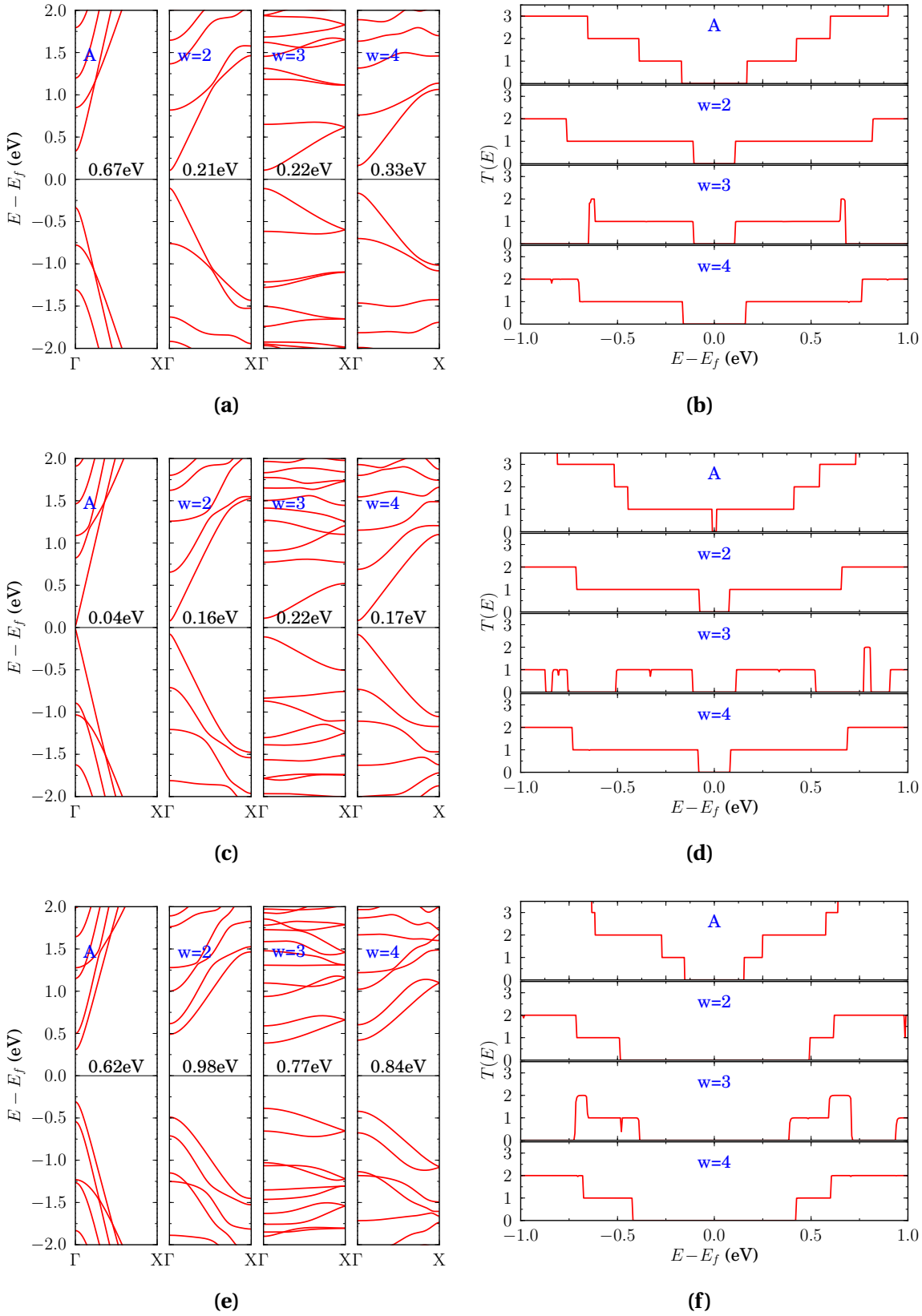

Figure 6.13: The energy band structure and transmission spectrum of AGNRs with three different widths N: (a) and (b) $N = 12$, (c) and (d) $N = 14$, and (e) and (f) $N = 16$. For each ribbon width, four graphs are plotted: (A) refers to perfect AGNR, and the other three are for different neck widths w.

The even-odd fluctuations of the band gaps with increasing the neck width can be understood by looking at Figures 6.11a and 6.11b. When the neck width w equals an even number, the centres of the neighboring nanoholes are queue up in the same straight line. However, when w takes an odd number, the centres of nanoholes are unaligned in the same straight line but with a staggered distance in the direction of the ribbon width for the two adjacent nanoholes. These geometric details considerably affect the electronic properties of AGNRs. To have deeper insights, we can think of punching nanoholes in the ribbon as introducing infinite potential wells. Certainly, the locations of these potential wells within the ribbon potential map have great impact on the determination of the electronic band structure and hence the transport features. Figure 6.13f shows the transmission spectra for the perfect AGNR(16) and the punched AGNR(w,16) (w=2, 3 and 4). The common feature to all the graphs is the absent of transport at Fermi level and in its vicinity. But the transmission function starts to behave differently over the range of energy that is away from the Fermi level.

For the ribbon width $N = 12$ which belongs to $N = 3m$ category, the band structure and transmission are plotted in Figures 6.13a and 6.13b respectively for the perfect AGNR(12) and the punched AGNR(w,12) with w=2, 3 and 4. Two distinct differences can be seen between the AGNR(w,12) and AGNR(w,16):

1. The energy gaps of the punched AGNR(w,12) are less than the gap of the perfect AGNR(12) on contrast of AGNR(w,16). This means that, increasing the quantum confinement in AGNR(w,12) leads to decrease in energy gaps. This feature shows the sensitivity of the electronic band structure of the AGNRs with periodically nanoholes for any change in geometric parameters. Tian *et al.* ascribed this oddity of AGNR(w,12) to the possible effects of the ESNR and NSNR [48]. For example, NSNR has zigzag shaped edges with metallic propreties which might modify the electronic band structure and the gap sizes of AGNR(w,12).

2. The even-odd oscillation feature is missing in AGNR(w,12) in comparison with AGNR(w,16), instead the gap increases with increasing the neck width w.

Finally, in the case of $N = 3m - 1$, the nanoribbon with width $N = 14$ was selected as a representative. The bands structure and transmission coefficient plots are shown in Figures 6.13c and 6.13d. The main characteristics are similar to that of AGNR(w,16). For

example, the energy gaps for the punched AGNR(w,14) are larger than that of the perfect AGNR(14), the even-odd oscillations of energy gaps is found again and the transmission spectra is closely related to the band structure over the whole displayed range of energy.

Our EHT results are generally in agreement with that of Tian *et al.* except the following:

- All the energy gaps in the case of AGNRs(w,N), punched with periodically hexagonal nanoholes, predicated by EHT calculations are smaller than that obtained by Tian *et al.* using DFT.

- In Tian *et al.* results, the even-odd oscillation of band gaps occurs in the AGNRs that belong to categories $N = 3m$ and $N = 3m+1$ and disappears in the case of $N = 3m-1$. While in our EHT results, this feature was observed in the case of $N = 3m-1$ and $N = 3m+1$ and was absence when $N = 3m$.

- Tian *et al.* have found that the energy gap decreases, as a general trend, with increasing the neck width w regardless the width of the AGNRs, N. On the other hand, our findings showed this trend when $N = 3m+1$, otherwise the gap increases with increasing w.

6.4 Conclusions

The EHT parameters for 2D pristine graphene were customised to produce electronic band structure similar to that of DFT approach. Following this, we have employed the SC-EHT method to examine the band structure and transmission spectra across the graphene nanoribbon structures without and with periodically hexagonal nanoholes. We have demonstrated that the results are in general agreement with those reported by other researches on similar systems using different approaches.

Inspection of the band structure of the three families $3m$, $3m-1$ and $m+1$ (Figures 6.13a, 6.13c and 6.13e) shows the following main characteristics for the AGNRs punched with hexagonal nanoholes:

1. Energy gap appears in all cases of punched AGNRs(w,N).

2. For AGNR(w,12), the energy gap decreases with increasing the neck width w. While an even-odd oscillation feature is noticed in the case of AGNRs(w,14) and AGNRs(w,16) when varying the neck width.

3. The energy gaps of punched AGNRs(w,12) are less than the energy gap of perfect AGNR(12). The opposite scenario occurs with AGNR(w,14) and AGNR(w,16) in which the gaps are greater than that of perfect nanoribbon.

CHAPTER 7

GRAIN BOUNDARIES IN GRAPHENE

7.1 Introduction

To use graphene in future microelectronic devices, it needs to be produced on an industrial scale and most importantly with large-area sheets of single crystal. The most commonly employed method to fabricate large-scale graphene is the chemical vapor deposition (CVD) method [80, 81]. In this technique, a metal foil, often copper, is used as the substrate on which the graphene is deposited. The size of the produced graphene sheet is therefore restricted only by the size of the metal foil used. The graphene samples grown by CVD are polycrystalline where multi-single crystals are stitched together to form the entire sheet. Each of these single crystals is called a domain or grain and the interface between the two adjacent grains is termed a grain boundary (GB). The GBs and other topological defects in graphene could affect its properties and may have benefits or drawbacks on employing graphene in technological applications [50, 51]. This leads us to the two long term aims in the graphene research community: developing a reliable technique to produce large-scale graphene and control on the type and number of defects. Achieving these aims opens up endless possibilities for graphene applications [229]. Graphene specimens are prepared as either monolayers deposited on a substrate of another material or free standing membranes. Generally, defects in graphene are due to imperfections and/or pre-existent defects on the substrate surface. With free standing sheets, buckling of the sheets can occur due to the elastic strains created by defects [26, 52].

In this chapter, we focus on one of these defect structures, namely the grain

boundaries that occur in large sheet of graphene in order to determine the effects of these GBs on the sheet conductance. Because of the size of these structures, it is necessary to employ a semi-empirical scheme as it would be beyond the scope of *ab initio* calculations. The EHT method was used to determine the electronic band structures of the graphene sheets with GBs. The transmission spectrum is also investigated.

7.2 The GBs structure

The atomic structure of a GB in polycrystalline graphene can be described by two translational vectors $\vec{T}_L$ and $\vec{T}_R$ of left and right domains respectively as illustrated in Figure 7.1 [53]. The two vectors $\vec{T}_i$, (where i refers to left or right domain), are defined in terms of the primitive unit vectors of graphene hexagonal lattice $\vec{a}_1$ and $\vec{a}_2$ as follows

$$\vec{T}_i = n_i\vec{a}_1 + m_i\vec{a}_2 \equiv (n_i, m_i) \tag{7.1}$$

wher n_i and m_i are integers. The crystallographic directions of the left and right domains in respect to the normal of the GB line can be described by two angles θ_L and θ_R respectively,

$$\theta_i = \tan^{-1}\left(\frac{\sqrt{3}m_i}{m_i + 2n_i}\right) \tag{7.2}$$

Hence, the misorientation angle θ between the two domains is the sum of θ_L and θ_R. For an infinite GB with periodically arranged defects, the periodic length along the GB for left and right grains are given by

$$d_i = |\vec{T}_i| = a\sqrt{n_i^2 + n_i m_i + m_i^2} \tag{7.3}$$

where $a = |\vec{a}_1| = |\vec{a}_2| = 2.46$ Å is the lattice constant of graphene. The mismatch between the left and right grain boundaries can be described by the following formula

$$\delta = \frac{|d_L - d_R|}{d_L + d_R} \tag{7.4}$$

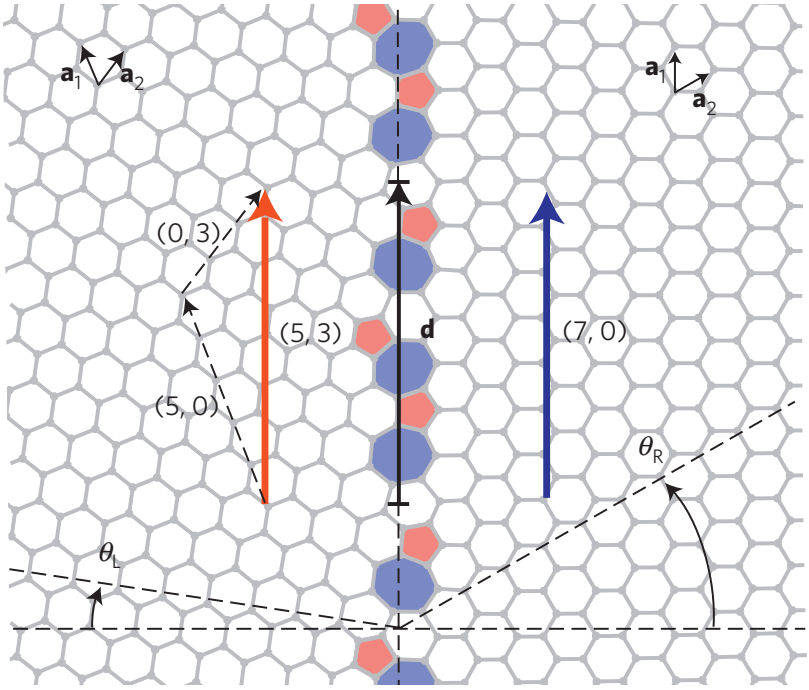

Figure 7.1: The geometry of nonsymmetric GB (5,3)|(7,0) with misorientation angle $\theta = \theta_L + \theta_R = 8.2° + 30.0° = 38.2°$. The figure shows, as well, the relationship between the primitive lattice vectors $\vec{a}_1$ and $\vec{a}_2$ and the translational vectors $\vec{T}_L$ and $\vec{T}_R$ of the left and right grains, respectively. For this special case, the two periodic lengths of left and right grains are exactly equal $|\vec{T}_L| = |\vec{T}_R| = 7.0a$. Adapted from ref. [53].

The graphene grain boundaries (GGBs) can be classified into two categories: symmetric and nonsymmetric depending on the indices pairs (n_L, m_L) and (n_R, m_R). If $n_L = n_R$ and $m_L = m_R$, the formed GB is symmetric, otherwise it is nonsymmetric. It follows that for symmetric GBs, $\theta_L = \theta_R$ and lattice mismatch δ is zero as $d_L = d_R$ (see equation (7.4)). By contrast, for nonsymmetric ones, $\theta_L \neq \theta_R$ and either $d_L = d_R$ or $d_L \neq d_R$.

To form a physically realistic GB, the periodic lengths of the left and right domains must be equal or be very close to being equal in addition to a reasonably low formation energy which is given by the formula

$$E_{form}\,(\text{eV/nm}) = \frac{E_{GB} - NE_{graphene}}{2d} \tag{7.5}$$

where E_{form} is the GB formation energy per unit length, E_{GB} is the energy of the whole GB supercell, $E_{graphene}$ is the energy per carbon atom for the pristine graphene, N is the number of carbon atoms in the supercell, d is the periodic length along the GB and finally the factor 2 accounts for the two GBs in one supercell.

7.3 Constructing a GB

Constructing the geometry of a GB model in graphene is not a trivial task especially in the case of nonsymmetric ones. The coincidence site lattice (CSL) theory [230] is commonly used to generate the geometrical structure of symmetric GBs [54, 55]. But generating nonsymmetric GBs geometries necessitates employing a more general approach which is based on carbon nanotubes theory [194]. This approach has been used to construct and study the dangling bonds of GGBs [56]. In this work, an initial structure of a GB was created using a python script. This structure was then edited for further manual configuring to be ready for a coarse geometry optimization using Avogadro software. Finally, the Long-range Carbon Bond Order Potential (LCBOPII) scheme was employed for fine optimization of the GB structure. Figures 7.2 and 7.3 show the geometries of GBs investigated in this study with periodic length $d < 2$ nm.

As illustrated in Figure 7.2, in the case of symmetric GBs, which are formed by attaching two identical grains of graphene sheets tilted at some angle, there are two different scenarios for the atoms to reconstruct. In the first one, the atoms forming the GB are distributed perfectly around the GB line as in the two isomers (3,1)|(3,1)-i1 and (4,1)|(4,1)-i1, while in the case of their counterparts (3,1)|(3,1)-i2 and (4,1)|(4,1)-i2, the GB atoms are not distributed symmetrically. To distinguish between the two cases, we refer to them by perfect symmetric and non-perfect symmetric GBs, respectively.

7.4 Computational details

Two dimensional periodic boundary conditions PBC were applied in the GB plane, i.e. in the directions perpendicular (x) and parallel (y) to the boundary. To avoid any interactions between a graphene sheet and its periodic image, a vacuum space of 40 Å was used to separate the graphene sheets along z-direction. Our calculations were carried out using a supercell containing two GBs of opposite tilt angles to implement the periodicity along graphene plane. Furthermore, a minimum separation distance was kept between the two GBs in a supercell to exclude any boundary-boundary interactions thereby giving the properties of an isolated GB. The GB-GB separation distance is equal to half the size of the supercell along the perpendicular axis to the boundary as illustrated

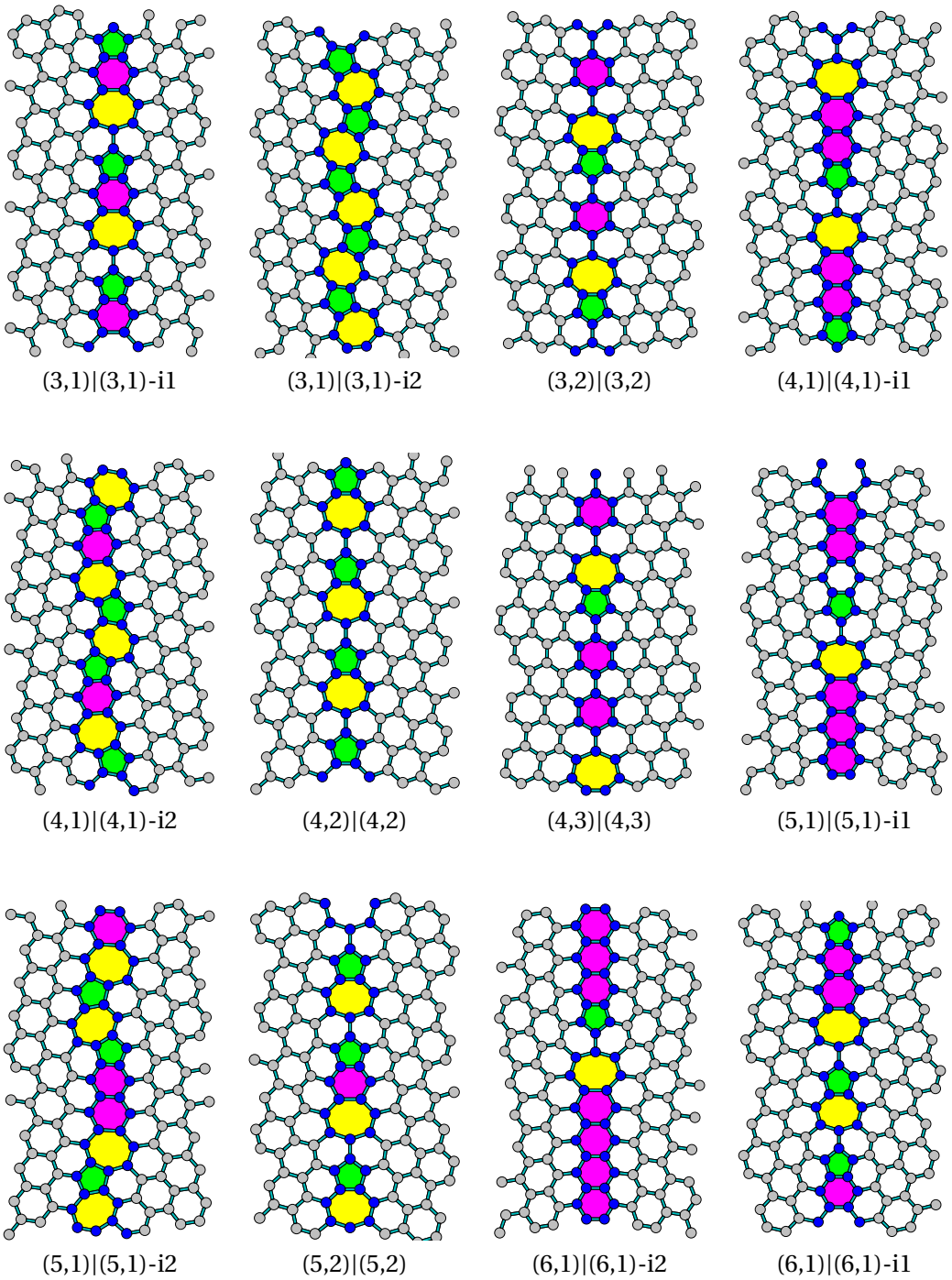

Figure 7.2: Geometries of GBs considered in this work. The Carbon atoms forming the GB are shown in blue (black) and the rings along the GB are highlighted as follows: pentagons are green (grey), hexagons are purple (dark grey) and heptagons are yellow (light grey).

in Figure 7.4. A previous DFT calculation [57] showed that a distance of 15 Å is large enough for the formation energy of the studied GBs to converge. The details of the GBs investigated here are shown in Table 7.1 where a minimum GB-GB separation of ~ 18 Å was employed in the case of the symmetric GB $(3,2)|(3,2)$.

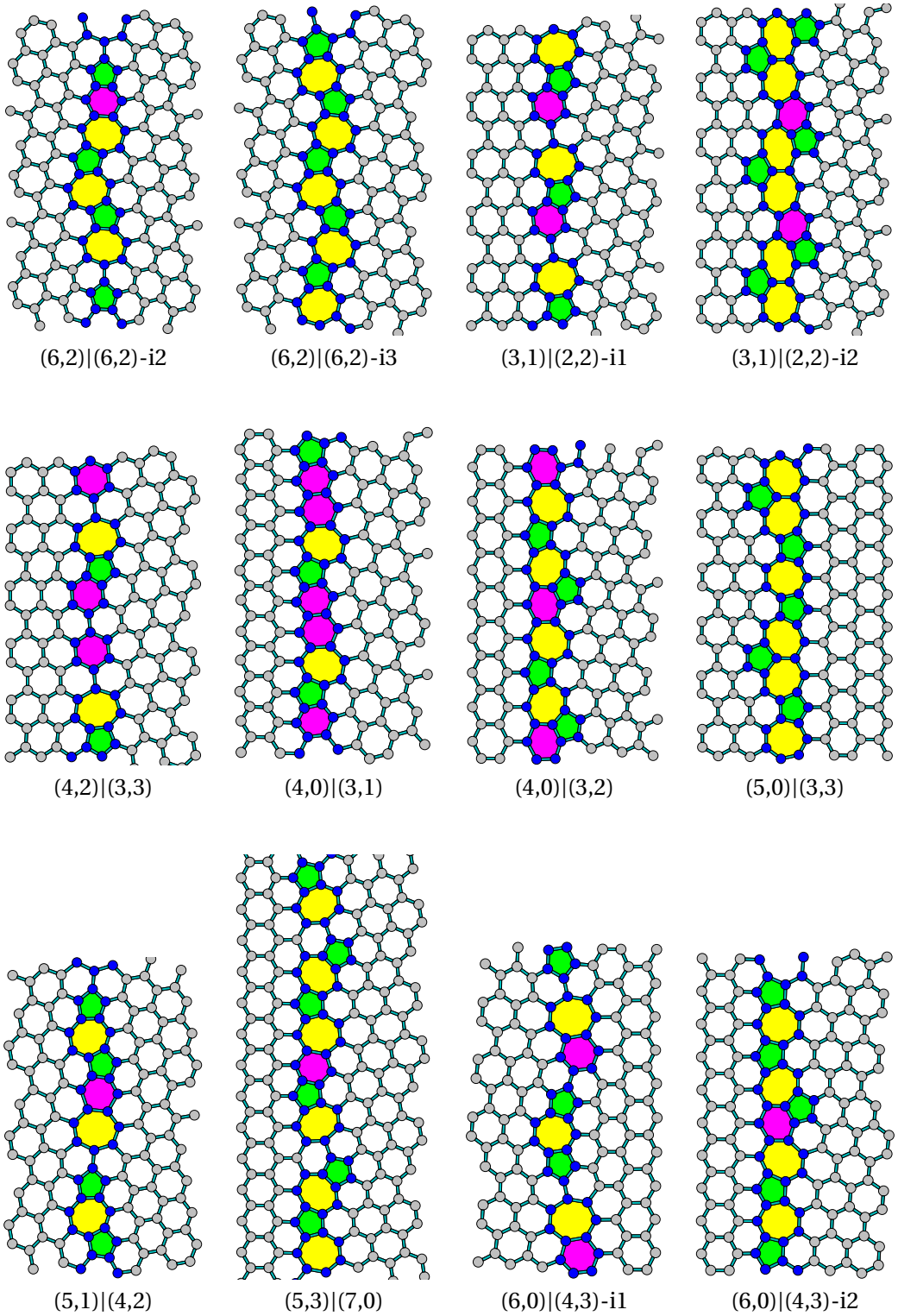

Figure 7.3: Continued of figure 7.2.

The 2D Brillouin zones of the GBs were sampled using Monkhorst scheme with equally spaced (about 0.01 $Å^{-1}$) mesh of k-points. Most of the GBs models considered in this work were adopted from ref. [58]. Based on the theory of carbon nanotubes [194],

an initial structure of a GB was created using a python script. This structure was then edited by Avogadro software for further manual configuring to be ready, in the final step, for a coarse geometry optimization using CG algorithm as implemented in Avogadro.

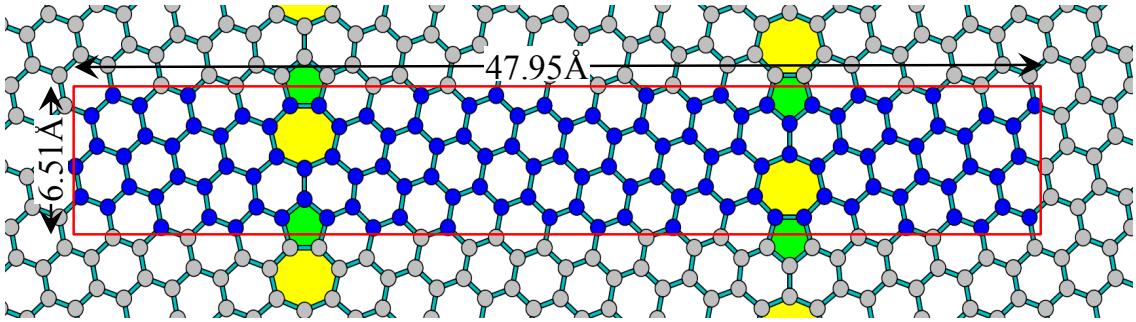

Figure 7.4: The structure of the GB $(2,1)|(2,1)$. The red rectangle shows the boundaries of supercell (which contains 120 atoms) used in the calculation.

7.5 Formation energy calculation

The formation energy calculations of the investigated GBs were carried out using the Long-range Carbon Bond Order Potential (LCBOPII) [231–233]. The potential parameters were optimized to reproduce the elastic properties of carbon in a variety of configurations. The structure relaxations with the LCBOPII were performed with a dedicated Monte Carlo code, through an annealing cycle. To do this, the initial 2D structure of a GB was heated up in steps up to 700 K and then cooled stepwise down to 10 K. Previous simulations [55] showed that the formation energies calculated (on smaller unit cells) with LCBOPII reproduce very accurately the DFT values, so that it is possible to obtain accurate formation energies for grain boundaries with significantly larger unit cells than those accessible by direct *ab initio* calculations.

After determining the periodic length of a GB (d), the total energy of the GB supercell (E_{GB}), and the energy per atom for pristine graphene ($E_{graphene} = -7.347$ eV) using LCBOPII, the formation energies were computed using equation (7.5) and tabulated in Table 7.1. As can be seen from the table, the values of the formation energies compare favourably with previous simulation results performed by DFT [58], DFTB [59], and MD using Tersoff-Brenner potential [60]. In addition, the experimentally measured value of periodic length (0.67 nm) of the (2,1)|(2,1) GB [61] is well reproduced (0.651 nm) by

our calculations. This indicates that the approach employed in this work is reliable in describing GB properties.

The values of formation energies of the considered GBs in this work range from 2.24 to 8.42 eV/nm which are noticeably less than the formation energy of bare edges in graphene (~ 10 eV/nm) [234]. Energetically, this suggests that these GBs have a high chance to exist in realistic polycrystalline graphene. For instance, a GB with misorientation angle 5.5° has been observed experimentally [62] but not studied theoretically as yet. Among the various possible combinations of left and right graphene grains to form a GB with this angle, we chose the $(17,2)|(18,0)$ for detailed investigation. It was found that, this small angle GB has a low formation energy of just 3.36 eV/nm with periodic length of 4.41 nm. The formation energy of a GB is an essential indicator for probability of its formation in real samples of graphene. However, it is not the only factor, as GBs are not equilibrium structures when they synthesised experimentally [63].

Figure 7.5 shows the plotting of formation energies of GBs vary with misorientation angle θ, periodic length d, and mismatch δ, respectively.

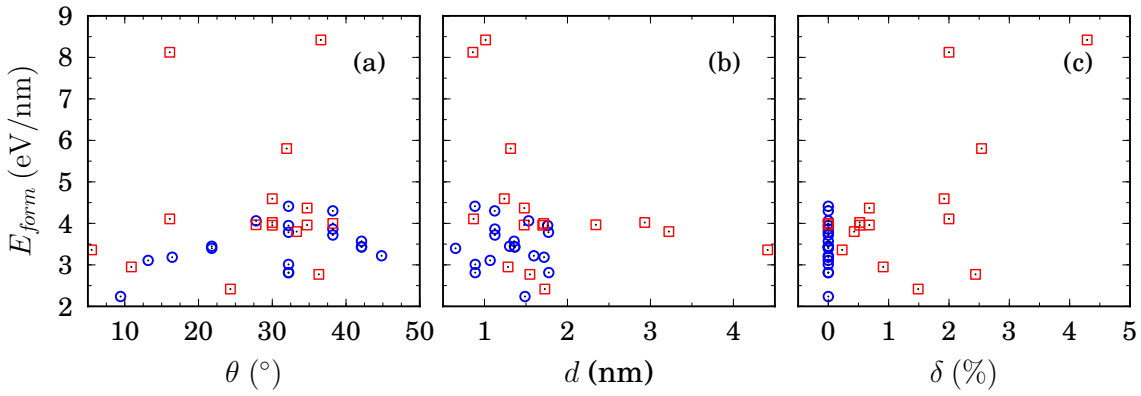

Figure 7.5: The formation energy (E_{form}) vs misorientation angle θ, periodic length d, and mismatch δ of graphene GBs. The blue circles and red squares stand for the symmetric and nonsymmetric GBs, respectively.

7.6 Electronic DOS

The existence of defects in a graphene sheet breaks the translation symmetry of the honeycomb lattice which in turns leads to creating some extra electronic states at the Fermi level and in its vicinity [61, 64, 65]. Mesaros *et al.* [66], have shown theoretically

Table 7.1: The misorientation angle (θ), the mismatch (δ), and the length of the GB supercell (L). The formation energy (E_{form}) per unit length of the relaxed periodic length (d) of the GB as calculated in this work compared with that calculated by previous studies ($E_{form}^{pre.}$). The most previous data have been taken from ref. [58], otherwise the reference is stated. To distinguish different isomers of the same GB, we used the suffixes i1, i2, etc. following the notation used in ref. [58].

GB	θ (°)	δ (%)	L (nm)	d (nm)	E_{form} (eV/nm)	$E_{form}^{pre.}$ (eV/nm)
(2,1)|(2,1)	21.79	—	4.795	0.651	3.389	3.44[58], 3.30[57], 4.00[59], 4.30[60], 3.38[53]
(3,1)|(3,1)-i1	32.20	—	3.954	0.885	4.412	5.03
(3,1)|(3,1)-i2	32.20	—	4.715	0.888	2.813	2.91[58], 3.00[54], 4.34[59], 3.80[60]
(3,2)|(3,2)	13.17	—	3.332	1.068	3.107	3.51[58], 4.20[57] 3.13[59], 4.79[60]
(4,1)|(4,1)-i1	38.21	—	5.332	1.123	4.301	4.62
(4,1)|(4,1)-i2	38.21	—	4.428	1.125	3.862	3.99
(4,3)|(4,3)	9.43	—	4.628	1.488	2.237	2.85[58], 4.0[57]
(5,1)|(5,1)-i1	42.10	—	3.876	1.364	3.435	4.26
(5,1)|(5,1)-i2	42.10	—	6.115	1.365	3.430	4.27
(6,1)|(6,1)-i1	44.82	—	4.675	1.595	3.219	4.81
(6,2)|(6,2)-i1	32.20	—	4.248	1.761	3.948	4.83
(6,2)|(6,2)-i2	32.20	—	5.723	1.771	3.785	3.23
(6,2)|(6,2)-i3	32.20	—	5.786	1.775	2.814	4.19
(3,1)|(2,2)-i1	16.10	2.00	4.470	0.868	4.108	3.82
(3,1)|(2,2)-i2	16.10	2.00	7.197	0.860	8.123	8.23
(4,0)|(3,2)	36.59	4.29	7.363	1.013	8.421	5.91
(4,2)|(3,3)	10.89	0.91	3.974	1.284	2.950	3.23
(5,0)|(3,3)	30.00	1.92	5.574	1.239	4.594	5.03
(5,1)|(4,2)	31.95	2.54	7.925	1.315	5.803	6.05
(5,2)|(6,1)	36.31	2.44	5.181	1.547	2.771	—
(5,3)|(7,0)	38.20	0.00	5.458	1.713	3.999	4.57
(5,3)|(6,2)-i1	24.32	1.49	6.738	1.727	2.417	3.19
(6,0)|(4,3)-i1	34.70	0.68	5.266	1.480	4.369	5.75
(6,0)|(4,3)-i2	34.70	0.68	5.605	1.478	3.960	4.72
(7,0)|(4,4)	30.00	0.52	7.167	1.702	3.955	—
(9,1)|(6,5)	27.80	0.00	8.073	2.342	3.966	—
(12,0)|(7,7)	30.00	0.52	6.835	2.931	4.021	—
(12,2)|(10,5)	33.30	0.43	6.220	3.222	3.802	—
(17,2)|(18,0)	5.50	0.23	7.931	4.413	3.361	—

that the GBs in graphene can enhance the local density of states (LDOS) both near E_f as well as away from E_f. The results of our calculations are illustrated in Figure 7.6. We see that DOS for some of GBs show enhancements in the LDOS, at E_f and away from E_f when compared with that of perfect graphene. For instance, the symmetric GB $(2,1)|(2,1)$ shows enhancements in the DOS especially at the energies (1.12 and 1.25 eV) under and above Fermi level respectively. This feature for the GBs is in agreement with previous theoretical study [66] and DFT simulation results [58]. This enhancement in DOS is essentially owing to the rehybridization of σ and π-orbitals in the vicinity of the GB as well as due to the effect of changing in the C-C bond lengths between the carbon atoms that form the GB (Figure 7.7) [51]. The existence of energy levels at Fermi level and/or in its vicinity is crucial for the electric current to flow through the GB, however, it is not the only factor as we will see in section 7.8.

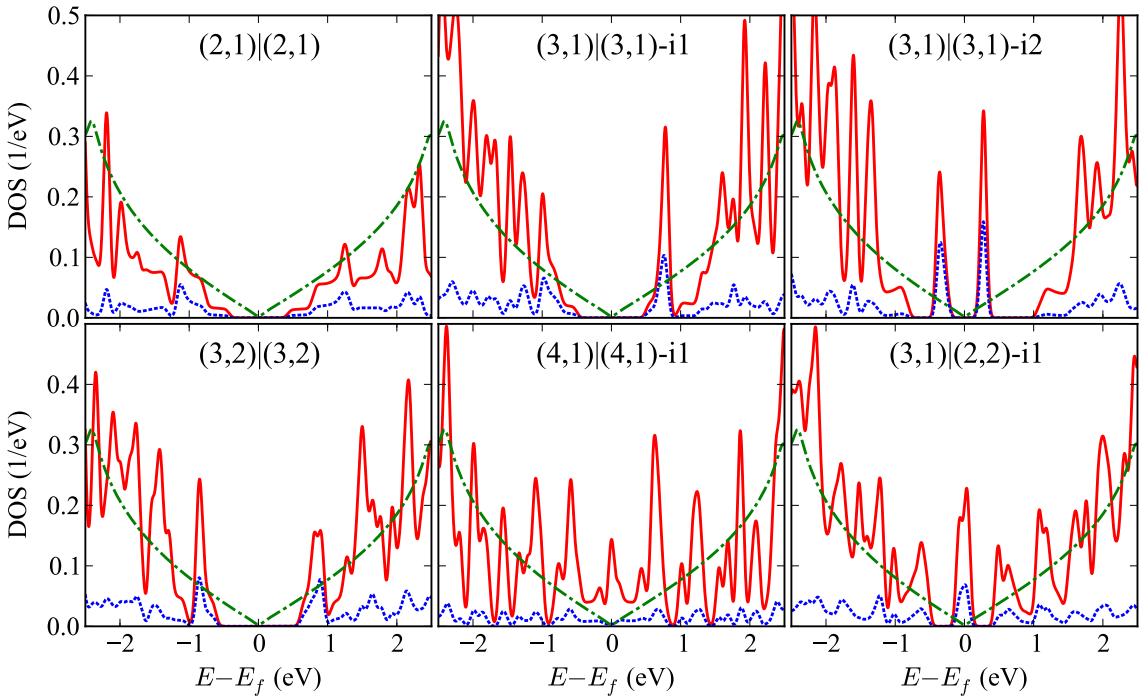

Figure 7.6: The total DOS (red solid line) of various GBs and and partial DOS (blue dotted line) of the atoms forming them in comparison of that of perfect graphene (green dashed line).

7.7 Band structure

Figure 6.2 shows the honeycomb lattice of graphene and the corresponding Brillouin zone with the high symmetry points in k-space. The $\Gamma-Y$ direction is along the GB,

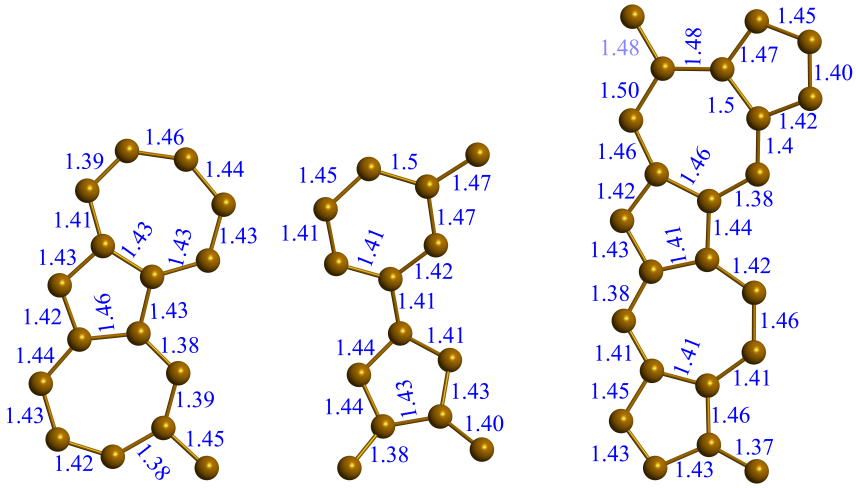

Figure 7.7: The bonds lengths (in Å) between the carbon atoms that form the GBs (left to right) (3,1)|(3,1)-i2, (3,1)|(2,2)-i1, and (5,0)|(3,3).

and the Γ−X is perpendicular to it. The Γ−X and Γ−Y directions in the GB reciprocal supercell converge to the Γ−K and Γ−M directions in the pristine graphene Brillouin zone respectively as the misorientation angle approaches zero ($\theta \rightarrow 0$). A previous DFT calculation [57] has shown that the electronic structure of polycrystalline graphene evolves to that of pristine graphene of single crystal when the misorientation angle approaches zero. In addition, the Dirac K point locates under the Fermi level and goes up with decreasing the misorientation angle. Tuning the band structure of polycrystalline graphene by applying an external strain has been explored theoretically by Wu *et. al.* [67]. They have found that, applying external strain has no effect on the electronic structure of symmetric GBs which still exhibits zero band gap. On the other hand, a band gap, up to 0.19 eV in the case of GB (5,5)|(3,7), can be opened in some nonsymmetric GBs by applying external stains. For the intrinsic strain, which is caused by the mismatch between the two grains of nonsymmetric GB, it slightly affects the band gap of the polycrystalline graphene.

Figure 7.8 shows the bands structure of various GBs. We classified them into two main categories depending on the similarity with the band structure of perfect graphene. The first group of GBs, as depicted in panels (a-e), has very similar bands of that of perfect graphene and preserves its semimetallic nature, while the second group of GBs, panels (f-j), shows considerably changes in their band structure in comparison with perfect one. From Figure 7.2, we can realize that the common feature between the first

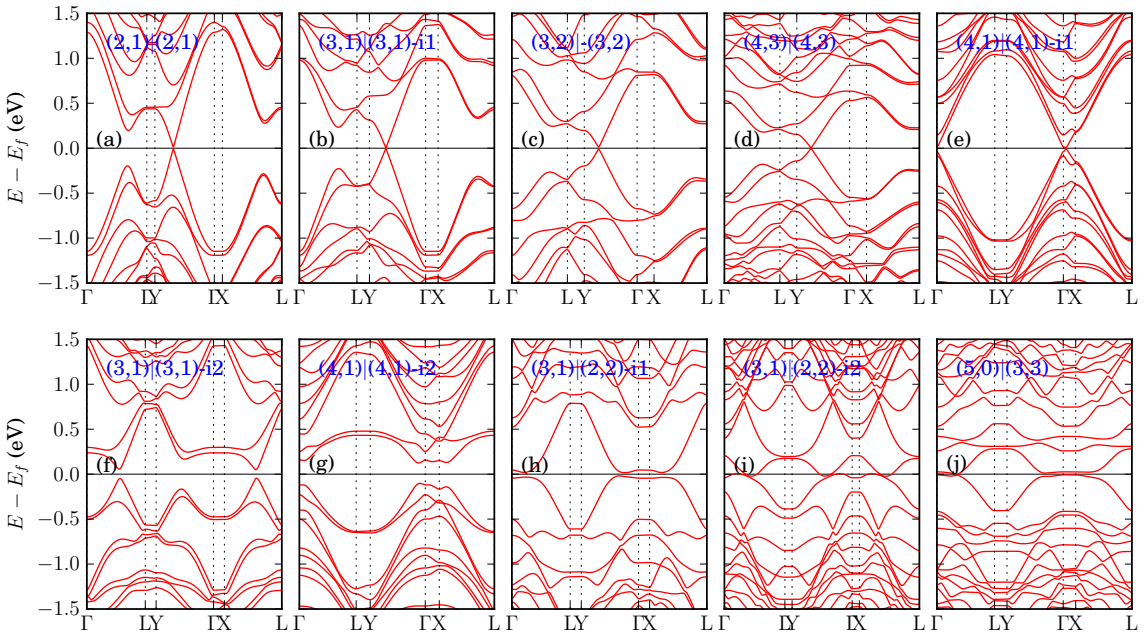

Figure 7.8: The band structure of various GBs. The top row shows the GBs that preserve the semimetallic nature of pristine graphene while the GBs whose band structures exhibit modifications are shown in the bottom row.

group members is that they are perfect symmetric GBs with two absolutely identical left and right grains. This matching between the left and right grains is mainly the reason for the GBs to inherit their band structure from perfect graphene. However, the Dirac points occur at two different points in k-space: either at $k = (0, 1/3)$ along $\Gamma - Y$ direction as in (a-d) or at $k = (1/3, 0)$ along $\Gamma - X$ as in (e). This behaviour results from the different sizes of GBs supercells and consequently the different folding into the conventional rectangular unit cell of perfect graphene. In the other group of GBs whose band structure differs considerably from that of perfect graphene (f-j), only the GB (3,1)|(2,2) shows metallic characteristics where the conduction and valence bands are interfaced, otherwise, a small band gap is opened in most cases. Zhang and Zhao have found, depending on DFT calculation, that a DOS band gap can be opened by 0.2 eV and 0.15 eV in (4,1)|(4,1)-i1 and (4,1)|(4,1)-i2 GBs, respectively [58]. By contrast, our EHT calculations revealed that the (4,1)|(4,1)-i1 GB has zero gap while the (4,1)|(4,1)-i2 GB has a gap of 0.3 eV which is comparable with the findings of Zhang and Zhao. This can be explained by the fact that measuring the gap depending on the DOS data is not accurate enough as the numerical computing of DOS depends on several parameters which must be chosen carefully. Zhang and Zhao ascribed the opening of a small gap to the deviations in bond

lengths and bond angles in the GB rings from those in the perfect graphene lattice [58]. Moreover, the local rehybridization of carbon atoms orbitals, that form the GB, from sp^2 to sp^3 may play a role in opening the gap. Indeed, checking the bond lengths for three GBs, as illustrated in Figure 7.7, confirms this trend.

It is also worth noting that, applying PBCs along the perpendicular direction to the GB line may result in some interaction between the two GBs with a supercell. This finite size effect can be responsible for opening a small gap. To investigate the effect of GB-GB interfacing, we increased the supercell size along the x-axis for different GBs and no difference was noticed in the formation energy and band gaps. For instance, we extended the width of (2,1)|(2,1) GB from 25.92 Å to 71.05 Å with 64 and 176 atoms, respectively, with not recognizing of the difference in band structure around the Fermi level. Moreover, the formation energy convergent to 3.39 eV at a separating distance of about 15 Å between the two GBs. These findings are in agreement with other previous calculation performed using DFT [57, 68].

7.8 Transport properties

The misorientation between the left and right domains of a GB, makes their Brillouin zones to be rotated by the same amount. This effective rotation in Brillouin zone is experienced by the charge carriers when they try to cross the GB line. For a carrier to transit through the GB elastically without scattering, both energy and the momentum component, $k_{||}$, parallel to the GB line must be conserved. By folding the momentum space from 2D Brillouin zone of graphene into that of 1D of grain boundary, we can demonstrate how the corresponding momentums in the two Brillouin zones are related to each other. Depending on the geometry of left and right domains, there are two possibilities for the Dirac points K and K$'$ to be mapped onto the 1D Brillouin zone of the GB. If $n-m=3p$ with ($p=0,1,2...$), the Dirac points are mapped onto the Γ point, otherwise, they are folded separately onto $k_{||}=-2\pi/(3d)$ and $k_{||}=2\pi/(3d)$ and hence the distance to the Γ point is $k_{||}=2\pi/(3d)$. Based on this basic idea, Yazyev and Louie concluded that most of the GBs are transparent and the charge carriers can transmit perfectly through them [53]. Although a GB with $n_L-m_L=3p$ and $n_R-m_R\neq 3p$ (or

$n_L - m_L \neq 3p$ and $n_R - m_R = 3p$) would show a transport gap given by

$$E_{TG}\,(\text{eV}) = \hbar v_F \frac{2\pi}{3d} \approx \frac{1.38}{d\,(\text{nm})} \tag{7.6}$$

where v_F is the Fermi velocity ($\sim 10^6$ m/s). The transport gaps tabulated in Table 7.2 are generally comparable with that predicted by YL's model and that from previous DFT studies [68]. This confirms that crossing the GB by charge carriers is determined completely by the GB periodicity and its orientation with respect to the crystalline lattices of the two grains of polycrystalline graphene. However, the slight difference of 0.05 eV between the values of the transport gaps of the $(3,1)|(2,2)$ GB isomers suggest that the topological details of the GB rings do have some effect also on the transport gap. It is worth noting that (as shown in 7.9), the transmission curve shows symmetric behaviour (similar to that of perfect graphene) around Fermi level for the GBs $(2,1)|(2,1)$ and $(3,1)|(3,1)$-i1. In these two GBs, the defect rings are distributed symmetrically along the GB line and their structures are closer to that of perfect graphene. Moreover, disruption of the graphene lattice perfection leads to a reduction in the transmission coefficient for both types of GBs that exhibit zero and some transport gap. However this reduction is less for the former which is expected as the deviation from the perfect graphene is less. Despite the fact that, the availability of the electronic states in vicinity of Fermi level is essential for any conduction process to occur, however, it is not enough. This can be seen from inspection the transmission graphs depicted in Figure 7.9. For instance in the case of the GB (5,0)|(3,3), although electronic states exist at Fermi level (Figure 7.6), however, the transmission and consequently conductance exhibits a gap of 1.28 eV around Fermi level. This behavior can be completely understood in the frame of the momentum conservation model proposed by Yazyev and Louie.

Table 7.2: The periodic length d in (nm) and the theoretical transport gap (E_{TG}) computed using equation (7.6) compared with that calculated using DFT (E_{TG}^{dft}) and calculated in this work (E_{TG}^{eht}). All the energies are in (eV).

$(n_L, m_L)\|(n_R, m_R)$	d	E_{TG}^{eht}	E_{TG}^{dft} [68]	E_{TG}
$(3,1)\|(2,2)$-i1	0.868	1.36	1.45	1.59
$(3,1)\|(2,2)$-i2	0.860	1.31	1.54	1.60
$(2,0)\|(1,1)$	0.435	2.61	—	3.17
$(5,0)\|(3,3)$	1.239	1.28	1.03	1.11
$(7,0)\|(4,4)$	1.723	0.72	—	0.80

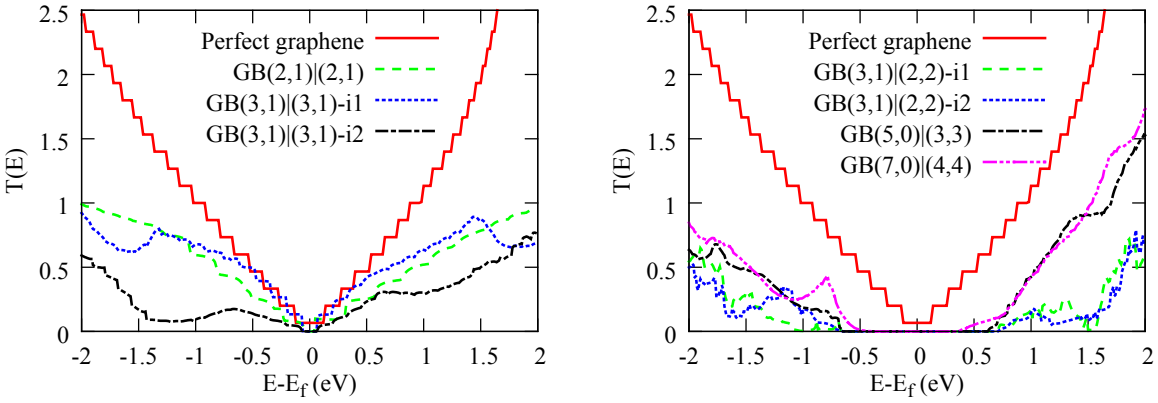

Figure 7.9: The transmission spectrum of perfect graphene and various GBs that show zero (left) and a finite transport gap (right).

7.9 Conclusions

The EHT method together with NEGFs formalism was used to study the electronic and transport properties of grain boundaries in polycrystalline graphene. Additionally, we employed the LCBOPII potential, as implemented by Fasolino and Los [231–233], to calculate the formation energies of the GBs. Our results are in agreement with other previous DFT simulations, theoretical models, and experimental observations. Most GBs preserve the semi-metallicity of perfect graphene, however, a few (which have specific geometrical structure of left and right domains) show a gap in transport spectrum around the Fermi level that depends mainly upon the periodic length of the GB. These features can be used for controlling and tuning the electrical properties of polycrystalline graphene.

Experiments have shown that, multiple domains of single crystals can coexist in synthesised graphene sheets of large area. Studying and understanding the properties of such systems theoretically is very important especially if the aim is to incorporate them in future microelectronics. It should also be possible to dope the grain boundaries with acceptor and donor atoms such as boron and nitrogen [235], respectively, which would result in semiconductors of p and n-type. These are areas for future research, both theoretically and experimentally. Topological defects in graphene grown on a substrate are caused by the imperfections and pre-existent defects on the substrate surface. By controlling these imperfections with desirable patterns, it should be possible to design precisely the form of the GBs together with its specified electrical properties.

CHAPTER 8

GRAPHENE NANOMESHES (GNMS)

8.1 Introduction

Recently, tremendous efforts have been made to construct a graphene sheet with periodically nanoscale holes punched in it, known as graphene nanomeshes (GNMs) or graphene antidots. This is because making a nanohole in a graphene sheet leads to quantum confinement of electrons movement through the 2D lattice and distorts the linear dispersion relation $\varepsilon(\vec{k})$ of pristine graphene near the Dirac points. As a consequence, a band gap may open up. The size of which can be controlled by adjusting various parameters of the GNM lattice. The hole shape, hole size, lattice geometry, and the periodicity of the holes along x- and y-axis are parameters that all play a crucial role in determining the size of the band gap, which, for technological applications, should be at least of the order of tenths of an electron-volt [77]. Moreover, n-type and p-type semiconductors could be obtained by doping the punched graphene sheet with donor and acceptor impurities such as nitrogen and boron. These ambitious future perspectives are motivated by some successful experimental fabrications of single layer of graphene into which an array of nanoholes are punched [70, 71]. Bai *et al.* [70] have showed that GNM-based FETs had on/off ratios similar to those of GNR devices and more importantly, the GNM devices can carry currents much greater than that of a single GNR. GNMs have been explored via many theoretical models to predict any potential change in their electronic structures due to lattice modification by perforating [69, 72–78]. As in all graphene based materials, the electronic structure of a GNM is essentially determined by the π electrons. Therefore, the main electronic features of the GNMs can

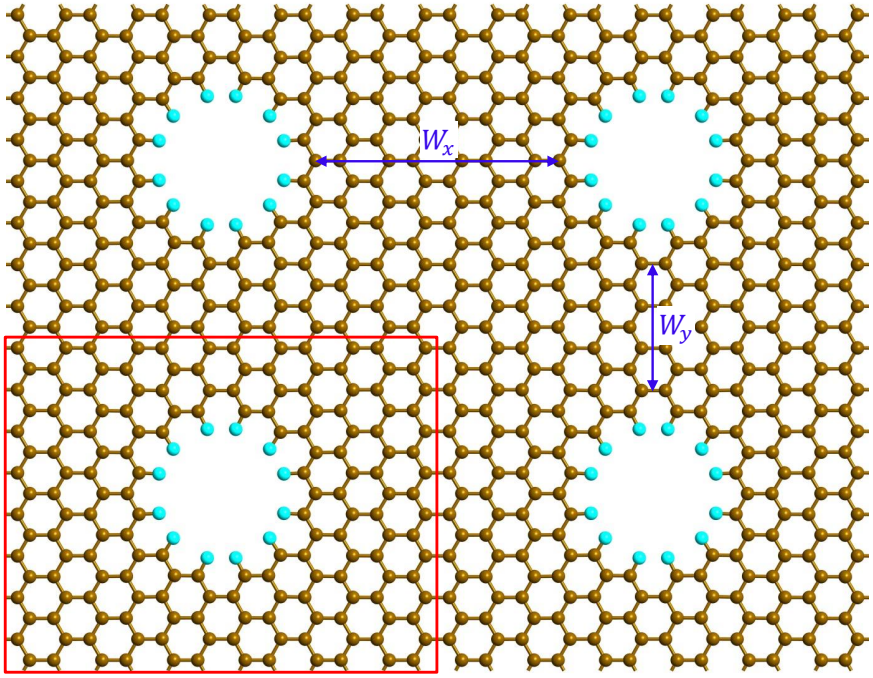

Figure 8.1: A 2×2 super lattice of the (6×8)h2 GNM. The cyan (gray) and brown (black) spheres represent hydrogen and carbon atoms respectively. The unit cell (determined by a rectangular solid line) has been replicated twice along x and y axis, W_x and W_y are the neck widths along x and y-axis respectively.

be discovered using a simple tight binding model considering only the nearest neighbor interaction. For instance, Pedersen *et al.* [69] found a scaling rule for the energy gap of a GNM with respect to the numbers of carbon atoms removed and the original carbon atoms in a unit cell. However, first principles DFT calculations have revealed more detailed information in the electronic structures of GNMs. DFT computations carried by Ouyang *et al.* [72] have predicted that half of GNMs were semimetals and the rest were semiconductors, while Şahin and Ciraci [73] pointed out that only one-third of their calculated GNMs had significant nonzero band gaps.

As shown in Figure 8.1, the holes periodicity W_x along x and W_y along y-axis represent the shortest distance between two neighboring holes along corresponding direction. This distance is termed as neck width and play an important role in determining the electronic properties of GNMs. To classify the different unit cells of GNMs, we followed the same approach as suggested in ref. [74]. As illustrated in Figure 8.2, the unit cells of GNMs are classified by pair of integer numbers (P and Q) which represent the number of the repeating conventional rectangular cells for the pristine graphene along the x (armchair) and y (zigzag) directions, respectively. Thus, we refer to

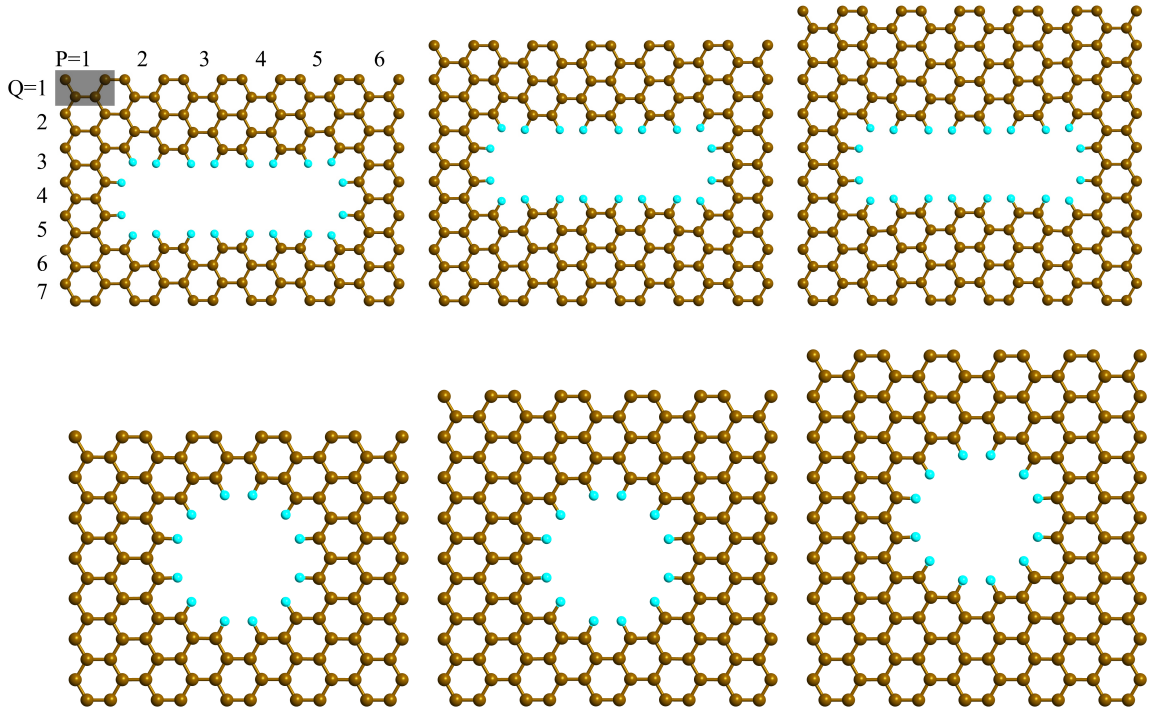

Figure 8.2: (Top row) three different unit cells of GNMs with rectangular nanohole. All the units have the same periodicity along x axis with $P = 6$ while the lattice parameter Q along the y axis has the values 7, 8, and 9 (from left to right), respectively. The rectangular hole for all the cases has dimensions of 5.05 × 16.02 Å with 40 removed carbon atoms. The shaded rectangular area represents the conventional unit cell of pristine graphene. (Bottom raw) three different unit cells of GNMs with hexagonal nanohole. The periodicity along x axis is 5 while the lattice parameter Q along the y axis has the values 7, 8, and 9 (from left to right), respectively. The hexagonal hole for all the cases has a diameter of 7.72 Å with 24 removed carbon atoms.

a GNM with lattice parameters P and Q as ($P \times Q$) GNM; for example, those in top panel of Figure 8.2 are named as (6×7), (6×8), and (6×9) GNM, respectively. Then, we add the information of the hole using either (r) or (h) letter, to denote a rectangular or hexagonal hole, followed by an integer indicating the size of the hole (Figure 8.3). For instance, the GNMs shown in Figure 8.2 are described as follows: (6×7)r1, (6×8)r1, (6×9)r1, (5×7)h2, (5×8)h2, and (5×9)h3 from top to bottom and left to right.

The electron energy calculations were performed using a 9 × 9 × 1 mesh of k-points in the BZ as this was found to be sufficient to obtain convergent results for the large unit cells of the investigated GNMs. To prevent any interaction between a GNM sheet and its periodic image, a vacuum spacing of 40 Å was used along the perpendicular to the GNMs plane (z-axis).

The systems studied in this work were taken to have rectangular unit cells, as shown in Figure 8.2, with two different hole shapes and different sizes: rectangular

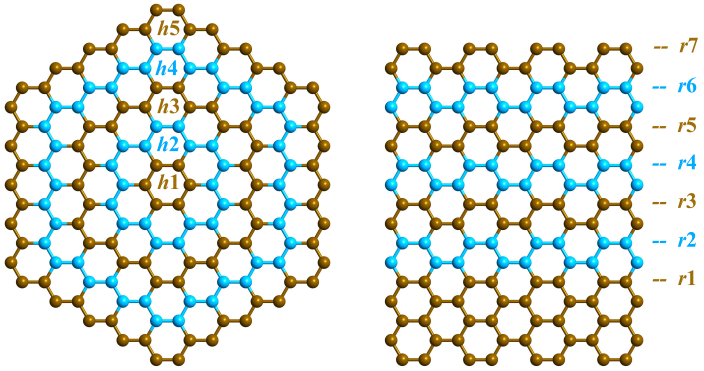

Figure 8.3: The hexagonal and rectangular nanoholes that used to punch the graphene sheet. Two different colors are used here to easily distinguish between different sizes of the holes.

and hexagonal holes. The dangling carbon bonds at the hole edges were passivated by hydrogen atoms. The lattice parameters P and Q range from 6 to 12 for both hole shapes. This corresponds to GNM unit cells dimensions along x and y-axis range from (25.26 to 51.15 Å) and (14.77 to 29.53 Å) respectively. With regard to the hole size, for hexagonal holes, the diameter was varied between 3.34 and 24.32 Å while for rectangular hole the dimensions were varied between (15.98 × 4.73 Å) and (15.98 × 17.35 Å). These different holes are shown in Figure 8.3.

8.2 Electronic band structure of GNMs

Figure 8.4 shows the electronic band structures of three different GNMs with hexagonal holes. It is noticeable that the conduction and valence bands are nearly symmetrical around the Fermi level. This feature may be ascribed to the behavior of π electrons in graphene. The energy dispersion of pristine graphene, based on the tight binding formalism, reveal clearly this fact where the occupied and unoccupied bands are symmetrical (Figure 6.1). The electronic band structures of the explored GNMs can be classified into two main categories: semimetals with zero (or roughly zero) band gap and semiconductors with a direct gap at the Γ point. In the case of the first category, the valence and conduction bands touch each other at two different k-points depending on the lattice parameters P and Q of the associated GNM. For example, in case of the (6×7) GNM, the matching occurs at a point along the k path (Y → Γ), while the bands meet exactly at the Y point for the (6×8) GNM. Other GNMs considered have band structures similar to one of these three, depending on their lattice parameters P and Q. It follows

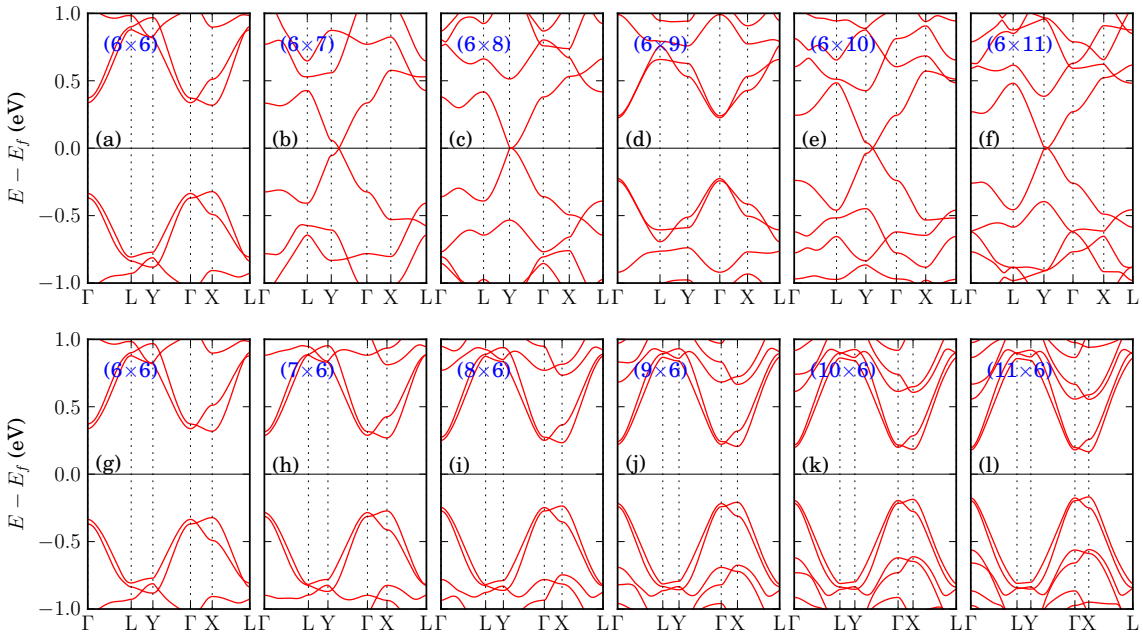

Figure 8.4: Electronic band structures of GNMs with the hexagonal hole h2 of 24 removed C atoms and different lattice parameters P and Q. The top graphs are for $P = 6$ and $Q = 6, 7, ..., 11$ and bottom are for $Q = 6$ and $P = 6, 7, ..., 11$.

that a third of the GNMs show semiconducting behavior and two thirds preserve the original semimetallic nature of pristine graphene.

The set of graphs in the top row of Figure 8.4 show that changing the lattice parameter Q, whilst keeping P constant, results in opened or closed gaps in h-GNMs. For $Q = 3m+1$ or $3m+2$ (where $m = 1, 2, ...$), the h-GNMs have zero (or nearly zero) gap with similar band structures. However, if $Q = 3m$, the h-GNMs exhibit a band gap of between 0.18 and 0.64 eV (Table 8.1). This shows semiconducting behavior. Again, the band structures of these structures are similar. By contrast, keeping Q fixed and varying P results in the energy gap reducing progressively with increasing lattice parameter P. The essential features of the band structure are similar for these configurations.

A different scenario is observed in the case of a graphene sheets perforated with periodic rectangular holes. As can be seen in Figure 8.5, the band structures were computed for various GNMs using rectangular hole h2 with 40 C atoms removed. As in hexagonal hole instances, the investigated r-GNMs can be classified into three categories depending on the value of Q: $3m$, $3m+1$, and $3m+2$. The first two groups of r-GNMs are semiconductors with a direct band gap at Γ and Y points respectively, while the semimetallic nature of graphene with zero-gap is perpetuated in the case of $Q = 3m+2$.

Table 8.1: The energy band gap (E_g) in eV for various GNMs with two different nanoholes: hexagonal (h2) and rectangular (r1) hole with 24 and 40 carbon atoms removed, respectively.

P \ Q	Hexagonal hole			Rectangular hole				
	6	9	12	6	7	9	10	12
5	0.788	0.522	0.385					
6	0.641	0.451	0.337	0.783	0.522	0.508	0.337	0.377
7	0.542	0.393	0.296	0.632	0.345	0.424	0.240	0.318
8	0.469	0.346	0.263	0.533	0.215	0.366	0.159	0.277
9	0.414	0.310	0.236	0.462	0.123	0.322	0.095	0.246
10	0.370	0.279	0.214	0.407	0.051	0.288	0.045	0.221
11	0.335	0.255	0.195	0.364	0.010	0.261	0.006	0.200
12	0.306	0.233	0.179	0.329	0.003	0.238	0.002	0.184

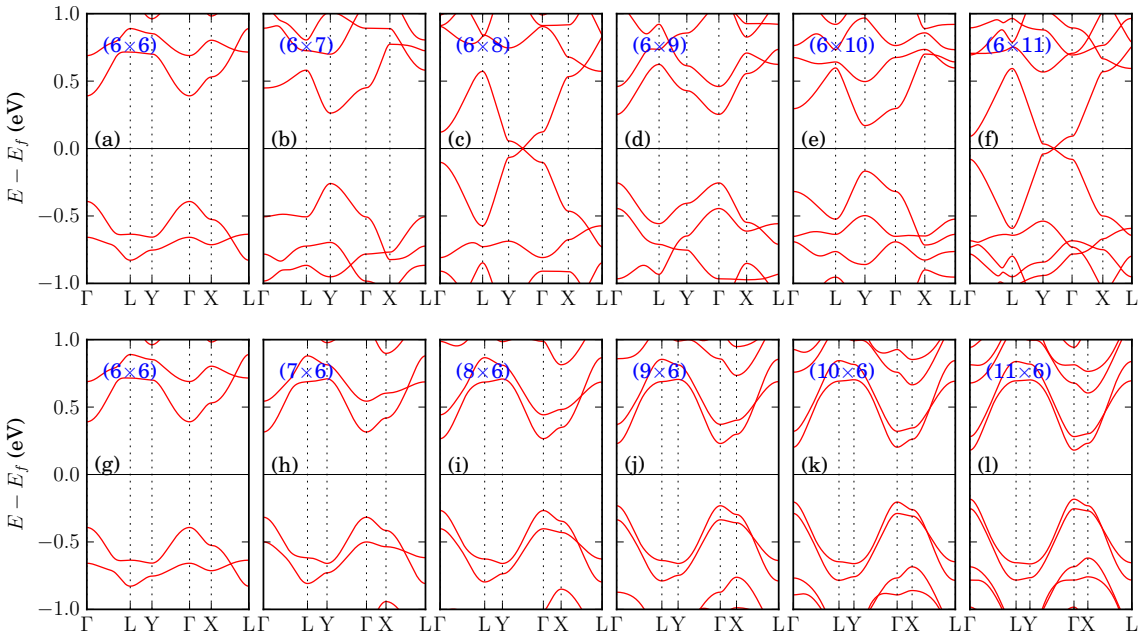

Figure 8.5: Electronic band structures of GNMs with a rectangular hole and different lattice parameters P and Q. The top graphs are for $P = 6$ and $Q = 6, 7, ..., 11$ and bottom are for $Q = 6$ and $P = 6, 7, ..., 11$.

Hence, the distinctive difference between GNMs with hexagonal and rectangular hole is that, in former case, only one third of investigated samples have a gap while, in the latter, a gap can be opened in two thirds of GNMs samples.

Pedersen *et al.* [69] carried out band structure calculations using a tight binding model and found that the energy gap of a GNM scaled according to the formula

$$E_g = \omega \frac{N_r^{1/2}}{N_t}, \tag{8.1}$$

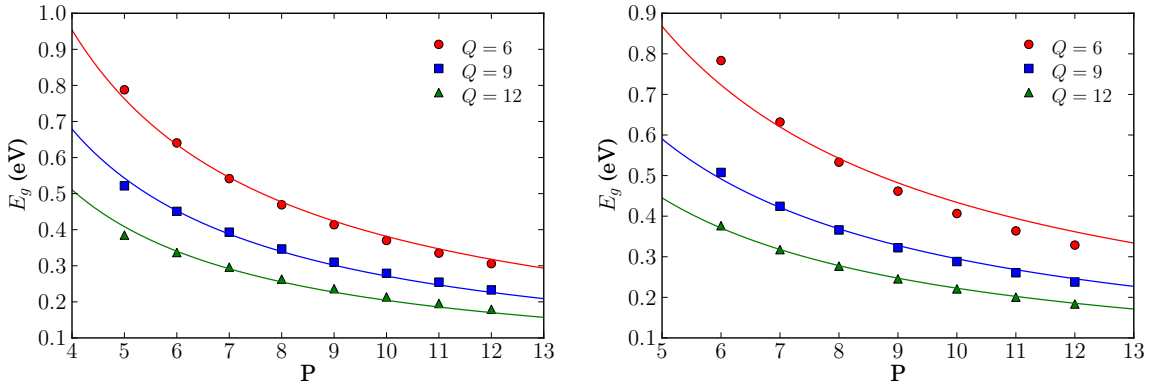

Figure 8.6: The energy band gap (E_g) of GNMs as a function of lattice parameter P for various values of Q, where (left) is for hexagonal hole of 24 removed carbon atoms and (right) is for rectangular hole of 40 removed carbon atoms. The data are fitted to equation (8.1).

where N_t is the total number of carbon atoms in a unit cell before making a hole, N_r is the number of carbon atoms removed when a hole is punctured and ω is a constant whose value is determined numerically by fitting the calculated energy gaps to equation (8.1). For a rectangular unit cell, $N_t = 4PQ$, and for a particular value of the lattice parameter Q and fixed hole (N_r = constant), the energy gap is inversely proportional to P (*i.e.* $E_g \propto 1/P$). Figure 8.6 shows the energy gap E_g as a function P and Q for hexagonal and rectangular holes. The calculated values of E_g are in agreement with that determined by the Pedersen *et al.* formula viz. that $E_g \propto 1/P$ for fixed Q. The fitted value of ω for each case is tabulated in the bottom row of Table 8.2.

In case of hexagonal nanohole, the fitted values of ω for $Q = 6, 9$, and 12 are about 19, 20, and 20 eV, respectively, in comparison with $\omega = 25$ eV fitted by Pedersen et al. for their TB results. Moreover, the result of Oswald and Wu revealed the values of 19 and 16 eV for $Q = 9$ and 12, respectively [74]. In case of the rectangular nanohole, it was found that the calculated energy gaps are fitted well to Pedersen's scaling rule (8.1) only when $Q = 6, 9$, and 12 (i.e. when $Q = 3m$) with a value of ω ranges between 16.5 and 17 eV (Table 8.2). While for $Q = 7$ and 10 (i.e. $Q = 3m+1$), the gaps do not obey the formula (8.1). To obtain better fitting, we modified the Pedersen formula by including an exponential term such that the energy gap takes the following form

$$E_g = \omega \frac{N_r^{1/2}}{N_t} - b\, \mathrm{e}^{cN_r/N_t} \tag{8.2}$$

where b and c are adjusted parameters. Using this formula gives better fitting for all

Table 8.2: The fitting parameters ω, b, and c using different formulas. ω and b are measured in eV and c is dimensionless.

	Q							
	Hexagonal hole			Rectangular hole				
	6	9	12	6	7	9	10	12
$\omega^{\dagger}$	18.69	19.95	20.01	16.47	—	16.80	—	16.89
$\omega^{\ddagger}$	—	—	—	20.54	28.59	18.36	26.79	17.48
$b^{\ddagger}$	—	—	—	0.133	0.575	0.034	0.370	0.00958
$c^{\ddagger}\times 10^{-4}$	—	—	—	-0.755	1.85	10.0	5.60	3.58

† Fitted to equation (8.1).
‡ Fitted to equation (8.2).

the values of Q (i.e $Q = 3m$ and $3m+1$) as shown in Figure 8.7. The values of fitting parameters ω, b, and c are tabulated in Table 8.2.

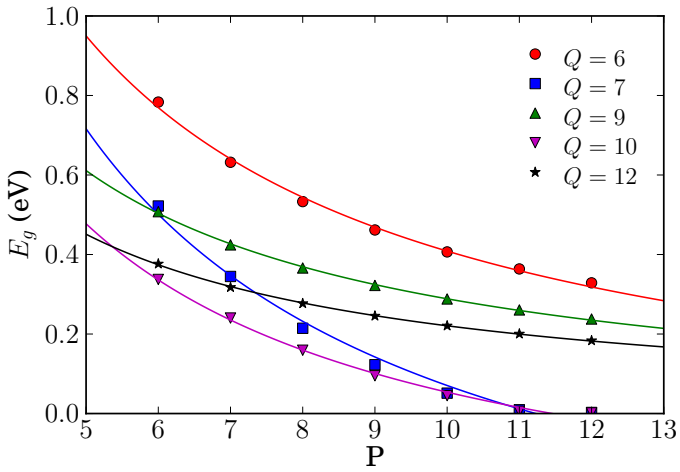

Figure 8.7: The energy band gap (E_g) of GNMs with rectangular nanohole as a function of lattice parameter P for various values of Q. The data are fitted to equation (8.2).

Fixing the unit cell of a GNM (P and Q are fixed) and changing the hole size (N_r), result in E_g varying with N_r as shown in Figure 8.8. In this figure, the dashed lines represent fitting our data according to the scaling rule (8.1). This is not a very good fit, but the fit can be improved by allowing the exponent of N_r to vary as suggested by Oswald and Wu [74]. That is, the modified formula reads

$$E_g = \omega \frac{N_r^{\sigma}}{N_t}, \tag{8.3}$$

where the exponent σ is used instead of $^1/_2$ and is regarded as a fitting parameter. Oswald and Wu found that $\sigma = 0.3$, with $\omega = 35$ and 42 for the GNMs (5×9) and (7×12)

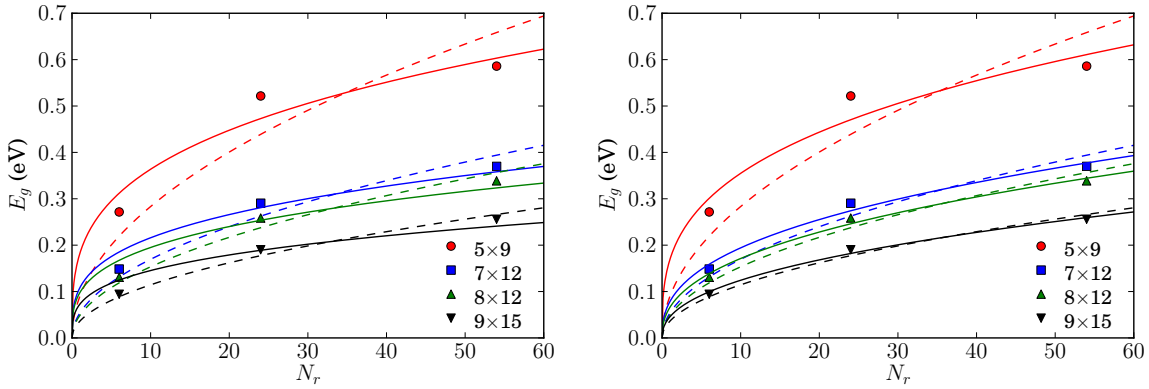

Figure 8.8: The energy band gap (E_g) as a function of the size of hexagonal hole punched in a GNM with fixed lattice parameters (P and Q). The dashed lines are fitted of the calculated points to the Pedersen formula (8.1). The solid lines represent the fitting of our data to Oswald formula (8.3) (left) with $\sigma = 0.3$ and (right) with σ treated as a scaling parameter.

respectively, gives better fitting than formula (8.1) does. Figure 8.8 shows the fitting of our data to Pedersen and Oswald formulas represented by dashed and solid lines respectively. In panel (a), the exponent σ has treated as a constant equal to 0.3 while in (b) we allowed for the exponent to vary as additional scaling parameter alongside ω. As can be seen, the agreement is good in the case of the GNMs (5×9) and (7×12), however, with larger GNMs we can see that the Pedersen return to give better description of the energy gap.

The mechanism of opening a gap in GNMs could be understood within the tight binding model considering π bonding orbitals and nearest neighbour interaction. However, deriving an analytical expression for the Hamiltonian that describes a GNM is not trivial owing to its huge unit cell and the complex boundary conditions at hole edges. Alternatively, we can imagine that, the periodic holes in graphene produce a periodic

Table 8.3: The fitting parameters of equation (8.3) for various GNMs punched with hexagonal nanohole of different sizes. The exponent σ was treated as fixed and adjustable parameter. In the case of fixed σ, the only scaling parameter is ω.

$P \times Q$	σ is fixed		σ is varied	
	$\omega^{\dagger}$	$\omega^{\ddagger}$	ω	σ
5×9	16.13	32.81	30.44	0.32
7×12	18.02	36.38	26.37	0.39
8×12	18.63	37.54	25.37	0.41
9×15	19.56	39.33	24.61	0.44

† Fitted to equation (8.1) (i.e. $\sigma = 0.5$).
‡ Fitted to equation (8.3) (i.e. $\sigma = 0.3$).

perturbation which in turn modifies the band structure of pristine graphene and opens a gap. In the neighbourhood of the Dirac point, the energy dispersion takes the linear form

$$\varepsilon_{\mp}(\vec{q}) = E_0 \mp \hbar v_F \vec{q} \tag{8.4}$$

where $\vec{q}$ is a small wave vector [1] and is measured relatively to the Dirac point as $\vec{q} = \vec{k} - \vec{\mathrm{K}}$, v_F is the electron's Fermi speed ($\sim 10^6$ m/s), E_0 is the top of the valence band and finally the (+) and (-) signs refer to the conduction and valence bands respectively.

Punching periodic holes in a graphene sheet can be viewed as "*digging*" infinite wells in the graphene potential land. These potential wells of unpenetrated walls cause the electronic wave functions to vinish at the hole edge. Consequencely, the linear relashionship between energy and momentum (equation (8.4)) is modified and the point apex of Dirac cone becomes smoother similar to those for GNRs and CNTs [74].

Many of the energy bands originate directly from that of pristine graphene without noticeable changes, except for those that appear around Fermi energy. To compare the band structure of a system with a unit cell rather than primitive one, the folded bands are necessary to be considered. The six Dirac points of the primitive hexagonal BZ of graphene are folded to the k_y axis in the BZ for conventional rectangular unit cell. In the case of a GNM described by $P \times Q$ rectangular unit cell, further folding of the k points in the BZ of the conventional unit cell occurs into the BZ of the GNM. The k points are folded $P-1$ and $Q-1$ times along k_x and k_y axes respectively. Therefore, the original Dirac point is located somewhere along the $\Gamma-\mathrm{Y}$ direction of GNM's BZ where the opening of a gap might occur. As a result, varying Q in a GNM changes the energy dispersion characteristics along the $\Gamma-\mathrm{Y}$ direction, while changing P only gradually modifies the dispersion quantitatively.

8.3 Transport properties

The transmission spectrum of various GNMs with hexagonal hole were calculated to inspect the dependency of the conductance on the lattice parameters P and Q and the hole size. By comparing the transmission graphs depicted in Figure 8.9 with that of band

[1] The assumption of smallness of $\vec{q}$ is required to ensure that the linearity of the energy dispersion is valid.

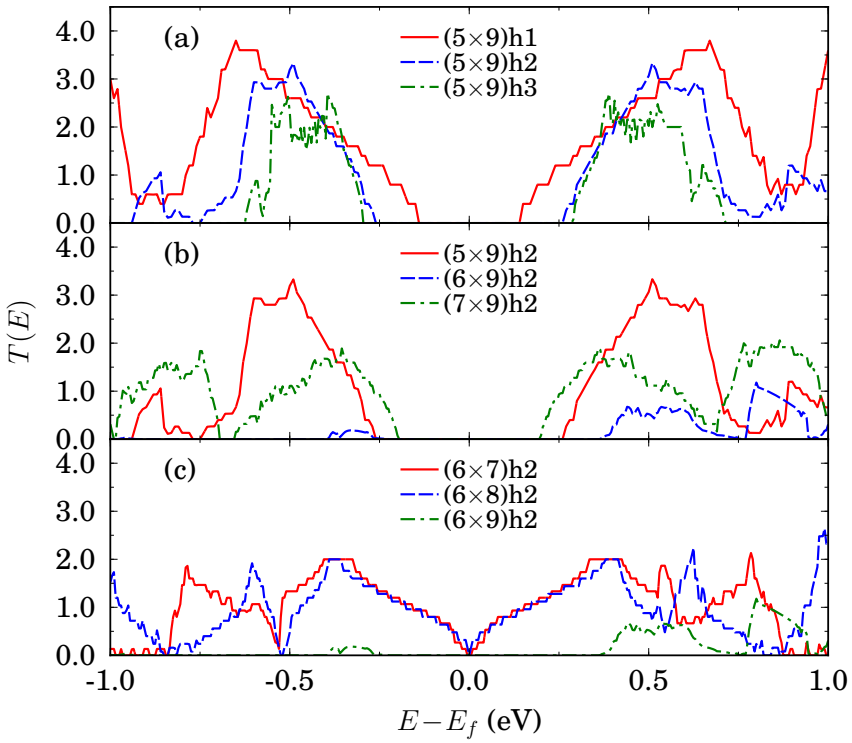

Figure 8.9: The transmission spectrum of various GNMs with a hexagonal hole, (a) for different hole sizes using (5×9) GNM, (b) for $Q = 9$ and different P, and (c) for $P = 6$ and different Q. In the case of (b) and (c) a hexagonal hole with 24 carbon atoms has been used.

structure shown in Figure 8.4, we can see clearly that the conductance behaviour of the GNMs is originated directly from the electronic band structure. The only exception is the (6×9) GNM, that is because transmission spectra exhibits a gap of 0.625 eV while the band structure calculations reveal a gap of 0.451 eV. In addition, the conductance totally vanishes over the range -1.0 to 0.38 eV except a little (ramp) plateau around -0.33 eV.

8.4 Conclusions

We demonstrated that GNMs provide great flexibility in engineering structure with desired band gaps. This is because a number of factors can be varied. This includes the size of the structure which in turn is determined by the repeat distance of the conventional unit cell of pristine graphene. In addition, the size and shape of the holes affect the band gap, band structure and transport properties making the GNMs an exciting for the future applications.

CHAPTER 9

CONCLUSIONS

9.1 Summary

In this thesis, a C++ code named EHTransport, developed at Cardiff University and based on the self consistent extended Hückel theory, was used to investigate the electronic band structure and electrical transport properties of various systems. These systems include the biological molecules, porphyrin and DNA, and graphene based materials represented by nanoribbons, grain boundaries and nanomeshes. One of the aims of the present work was to demonstrate that EHT is able to produce reliable results for small systems such as porphyrin molecules which are comparable to those obtained by *ab initio* methods. Having established this, EHT was applied to study larger systems beyond the scope of *ab initio* techniques. Two classes of systems were investigated: molecular wires and 2D graphene based interconnects.

In studying molecular wires, the SC-EHT approach was used to investigate the factors that influence the electronic and transport properties of porphyrin molecules. This included the molecular length, metal atom at the centre of porphyrin ring, molecular conformation, and the effect of water molecules surrounding the molecule. It was found that the conductance of a nanowire made from porphyrin showed an exponential dependence on the wire's length with an attenuation factor β equals to 0.149 Å^{-1}. This exponential dependence reveals that the main mechanism of the electronic transport in porphyrin based systems is the coherent tunneling. It was also shown that changing the central metal atom in porphyrin ring can affect the behaviour of the transmission function. In addition, investigating the pathways of bond current showed that most of the current flows through the central metal atom in the case of Fe-porphyrin, while the path around the sides of the porphyrin ring is preferable if the metal atom is Zn.

Finally, our calculations revealed that porphyrins surrounded by water molecules exhibit an enhancement in their conductance.

As with the porphyrin wires, transmission through DNA systems was also found that it depends on a number of factors. Among the important factors are: the length, the base sequence, the base type, and the environment. For example, our calculations showed that the transmission is inversely proportional to the DNA length in agreement with experimental observations. The sequence dependence was demonstrated by calculations that showed the CG sequence to have better conduction than AT sequence. Finally, the presence of water molecules around the DNA fragment also helped improve the conductance. We have been able to demonstrate that the reason for the enhancement of the conductance across molecular wires in solution is a consequence of the change in work function at the contacts. This change in the work function is directly related to the electrostatic interactions and to the polarization of the water.

For the graphene based systems, the EHT parameter set was optimised so that the results for the electronic band structure and DOS of pristine graphene agreed with that found using DFT. Then, the SC-EHT was used to explore various configurations that opened the gap in graphene which is an important control for its electronic and transport properties.

Cutting the 2D graphene into ribbons is one of such methods used to modify its electronic band structure around the Dirac points. These nanoribbons are of two types depending on their edges shape: armchair and zigzag. The armchair ribbons were confirmed to be semiconductors which their energy gap is inversely proportional to the ribbon width. By contrast, the zigzag ribbons preserve the semi-metalitiy nature of pristine graphene. The step function behaviour of the transmission spectra for graphene nanoribbons reveals that the conduction through them occur ballistically. The electronic and transport properties of graphene nanoribbons can be further refined by several methods, including for example, by punching periodic holes in it. Such configurations were also considered and the EHT results were found to be in a good agreement of a previous DFT study.

Graphene sheets with grain boundaries is another approach that can be used for gap engineering. Although, most of grain boundaries structure in polycrystalline graphene show zero gap in the conductance spectra, a few of them, under particular geometrical

circumstances, exhibit a gap which depends mainly on the periodic length of the grain boundary. This feature can be explained usefully by a theoretical model proposed by Yazyev and Louie [53].

Finally, 2D graphene sheets with periodically punched nanoholes were explored. The advantage of this technique is its flexibility in designing the desirable feature through changing various factors. These factors include, the shape and size of the hole, the neck widths that separate the adjacent holes along armchair $W_x \propto P$ and zigzag ($W_y \propto Q$) edges of the sheet, the size of the supercell, and the passivater atoms at the inner edges of the holes. From EHT results, one third of the samples punched with hexagonal holes turn out to be semiconductors with an energy gap decreasing inversely with the neck width W_x. The shape of the holes in the nanomesh also has important effect. Thus a rectangular shaped hole results in a gap in two thirds of the samples with the same trend of energy gap dependence on W_x. Moreover, for the semiconductors graphene nanomeshes with hexagonal holes, it was demonstrated that the energy gap increases with increasing the size of the hole. Most of these characteristics can be understood by imagining that punching nanoholes in 2D sheet of graphene is equivalent to introducing infinite potential wells. These wells can considerably modify the electronic and transport properties of GNMs.

9.2 Further work

Future research can be made on two different aspects:

1. Extending the ability of the EHTransport code. There are many potential approaches to extend and improve the efficiency of the current version of the EHTransport code, such as, using parallel algorithms wherever it is possible, developing a graphic user interface (GUI) software to help set up the geometrical structures of systems to be investigated, and adding some other features like energy optimization.

2. Exploring other systems for example the two dimensional graphene like materials, such as MoS_2 and hexagonal boron nitride, GNRs with periodically nanoholes using different passivater atoms at the ribbons edges, and dopping GGBs with some impurities such as nitrogen and boron.

REFERENCES

[1] Gordon E. Moore. Cramming more components onto integrated circuits. *Electronics*, 38(8):4, 1965.

[2] Amit Chaudhry. *Fundamentals of Nanoscaled Field Effect Transistors*. Springer, April 2013.

[3] http://www.itrs.net/links/2011itrs/home2011.htm.

[4] Rolf Landauer. Spatial variation of currents and fields due to localized scatterers in metallic conduction. *IBM Journal of Research and Development*, 1(3):223–231, July 1957.

[5] Rolf Landauer. Electrical resistance of disordered one-dimensional lattices. *Philosophical Magazine*, 21(172):863–867, 1970.

[6] Philip F. Bagwell and Terry P. Orlando. Landauer's conductance formula and its generalization to finite voltages. *Physical Review B*, 40(3):1456–1464, Jul 1989.

[7] C. C. Matthai, G. P. Srivastava, and D. W. Palmer. Control of electrical barriers at semiconductor heterojunctions by interface doping [and discussion]. *Philosophical Transactions of the Royal Society of London. Series A: Physical and Engineering Sciences*, 344(1673):579–586, 1993.

[8] J. M. Bass and C. C. Matthai. Scanning-tunneling-microscopy and spectroscopy simulation of the GaAs(110) surface. *Physical Review B*, 52(7):4712–4715, Aug 1995.

[9] J. R. Reimers, T. X. Lu, M. J. Crossley, and N. S. Hush. Molecular electronic properties of fused rigid porphyrin-oligomer. *Nanotechnology*, 7(4):424–429, 1996.

[10] Aleksey A. Kocherzhenko, Sameer Patwardhan, Ferdinand C. Grozema, Harry L. Anderson, and Laurens D. A. Siebbeles. Mechanism of charge transport along zinc porphyrin-based molecular wires. *Journal of the American Chemical Society*, 131(15):5522–5529, 2009.

[11] H Wende, M Bernien, J Luo, C Sorg, N Ponpandian, J Jurde, J Miguel, M Piantek, X Xu, Ph Eckhold, W Kuch, K Baberschke, P M Panchmatia, B Sanyal, P M Oppeneer, and O Eriksson. Substrate-induced magnetic ordering and switching of iron porphyrin molecules. *Nature Materials*, 6(7):516–520, 2007.

[12] J. R. Reimers, T. X. Lu, M. J. Crossley, and N. S. Hush. Molecular electronic properties of fused rigid porphyrin-oligomer. *Nanotechnology*, 7(4):424–429, 1996.

[13] Aleksey A. Kocherzhenko, Sameer Patwardhan, Ferdinand C. Grozema, Harry L. Anderson, and Laurens D. A. Siebbeles. Mechanism of charge transport along zinc porphyrin-based molecular wires. *Journal of the American Chemical Society*, 131(15):5522–5529, 2009.

[14] Neil Bennett, Gengzhao Xu, Louisa J. Esdaile, Harry L. Anderson, J. Emyr Macdonald, and Martin Elliott. Transition voltage spectroscopy of porphyrin molecular wires. *Small*, 6(22):2604–2611, 2010.

[15] Yanwei Li, Jinhuan Yao, Shengkui Zhong, and Zhengguang Zou. Theoretical investigations on the orientational dependence of electron transport through porphyrin molecular wire. *Current Applied Physics*, 11(6):1349–1353, 2011.

[16] Erez Braun, Yoav Eichen, Uri Sivan, and Gdalyahu Ben-Yoseph. DNA-templated assembly and electrode attachment of a conducting silver wire. *Nature*, 391(6669):775–778, 1998.

[17] Z. Hermon, S. Caspi, and E. Ben-Jacob. Prediction of charge and dipole solitons in DNA molecules based on the behaviour of phosphate bridges as tunnel elements. *Europhysics Letters*, 43(4):482–487, 1998.

[18] E Ben-Jacob, Z Hermon, and S Caspi. DNA transistor and quantum bit element: Realization of nano-biomolecular logical devices. *Physics Letters A*, 263(3):199–202, 1999.

[19] Nadrian C. Seeman. DNA nicks and nodes and nanotechnology. *Nano Letters*, 1(1):22–26, 2001.

[20] K. S. Novoselov, A. K. Geim, S. V. Morozov, D. Jiang, Y. Zhang, S. V. Dubonos, I. V. Grigorieva, and A. A. Firsov. Electric field effect in atomically thin carbon films. *Science*, 306(5696):666–669, 2004.

[21] A. H. Castro Neto, F. Guinea, N. M. R. Peres, K. S. Novoselov, and A. K. Geim. The electronic properties of graphene. *Reviews of Modern Physics*, 81(1):109–162, Jan 2009.

[22] A. K. Geim and Novoselov K. S. The rise of graphene. *Nature Materials*, 6(3):183–191, 2007.

[23] Mikhail I. Katsnelson. Graphene: Carbon in two dimensions. *Materials Today*, 10(1–2):20–27, 2007.

[24] Matthias C. Schabel and José Luís Martins. Energetics of interplanar binding in graphite. *Physical Review B*, 46(11):7185–7188, Sep 1992.

[25] D W Bullett. Chemical pseudopotential approach to covalent bonding. II. Bond lengths and bond energies in diamond, silicon and graphite. *Journal of Physics C: Solid State Physics*, 8(17):2707–2714, 1975.

[26] Changgu Lee, Xiaoding Wei, Jeffrey W. Kysar, and James Hone. Measurement of the elastic properties and intrinsic strength of monolayer graphene. *Science*, 321(5887):385–388, 2008.

[27] Shanshan Chen, Arden L. Moore, Weiwei Cai, Ji Won Suk, Jinho An, Columbia Mishra, Charles Amos, Carl W. Magnuson, Junyong Kang, Li Shi, and Rodney S. Ruoff. Raman measurements of thermal transport in suspended monolayer graphene of variable sizes in vacuum and gaseous environments. *ACS Nano*, 5(1):321–328, 2011.

[28] Alexander A. Balandin. Thermal properties of graphene and nanostructured carbon materials. *Nature Materials*, 10(8):569–581, 2011.

[29] Shanshan Chen, Qingzhi Wu, Columbia Mishra, Junyong Kang, Hengji Zhang, Kyeongjae Cho, Weiwei Cai, Alexander A. Balandin, and Rodney S. Ruoff. Thermal conductivity of isotopically modified graphene. *Nature Materials*, 11(3):203–207, 2012.

[30] A. B. Kuzmenko, E. van Heumen, F. Carbone, and D. van der Marel. Universal optical conductance of graphite. *Physical Review Letters*, 100(11):117401, Mar 2008.

[31] Y.-M. Lin, C. Dimitrakopoulos, K. A. Jenkins, D. B. Farmer, H.-Y. Chiu, A. Grill, and Ph. Avouris. 100-GHz transistors from wafer-scale epitaxial graphene. *Science*, 327(5966):662, 2010.

[32] Ming Liu, Xiaobo Yin, Erick Ulin-Avila, Baisong Geng, Thomas Zentgraf, Long Ju, Feng Wang, and Xiang Zhang. A graphene-based broadband optical modulator. *Nature*, 474(7349):64–67, 2011.

[33] Keun Soo Kim, Yue Zhao, Houk Jang, Sang Yoon Lee, Jong Min Kim, Kwang S. Kim, Jong-Hyun Ahn, Philip Kim, Jae-Young Choi, and Byung Hee Hong. Large-scale pattern growth of graphene films for stretchable transparent electrodes. *Nature*, 457(7230):706–710, 2009.

[34] Yanwu Zhu, Shanthi Murali, Meryl D. Stoller, K. J. Ganesh, Weiwei Cai, Paulo J. Ferreira, Adam Pirkle, Robert M. Wallace, Katie A. Cychosz, Matthias Thommes, Dong Su, Eric A. Stach, and Rodney S. Ruoff. Carbon-based supercapacitors produced by activation of graphene. *Science*, 332(6037):1537–1541, 2011.

[35] Maher F. El-Kady, Veronica Strong, Sergey Dubin, and Richard B. Kaner. Laser scribing of high-performance and flexible graphene-based electrochemical capacitors. *Science*, 335(6074):1326–1330, 2012.

[36] Yan Gao, Xiaoqiang Chen, Hao Xu, Yunlong Zou, Renpeng Gu, Mingsheng Xu, Alex K.-Y. Jen, and Hongzheng Chen. Highly-efficient fabrication of nanoscrolls from functionalized graphene oxide by Langmuir–Blodgett method. *Carbon*, 48(15):4475–4482, 2010.

[37] Xi Yang, Mingsheng Xu, Weiming Qiu, Xiaoqiang Chen, Meng Deng, Jinglin Zhang, Hideo Iwai, Eiichiro Watanabe, and Hongzheng Chen. Graphene uniformly decorated with gold nanodots: In situ synthesis, enhanced dispersibility and applications. *Journal of Materials Chemistry*, 21(22):8096–8103, 2011.

[38] Mingsheng Xu, Daisuke Fujita, and Nobutaka Hanagata. Perspectives and challenges of emerging single-molecule DNA sequencing technologies. *Small*, 5(23):2638–2649, 2009.

[39] S. Garaj, W. Hubbard, A. Reina, J. Kong, D. Branton, and J. A. Golovchenko. Graphene as a subnanometre trans-electrode membrane. *Nature*, 467(7312):190–193, 2010.

[40] MingSheng Xu, Yan Gao, Xi Yang, and HongZheng Chen. Unique synthesis of graphene-based materials for clean energy and biological sensing applications. *Chinese Science Bulletin*, 57(23):3000–3009, 2012.

[41] Meng Deng, Xi Yang, Musa Silke, Weiming Qiu, Mingsheng Xu, Gustaaf Borghs, and Hongzheng Chen. Electrochemical deposition of polypyrrole/graphene oxide composite on microelectrodes towards tuning the electrochemical properties of neural probes. *Sensors and Actuators B: Chemical*, 158(1):176–184, 2011.

[42] Kinam Kim, Jae-Young Choi, Taek Kim, Seong-Ho Cho, and Hyun-Jong Chung. A role for graphene in silicon-based semiconductor devices. *Nature*, 479(7373):338–344, 2011.

[43] Katsunori Wakabayashi, Mitsutaka Fujita, Hiroshi Ajiki, and Manfred Sigrist. Electronic and magnetic properties of nanographite ribbons. *Physical Review B*, 59(12):8271–8282, Mar 1999.

[44] Kyoko Nakada, Mitsutaka Fujita, Gene Dresselhaus, and Mildred S. Dresselhaus. Edge state in graphene ribbons: Nanometer size effect and edge shape dependence. *Physical Review B*, 54(24):17954–17961, Dec 1996.

[45] Katsunori Wakabayashi, Ken ichi Sasaki, Takeshi Nakanishi, and Toshiaki Enoki. Electronic states of graphene nanoribbons and analytical solutions. *Science and Technology of Advanced Materials*, 11(5):054504, 2010.

[46] Mitsutaka Fujita, Masatsura Igami, and Kyoko Nakada. Lattice distortion in nanographite ribbons. *Journal of the Physical Society of Japan*, 66(7):1864–1867, 1997.

[47] Young-Woo Son, Marvin L. Cohen, and Steven G. Louie. Energy gaps in graphene nanoribbons. *Physical Review Letters*, 97(21):216803, Nov 2006.

[48] W. Tian, Y. C. Zeng, and Z. H. Zhang. Electronic properties of graphene nanoribbons with periodically hexagonal nanoholes. *Journal of Applied Physics*, 114(7):074307, 2013.

[49] Hirokazu Takaki and Nobuhiko Kobayashi. Quantum transport properties of zigzag graphene nanoribbons. *Physica E: Low-dimensional Systems and Nanostructures*, 43(3):711–713, 2011.

[50] Humberto Terrones, Ruitao Lv, Mauricio Terrones, and Mildred S Dresselhaus. The role of defects and doping in 2D graphene sheets and 1D nanoribbons. *Reports on Progress in Physics*, 75(6):062501, 2012.

[51] Florian Banhart, Jani Kotakoski, and Arkady V. Krasheninnikov. Structural defects in graphene. *ACS Nano*, 5(1):26–41, 2011.

[52] F Molitor, J Güttinger, C Stampfer, S Dröscher, A Jacobsen, T Ihn, and K Ensslin. Electronic properties of graphene nanostructures. *Journal of Physics: Condensed Matter*, 23(24):243201, 2011.

[53] Oleg V. Yazyev and Steven G. Louie. Electronic transport in polycrystalline graphene. *Nature Materials*, 9(10):806–809, 2010.

[54] Oleg V. Yazyev and Steven G. Louie. Topological defects in graphene: Dislocations and grain boundaries. *Physical Review B*, 81(19):195420–195420–7, May 2010.

[55] Johan M. Carlsson, Luca M. Ghiringhelli, and Annalisa Fasolino. Theory and hierarchical calculations of the structure and energetics of [0001] tilt grain boundaries in graphene. *Physical Review B*, 84(16):165423, Oct 2011.

[56] M. A. Akhukov, A. Fasolino, Y. N. Gornostyrev, and M. I. Katsnelson. Dangling bonds and magnetism of grain boundaries in graphene. *Physical Review B*, 85(11):115407, Mar 2012.

[57] Joice da Silva Araújo and R. W. Nunes. Complex evolution of the electronic structure from polycrystalline to monocrystalline graphene: Generation of a new Dirac point. *Physical Review B*, 81(7):073408, Feb 2010.

[58] Junfeng Zhang and Jijun Zhao. Structures and electronic properties of symmetric and nonsymmetric graphene grain boundaries. *Carbon*, 55(0):151–159, 2013.

[59] Yuanyue Liu and Boris I. Yakobson. Cones, pringles, and grain boundary landscapes in graphene topology. *Nano Letters*, 10(6):2178–2183, 2010.

[60] Te-Huan Liu, Grzegorz Gajewski, Chun-Wei Pao, and Chien-Cheng Chang. Structure, energy, and structural transformations of graphene grain boundaries from atomistic simulations. *Carbon*, 49(7):2306–2317, 2011.

[61] P Simonis, C Goffaux, P.A Thiry, L.P Biro, Ph Lambin, and V Meunier. STM study of a grain boundary in graphite. *Surface Science*, 511(1–3):319–322, 2002.

[62] Kwanpyo Kim, Zonghoon Lee, William Regan, C. Kisielowski, M. F. Crommie, and A. Zettl. Grain boundary mapping in polycrystalline graphene. *ACS Nano*, 5(3):2142–2146, 2011.

[63] Boris I. Yakobson and Feng Ding. Observational geology of graphene, at the nanoscale. *ACS Nano*, 5(3):1569–1574, 2011.

[64] J. Červenka and C. F. J. Flipse. Structural and electronic properties of grain boundaries in graphite: Planes of periodically distributed point defects. *Physical Review B*, 79(19):195429, May 2009.

[65] Jayeeta Lahiri, You Lin, Pinar Bozkurt, Ivan I. Oleynik, and Matthias Batzill. An extended defect in graphene as a metallic wire. *Nature Nanotechnology*, 5(5):326–329, 2010.

[66] A. Mesaros, S. Papanikolaou, C. F. J. Flipse, D. Sadri, and J. Zaanen. Electronic states of graphene grain boundaries. *Physical Review B*, 82(20):205119, Nov 2010.

[67] Jiang-Tao Wu, Xing-Hua Shi, and Yu-Jie Wei. Tunable band structures of polycrystalline graphene by external and mismatch strains. *Acta Mechanica Sinica*, 28(6):1539–1544, 2012.

[68] Junfeng Zhang, Junfeng Gao, Lizhao Liu, and Jijun Zhao. Electronic and transport gaps of graphene opened by grain boundaries. *Journal of Applied Physics*, 112(5):053713, 2012.

[69] Thomas G. Pedersen, Christian Flindt, Jesper Pedersen, Niels Asger Mortensen, Antti-Pekka Jauho, and Kjeld Pedersen. Graphene antidot lattices: Designed defects and spin qubits. *Physical Review Letters*, 100(13):136804, Apr 2008.

[70] Jingwei Bai, Xing Zhong, Shan Jiang, Yu Huang, and Xiangfeng Duan. Graphene nanomesh. *Nature Nanothechnology*, 5(3):190–194, 2010.

[71] Omid Akhavan. Graphene nanomesh by ZnO nanorod photocatalysts. *ACS Nano*, 4(7):4174–4180, 2010.

[72] Fangping Ouyang, Shenglin Peng, Zhongfan Liu, and Zhirong Liu. Bandgap opening in graphene antidot lattices: The missing half. *ACS Nano*, 5(5):4023–4030, 2011.

[73] H. Şahin and S. Ciraci. Structural, mechanical, and electronic properties of defect-patterned graphene nanomeshes from first principles. *Physical Review B*, 84(3):035452, Jul 2011.

[74] William Oswald and Zhigang Wu. Energy gaps in graphene nanomeshes. *Physical Review B*, 85(11):115431, Mar 2012.

[75] Wei Liu, Z. F. Wang, Q. W. Shi, Jinlong Yang, and Feng Liu. Band-gap scaling of graphene nanohole superlattices. *Physical Review B*, 80(23):233405, Dec 2009.

[76] Hideyuki Jippo, Mari Ohfuchi, and Chioko Kaneta. Theoretical study on electron transport properties of graphene sheets with two- and one-dimensional periodic nanoholes. *Physical Review B*, 84(7):075467, Aug 2011.

[77] René Petersen, Thomas Garm Pedersen, and Antti-Pekka Jauho. Clar sextet analysis of triangular, rectangular, and honeycomb graphene antidot lattices. *ACS Nano*, 5(1):523–529, 2011.

[78] X. Y. Cui, R. K. Zheng, Z. W. Liu, L. Li, B. Delley, C. Stampfl, and S. P. Ringer. Magic numbers of nanoholes in graphene: Tunable magnetism and semiconductivity. *Physical Review B*, 84(12):125410, Sep 2011.

[79] Mitsutaka Fujita, Katsunori Wakabayashi, Kyoko Nakada, and Koichi Kusakabe. Peculiar localized state at zigzag graphite edge. *Journal of the Physical Society of Japan*, 65(7):1920–1923, 1996.

[80] Xuesong Li, Weiwei Cai, Jinho An, Seyoung Kim, Junghyo Nah, Dongxing Yang, Richard Piner, Aruna Velamakanni, Inhwa Jung, Emanuel Tutuc, Sanjay K. Banerjee, Luigi Colombo, and Rodney S. Ruoff. Large-area synthesis of high-quality and uniform graphene films on copper foils. *Science*, 324(5932):1312–1314, 2009.

[81] Sukang Bae, Hyeongkeun Kim, Youngbin Lee, Xiangfan Xu, Jae-Sung Park, Yi Zheng, Jayakumar Balakrishnan, Tian Lei, Hye Ri Kim, Young Il Song, Young-Jin Kim, Kwang S. Kim, Barbaros Ozyilmaz, Jong-Hyun Ahn, Byung Hee Hong, and Sumio Iijima. Roll-to-roll production of 30-inch graphene films for transparent electrodes. *Nature Nanotechnology*, 5(8):574–578, 2010.

[82] Kyozaburo Takeda and Kenji Shiraishi. Theoretical possibility of stage corrugation in Si and Ge analogs of graphite. *Physical Review B*, 50(20):14916–14922, Nov 1994.

[83] Bernard Aufray, Abdelkader Kara, Sébastien Vizzini, Hamid Oughaddou, Christel Léandri, Benedicte Ealet, and Guy Le Lay. Graphene-like silicon nanoribbons on Ag(110): A possible formation of silicene. *Applied Physics Letters*, 96(18):183102, 2010.

[84] S. Cahangirov, M. Topsakal, E. Aktürk, H. Şahin, and S. Ciraci. Two- and one-dimensional honeycomb structures of silicon and germanium. *Physical Review Letters*, 102(23):236804, Jun 2009.

[85] E. Fortin and W. M. Sears. Photovoltaic effect and optical absorption in MoS_2. *Journal of Physics and Chemistry of Solids*, 43(9):881–884, 1982.

[86] Branimir Radisavljevic, Michael Brian Whitwick, and Andras Kis. Integrated circuits and logic operations based on single-layer MoS_2. *ACS Nano*, 5(12):9934–9938, 2011.

[87] Branimir Radisavljevic, Michael B. Whitwick, and Andras Kis. Correction to integrated circuits and logic operations based on single-layer MoS_2. *ACS Nano*, 7(4):3729–3729, 2013.

[88] Kin Fai Mak, Changgu Lee, James Hone, Jie Shan, and Tony F. Heinz. Atomically thin MoS_2: A new direct-gap semiconductor. *Physical Review Letters*, 105(13):136805, Sep 2010.

[89] B Radisavljevic, A Radenovic, J Brivio, V Giacometti, and A Kis. Single-layer MoS_2 transistors. *Nature Nanotechnology*, 6(3):147–150, 2011.

[90] Ki Kang Kim, Allen Hsu, Xiaoting Jia, Soo Min Kim, Yumeng Shi, Mario Hofmann, Daniel Nezich, Joaquin F. Rodriguez-Nieva, Mildred Dresselhaus, Tomas Palacios, and Jing Kong. Synthesis of monolayer hexagonal boron nitride on Cu foil using chemical vapor deposition. *Nano Letters*, 12(1):161–166, 2012.

[91] Wei Chen, Yafei Li, Guangtao Yu, Chen-Zhong Li, Shengbai B. Zhang, Zhen Zhou, and Zhongfang Chen. Hydrogenation: A simple approach to realize semiconductor-half-metal-metal transition in boron nitride nanoribbons. *Journal of the American Chemical Society*, 132(5):1699–1705, 2010.

[92] Gareth Jones. *Investigation of the electronic conduction of large molecules via semi-empirical techniques*. PhD thesis, Cardiff School of Physics and Astronomy, August 2012.

[93] L. H. Thomas. The calculation of atomic fields. *Mathematical Proceedings of the Cambridge Philosophical Society*, 23(05):542–548, 1927.

[94] P. Hohenberg and W. Kohn. Inhomogeneous electron gas. *Physical Review*, 136(3B):B864–B871, Nov 1964.

[95] Juan Carlos Cuevas and Elke Scheer. *Molecular Electronics: An Introduction to Theory and Experiment*, volume 1 of *World Scientific Series in Nanoscience and Nanotechnology*. World Scientific, 2010.

[96] M. Born und R. Oppenheimer. Zur quantentheorie der molekeln. *Annalen der Physik (Leipzig)*, 84(3):457–484, 1927.

[97] F. Bloch. Über die quantenmechanik der elektronen in kristallgittern. *Zeitschrift für Physik*, 52(7-8):555–600, 1929.

[98] W. J. Carr. Energy, specific heat, and magnetic properties of the low-density electron gas. *Physical Review*, 122(5):1437–1446, Jun 1961.

[99] W. J. Carr and A. A. Maradudin. Ground-state energy of a high-density electron gas. *Physical Review*, 133(2A):A371–A374, Jan 1964.

[100] D. M. Ceperley and B. J. Alder. Ground state of the electron gas by a stochastic method. *Physical Review Letters*, 45(7):566–569, Aug 1980.

[101] John P. Perdew and Yue Wang. Accurate and simple analytic representation of the electron-gas correlation energy. *Physical Review B*, 45(23):13244–13249, Jun 1992.

[102] W. Kohn and L. J. Sham. Self-consistent equations including exchange and correlation effects. *Physical Review*, 140(4A):A1133–A1138, Nov 1965.

[103] Frank Herman, John P. Van Dyke, and Irene B. Ortenburger. Improved statistical exchange approximation for inhomogeneous many-electron systems. *Physical Review Letters*, 22(16):807–811, Apr 1969.

[104] W. Kohn. Nobel lecture: Electronic structure of matter—wave functions and density functionals. *Reviews of Modern Physics*, 71(5):1253–1266, Oct 1999.

[105] Richard M. Martin. *Electronic Structure: Basic Theory and Practical Methods*. Cambridge University Press, Cambridge, UK, 2004.

[106] John P. Perdew, Kieron Burke, and Matthias Ernzerhof. Generalized gradient approximation made simple. *Physcal Review Letters*, 77(18):3865–3868, Oct 1996.

[107] John P. Perdew, Kieron Burke, and Matthias Ernzerhof. Generalized gradient approximation made simple [physical review letters 77, 3865 (1996)]. *Physcal Review Letters*, 78(7):1396–1396, Feb 1997.

[108] B. Hammer, L. B. Hansen, and J. K. Nørskov. Improved adsorption energetics within density-functional theory using revised Perdew-Burke-Ernzerhof functionals. *Physical Review B*, 59(11):7413–7421, Mar 1999.

[109] John P. Perdew and Kieron Burke. Comparison shopping for a gradient-corrected density functional. *International Journal of Quantum Chemistry*, 57(3):309–319, 1996.

[110] J. M. Seminario and P. Politzer. *Modern Density Functional Theory: A Tool for Chemistry*, volume 2 of *Theoretical and Computational Chemistry (Book 2)*. Elsevier Science B.V., Amsterdam, The Nertherlands, 1995.

[111] Yong-Hoon Kim, In-Ho Lee, Satyadev Nagaraja, Jean-Pierre Leburton, Randolph Q. Hood, and Richard M. Martin. Two-dimensional limit of exchange-correlation energy functional approximations. *Physical Review B*, 61(8):5202–5211, Feb 2000.

[112] Axel D. Becke. A new mixing of Hartree-Fock and local density functional theories. *The Journal of Chemical Physics*, 98(2):1372–1377, 1993.

[113] Axel D. Becke. Density functional thermochemistry. III. The role of exact exchange. *The Journal of Chemical Physics*, 98(7):5648–5652, 1993.

[114] P. J. Stephens, F. J. Devlin, C. F. Chabalowski, and M. J. Frisch. Ab initio calculation of vibrational absorption and circular dichroism spectra using density functional force fields. *The Journal of Physical Chemistry*, 98(45):11623–11627, 1994.

[115] Phillip A. Christiansen, Yoon S. Lee, and Kenneth S. Pitzer. Improved abinitio effective core potentials for molecular calculations. *The Journal of Chemical Physics*, 71(11):4445–4450, 1979.

[116] Morris Krauss and Walter J. Stevens. Effetive potentials in molecular quantum chemistry. *Annual Review of Physical Chemistry*, 35:357–385, 1984.

[117] D. R. Hamann, M. Schlüter, and C. Chiang. Norm-conserving pseudopotentials. *Physical Review Letters*, 43(20):1494–1497, Nov 1979.

[118] F. Bloch. Bemerkung zur elektronentheorie des ferromagnetismus und der elektrischen leitfähigkeit. *Zeitschrift für Physik*, 57(7-8):545–555, 1929.

[119] Roald Hoffmann. An extended Hückel theory. I. Hydrocarbons. *The Journal of Chemical Physics*, 39(6):1397–1412, 1963.

[120] Erich Hückel. Quantentheoretische beiträge zum benzolproblem. *Zeitschrift für Physik A Hadrons and Nuclei*, 70(3-4):204–286, 1931.

[121] Erich Hückel. Quanstentheoretische beiträge zum benzolproblem. *Zeitschrift für Physik A Hadrons and Nuclei*, 72(5-6):310–337, 1931.

[122] Erich Hückel. Quantentheoretische beiträge zum problem der aromatischen und ungesättigten verbindungen. III. *Zeitschrift für Physik A Hadrons and Nuclei*, 76(9-10):628–648, 1932.

[123] Erich Hückel. Die freien radikale der organischen chemie. *Zeitschrift für Physik A Hadrons and Nuclei*, 83(9-10):632–668, 1933.

[124] R. S. Mulliken. Electronic population analysis on LCAO-MO molecular wave functions. I. *The Journal of Chemical Physics*, 23(10):1833–1840, 1955.

[125] Alan E. Reed, Robert B. Weinstock, and Frank Weinhold. Natural population analysis. *The Journal of Chemical Physics*, 83(2):735–746, 1985.

[126] Kurt Stokbro, Dan Erik Petersen, Søren Smidstrup, Anders Blom, Mads Ipsen, and Kristen Kaasbjerg. Semiempirical model for nanoscale device simulations. *Physical Review B*, 82(7):075420, Aug 2010.

[127] Mads Brandbyge, José-Luis Mozos, Pablo Ordejón, Jeremy Taylor, and Kurt Stokbro. Density-functional method for nonequilibrium electron transport. *Physical Review B*, 65(16):165401, Mar 2002.

[128] James D. Talman. Expression for overlap integrals of Slater orbitals. *Physical Review A*, 48(1):243–249, Jul 1993.

[129] http://www.quantumwise.com/documents/manuals.

[130] Yoseph Imry and Rolf Landauer. Conductance viewed as transmission. *Reviews of Modern Physics*, 71(2):S306–S312, Mar 1999.

[131] V. M. Garcia-Suarez and Colin Lambert. Non-trivial length dependence of the conductance and negative differential resistance in atomic molecular wires. *Nanotechnology*, 19(45):455203–455207, 2008.

[132] Cai-Juan Xia, De-Sheng Liu, Han-Chen Liu, and Xue-Jun Zhai. Large negative differential resistance in a molecular device with asymmetric contact geometries: A first-principles study. *Physica E: Low-dimensional Systems and Nanostructures*, 43(8):1518–1521, 2011.

[133] K. Hansen, E. Lægsgaard, I. Stensgaard, and F. Besenbacher. Quantized conductance in relays. *Physical Review B*, 56(4):2208–2220, Jul 1997.

[134] Magnus Paulsson, Ferdows Zahid, and Supriyo Datta. Resistance of a Molecule. In William A. Goddard III, Donald W. Brenner, Sergey Edward Lyshevski, and Gerald J. Iafrate, editors, *Handbook of Nanoscience, Engineering, and Technology*. CRC Press, 2nd edition, June 2007.

[135] S. Datta. *Electronic Transport in Mesoscopic Systems*. Cambridge University Press, Cambridge, UK, 1997.

[136] Y. Imry. *Introduction to Mesoscopic Physics*. Oxford University Press, Oxford, UK, 1997.

[137] Richard H. Summerville and Roald Hoffmann. Tetrahedral and other M_2L_2 transition metal dimers. *Journal of the American Chemical Society*, 98(23):7240–7254, 1976.

[138] Sanshiro Komiya, Thomas A. Albright, Roald Hoffmann, and Jay K. Kochi. Reductive elimination and isomerization of organogold complexes. Theoretical studies of trialkylgold species as reactive intermediates. *Journal of the American Chemical Society*, 98(23):7255–7265, 1976.

[139] Pekka Pyykkö and Lawrence L. Lohr. Relativistically parameterized extended Hückel calculations. 3. Structure and bonding for some compounds of uranium and other heavy elements. *Inorganic Chemistry*, 20(7):1950–1959, 1981.

[140] Noel J. Fitzpatrick and George H. Murphy. Double zeta d radial wave functions for transition elements. *Inorganica Chimica Acta*, 111(2):139–140, 1986.

[141] Pekka Pyykkö and Leif Laaksonen. Relativistically parameterized extended Hückel calculations. 8. Double-ζ parameters for the actinoids Th, Pa, U, Np, Pu, and Am and an application on uranyl. *The Journal of Physical Chemistry*, 88(21):4892–4895, 1984.

[142] J. Cerdá and F. Soria. Accurate and transferable extended Hückel-type tight-binding parameters. *Physical Review B*, 61(12):7965–7971, Mar 2000.

[143] D. Kienle, J. I. Cerda, and A. W. Ghosh. Extended Hückel theory for band structure, chemistry, and transport. I. Carbon nanotubes. *Journal of Applied Physics*, 100(4):043714, 2006.

[144] José M Soler, Emilio Artacho, Julian D Gale, Alberto García, Javier Junquera, Pablo Ordejón, and Daniel Sánchez-Portal. The SIESTA method for ab initio order-N materials simulation. *Journal of Physics: Condensed Matter*, 14(11):2745, 2002.

[145] Emilio Artacho, E Anglada, O Diéguez, J D Gale, A García, J Junquera, R M Martin, P Ordejón, J M Pruneda, D Sánchez-Portal, and J M Soler. The SIESTA method; developments and applicability. *Journal of Physics: Condensed Matter*, 20(6):064208, 2008.

[146] Daniel Sánchez-Portal, Pablo Ordejón, Emilio Artacho, and José M. Soler. Density-functional method for very large systems with LCAO basis sets. *International Journal of Quantum Chemistry*, 65(5):453–461, 1997.

[147] Pablo Ordejón, Emilio Artacho, and José M. Soler. Self-consistent order-N density-functional calculations for very large systems. *Physical Review B*, 53(16):R10441–R10444, Apr 1996.

[148] Javier Junquera, Óscar Paz, Daniel Sánchez-Portal, and Emilio Artacho. Numerical atomic orbitals for linear-scaling calculations. *Physical Review B*, 64(23):235111, Nov 2001.

[149] Eduardo Anglada, José M. Soler, Javier Junquera, and Emilio Artacho. Systematic generation of finite-range atomic basis sets for linear-scaling calculations. *Physical Review B*, 66(20):205101, Nov 2002.

[150] Mads Brandbyge, José-Luis Mozos, Pablo Ordejón, Jeremy Taylor, and Kurt Stokbro. Density-functional method for nonequilibrium electron transport. *Physical Review B*, 65(16):165401, Mar 2002.

[151] Kurt Stokbro, Jeremy Taylor, Mads Brandbyge, and Pablo Ordejón. TranSIESTA: A spice for molecular electronics. *Annals of the New York Academy of Sciences*, 1006(1):212–226, 2003.

[152] Arieh Aviram and Mark A. Ratner. Molecular rectifiers. *Chemical Physics Letters*, 29(2):277–283, 1974.

[153] Abraham Nitzan and Mark A. Ratner. Electron transport in molecular wire junctions. *Science*, 300(5624):1384–1389, 2003.

[154] F. Zahid, M. Paulsson, and S. Datta. Electrical conduction through molecules. In H. Morkoc, editor, *Advanced Semiconductors and Organic Nano-Techniques*, pages 1–14. Academic Press, New York, 2003.

[155] Richard L. McCreery and Adam Johan Bergren. Progress with molecular electronic junctions: Meeting experimental challenges in design and fabrication. *Advanced Materials*, 21(43):4303–4322, 2009.

[156] Stuart Lindsay. Molecular wires and devices: Advances and issues. *Faraday Discussions*, 131(0):403–409, 2006.

[157] Yoram Selzer, Lintao Cai, Marco A. Cabassi, Yuxing Yao, James M. Tour, Theresa S. Mayer, and David L. Allara. Effect of local environment on molecular conduction: Isolated molecule versus self-assembled monolayer. *Nano Letters*, 5(1):61–65, 2005.

[158] V. Fatemi, M. Kamenetska, J. B. Neaton, and L. Venkataraman. Environmental control of single-molecule junction transport. *Nano Letters*, 11(5):1988–1992, 2011.

[159] Katsunori Tagami, Masaru Tsukada, Takuya Matsumoto, and Tomoji Kawai. Electronic transport properties of free-base tape-porphyrin molecular wires studied by self-consistent tight-binding calculations. *Physical Review B*, 67(24):245324, Jun 2003.

[160] Aleksey A. Kocherzhenko, Sameer Patwardhan, Ferdinand C. Grozema, Harry L. Anderson, and Laurens D. A. Siebbeles. Mechanism of charge transport along zinc porphyrin-based molecular wires. *Journal of the American Chemical Society*, 131(15):5522–5529, 2009.

[161] Hannu Häkkinen. The gold-sulfur interface at the nanoscale. *Nature Chemistry*, 4(6):443–455, 2012.

[162] Tomofumi Tada, Masakazu Kondo, and Kazunari Yoshizawa. Green's function formalism coupled with Gaussian broadening of discrete states for quantum transport: Application to atomic and molecular wires. *The Journal of Chemical Physics*, 121(16):8050–8057, 2004.

[163] Gita Sedghi, Víctor M. García-Suárez, Louisa J. Esdaile, Harry L. Anderson, Colin J. Lambert, Santiago Martín, Donald Bethell, Simon J. Higgins, Martin Elliott, Neil Bennett, J. Emyr Macdonald, and Richard J. Nichols. Long-range electron tunnelling in oligo-porphyrin molecular wires. *Nature Nanotechnology*, 6(8):517–523, 2011.

[164] Gita Sedghi, Katsutoshi Sawada, Louisa J. Esdaile, Markus Hoffmann, Harry L. Anderson, Donald Bethell, Wolfgang Haiss, Simon J. Higgins, and Richard J. Nichols. Single molecule conductance of porphyrin wires with ultralow attenuation. *Journal of the American Chemical Society*, 130(27):8582–8583, 2008.

[165] L. Venkataraman, J. E. Klare, C. Nuckolls, M. S. Hybertsen, and M. L. Steigenwald. Dependence of single-molecule junction conductance on molecular conformation. *Nature*, 442(7105):904–907, 2006.

[166] Ryo Yamada, Hiroaki Kumazawa, Tomoharu Noutoshi, Shoji Tanaka, and Hirokazu Tada. Electrical conductance of oligothiophene molecular wires. *Nano Letters*, 8(4):1237–1240, 2008.

[167] E. Leary, H. Höbenreich, S. J. Higgins, H. van Zalinge, W. Haiss, R. J. Nichols, C. M. Finch, I. Grace, C. J. Lambert, R. McGrath, and J. Smerdon. Single-molecule solvation-shell sensing. *Physical Review Letters*, 102(8):086801, Feb 2009.

[168] James D. Watson, Tania A. Baker, Stephen P. Bell, Alexander Gann, Michael Levine, Richard Losick, and Inglis CSHLP. *Molecular Biology of the Gene: International Ed.* Pearson, 6 edition, December 2007.

[169] R. E. Franklin and R. G. Gosling. The structure of sodium thymonucleate fibres. I. The influence of water content. *Acta Crystallographica*, 6(8-9):673–677, Sep 1953.

[170] R. E. Franklin and R. G. Gosling. The structure of sodium thymonucleate fibres. II. The cylindrically symmetrical Patterson function. *Acta Crystallographica*, 6(8-9):678–685, Sep 1953.

[171] Haiyuan Zhang, Haijia Yu, Jinsong Ren, and Xiaogang Qu. Reversible B/Z-DNA transition under the low salt condition and non-B-form polydApolydT selectivity by a cubane-like europium-L-aspartic acid complex. *Biophysical Journal*, 90(9):3203–3207, 2006.

[172] Christopher R. Treadway, Michael G. Hill, and Jacqueline K. Barton. Charge transport through a molecular π-stack: Double helical DNA. *Chemical Physics*, 281(2–3):409–428, 2002.

[173] Shana O. Kelley and Jacqueline K. Barton. Electron transfer between bases in double helical DNA. *Science*, 283(5400):375–381, 1999.

[174] Melanie A. O'Neil and Jacqueline K. Barton. DNA charge transport: Conformationally gated hopping through stacked domains. *Journal of the American Chemical Society*, 126(37):11471–11483, 2004.

[175] CJ Murphy, MR Arkin, Y Jenkins, ND Ghatlia, SH Bossmann, NJ Turro, and JK Barton. Long-range photoinduced electron transfer through a DNA helix. *Science*, 262(5136):1025–1029, 1993.

[176] Bernd Giese. Long-distance electron transfer through DNA. *Annual Review of Biochemistry*, 71(1):51–70, 2002.

[177] Eric Meggers, Maria E. Michel-Beyerle, and Bernd Giese. Sequence dependent long range hole transport in DNA. *Journal of the American Chemical Society*, 120(49):12950–12955, 1998.

[178] Frederick D. Lewis, Taifeng Wu, Yifan Zhang, Robert L. Letsinger, Scott R. Greenfield, and Michael R. Wasielewski. Distance-dependent electron transfer in DNA hairpins. *Science*, 277(5326):673–676, 1997.

[179] Danith Ly, Laurie Sanii, and Gary B. Schuster. Mechanism of charge transport in DNA: Internally-linked anthraquinone conjugates support phonon-assisted polaron hopping. *Journal of the American Chemical Society*, 121(40):9400–9410, 1999.

[180] A. J. Storm, J. van Noort, S. de Vries, and C. Dekker. Insulating behavior for DNA molecules between nanoelectrodes at the 100 nm length scale. *Applied Physics Letters*, 79(23):3881–3883, 2001.

[181] Danny Porath, Alexey Bezryadin, Simon de Vries, and Cees Dekker. Direct measurement of electrical transport through DNA molecules. *Nature*, 403(6770):635–638, 2000.

[182] K.-H. Yoo, D. H. Ha, J.-O. Lee, J. W. Park, Jinhee Kim, J. J. Kim, H.-Y. Lee, T. Kawai, and Han Yong Choi. Electrical conduction through poly(dA)-Poly(dT) and poly(dG)-poly(dC) DNA molecules. *Physical Review Letters*, 87(19):198102, Oct 2001.

[183] B. Xu, P. Zhang, X. Li, and N. Tao. Direct conductance measurement of single DNA molecules in aqueous solution. *Nano Letters*, 4(6):1105–1108, 2004.

[184] Hezy Cohen, Claude Nogues, Ron Naaman, and Danny Porath. Direct measurement of electrical transport through single DNA molecules of complex sequence. *Proceedings of the National Academy of Sciences of the United States of America*, 102(33):11589–11593, 2005.

[185] A. Rakitin, P. Aich, C. Papadopoulos, Yu. Kobzar, A. S. Vedeneev, J. S. Lee, and J. M. Xu. Metallic conduction through engineered DNA: DNA nanoelectronic building blocks. *Physical Review Letters*, 86(16):3670–3673, Apr 2001.

[186] A. Yu. Kasumov, M. Kociak, S. Guéron, B. Reulet, V. T. Volkov, D. V. Klinov, and H. Bouchiat. Proximity-induced superconductivity in DNA. *Science*, 291(5502):280–282, 2001.

[187] Guohui Zheng, Xiang-Jun Lu, and Wilma K. Olson. Web 3DNA a web server for the analysis, reconstruction, and visualization of three-dimensional nucleic-acid structures. *Nucleic Acids Research*, 37(suppl 2):W240–W246, 2009.

[188] Avogadro: An open-source molecular builder and visualization tool. Version 1.1.0.

[189] Marcus D Hanwell, Donald E Curtis, David C Lonie, Tim Vandermeersch, Eva Zurek, and Geoffrey R Hutchison. Avogadro: An advanced semantic chemical editor, visualization, and analysis platform. *Journal of Cheminformatics*, 4:17, 2012.

[190] Bingqian Q. Xu, Xiulan L. Li, Xiaoyin Y. Xiao, Hiroshi Sakaguchi, and Nongjian J. Tao. Electromechanical and conductance switching properties of single oligothiophene molecules. *Nano Letters*, 5(7):1491–1495, 2005.

[191] P. Benjamin Woiczikowski, Tomáš Kubař, Rafael Gutiérrez, Rodrigo A. Caetano, Gianaurelio Cuniberti, and Marcus Elstner. Combined density functional theory and Landauer approach for hole transfer in DNA along classical molecular dynamics trajectories. *The Journal of Chemical Physics*, 130(21):215104, 2009.

[192] Somenath Roy, Harindra Vedala, Aparna Datta Roy, Do-hyun Kim, Melissa Doud, Kalai Mathee, Hoon-kyu Shin, Nobuo Shimamoto, Viswanath Prasad, and Wonbong Choi. Direct electrical measurements on single-molecule genomic DNA using single-walled carbon nanotubes. *Nano Letters*, 8(1):26–30, 2008.

[193] Xuefeng Guo, Alon A. Gorodetsky, James Hone, Jacqueline K. Barton, and Colin Nuckolls. Conductivity of a single DNA duplex bridging a carbon nanotube gap. *Nature Nanotechnology*, 3(3):163–167, 2008. 10.1038/nnano.2008.4.

[194] R. Saito, G. Dresselhaus, and M. S. Dresselhaus. *Physical Properties of Carbon Nanotubes*. Imperial College Press, London, UK, 1998.

[195] Claire Berger, Zhimin Song, Xuebin Li, Xiaosong Wu, Nate Brown, Cécile Naud, Didier Mayou, Tianbo Li, Joanna Hass, Alexei N. Marchenkov, Edward H. Conrad, Phillip N. First, and Walt A. de Heer. Electronic confinement and coherence in patterned epitaxial graphene. *Science*, 312(5777):1191–1196, 2006.

[196] A. Charrier, A. Coati, T. Argunova, F. Thibaudau, Y. Garreau, R. Pinchaux, I. Forbeaux, J.-M. Debever, M. Sauvage-Simkin, and J.-M. Themlin. Solid-state decomposition of silicon carbide for growing ultra-thin heteroepitaxial graphite films. *Journal of Applied Physics*, 92(5):2479–2484, 2002.

[197] Melinda Y. Han, Barbaros Ozyilmaz, Yuanbo Zhang, and Philip Kim. Energy band-gap engineering of graphene nanoribbons. *Physical Review Letters*, 98(20):206805, May 2007.

[198] Y C Huang, C P Chang, and M F Lin. Magnetic and quantum confinement effects on electronic and optical properties of graphene ribbons. *Nanotechnology*, 18(49):495401, 2007.

[199] N. M. R. Peres, A. H. Castro Neto, and F. Guinea. Dirac fermion confinement in graphene. *Physical Review B*, 73(24):241403, Jun 2006.

[200] P. G. Silvestrov and K. B. Efetov. Quantum dots in graphene. *Physical Review Letters*, 98(1):016802, Jan 2007.

[201] Kyle A. Ritter and Joseph W. Lyding. The influence of edge structure on the electronic properties of graphene quantum dots and nanoribbons. *Nature Materials*, 8(3):235–242, 2009.

[202] S. Y. Zhou, G. H. Gweon, A. V. Fedorov, P. N. First, W. A. de Heer, D. H. Lee, F. Guinea, A. H. Castro Neto, and A. Lanzara. Substrate-induced bandgap opening in epitaxial graphene. *Nature Materials*, 6(10):770–775, 2007.

[203] F. Varchon, R. Feng, J. Hass, X. Li, B. Ngoc Nguyen, C. Naud, P. Mallet, J.-Y. Veuillen, C. Berger, E. H. Conrad, and L. Magaud. Electronic structure of epitaxial graphene layers on SiC: Effect of the substrate. *Physical Review Letters*, 99(12):126805, Sep 2007.

[204] Alexander Grüneis and Denis V. Vyalikh. Tunable hybridization between electronic states of graphene and a metal surface. *Physical Review B*, 77(19):193401, May 2008.

[205] Eli Rotenberg, Aaron Bostwick, Taisuke Ohta, Jessica L. McChesney, Thomas Seyller, and Karsten Horn. Origin of the energy bandgap in epitaxial graphene. *Nature Materials*, 7(4):258–259, 2008.

[206] C. Stampfer, J. Güttinger, S. Hellmüller, F. Molitor, K. Ensslin, and T. Ihn. Energy gaps in etched graphene nanoribbons. *Physical Review Letters*, 102(5):056403, Feb 2009.

[207] D W Boukhvalov and M I Katsnelson. Chemical functionalization of graphene. *Journal of Physics: Condensed Matter*, 21(34):344205, 2009.

[208] D. W. Boukhvalov and M. I. Katsnelson. Chemical functionalization of graphene with defects. *Nano Letters*, 8(12):4373–4379, 2008.

[209] Elena Bekyarova, Mikhail E. Itkis, Palanisamy Ramesh, Claire Berger, Michael Sprinkle, Walt A. de Heer, and Robert C. Haddon. Chemical modification of epitaxial graphene: Spontaneous grafting of aryl groups. *Journal of the American Chemical Society*, 131(4):1336–1337, 2009.

[210] Daniel R. Dreyer, Sungjin Park, Christopher W. Bielawski, and Rodney S. Ruoff. The chemistry of graphene oxide. *Chemical Society Reviews*, 39(1):228–240, 2010.

[211] Lijie Ci, Li Song, Chuanhong Jin, Deep Jariwala, Dangxin Wu, Yongjie Li, Anchal Srivastava, Z. F. Wang, Kevin Storr, Luis Balicas, Feng Liu, and Pulickel M. Ajayan. Atomic layers of hybridized boron nitride and graphene domains. *Nature Materials*, 9(5):430–435, 2010.

[212] Hongtao Liu, Yunqi Liu, and Daoben Zhu. Chemical doping of graphene. *Journal of Materials Chemistry*, 21(10):3335–3345, 2011.

[213] Beidou Guo, Fang Liang, Baohong Zhang, and Jian Ru Gong. Graphene doping: A review. *Insciences Journal*, 1(2):80–89, 2011.

[214] Xiaochang Miao, Sefaattin Tongay, Maureen K. Petterson, Kara Berke, Andrew G. Rinzler, Bill R. Appleton, and Arthur F. Hebard. High efficiency graphene solar cells by chemical doping. *Nano Letters*, 12(6):2745–2750, 2012.

[215] Taisuke Ohta, Aaron Bostwick, Thomas Seyller, Karsten Horn, and Eli Rotenberg. Controlling the electronic structure of bilayer graphene. *Science*, 313(5789):951–954, 2006.

[216] Fengnian Xia, Damon B. Farmer, Yu-ming Lin, and Phaedon Avouris. Graphene field-effect transistors with high on/off current ratio and large transport band gap at room temperature. *Nano Letters*, 10(2):715–718, 2010.

[217] S. Bala Kumar and Jing Guo. Multilayer graphene under vertical electric field. *Applied Physics Letters*, 98(22):222101, 2011.

[218] Liang Z. Tan, Cheol-Hwan Park, and Steven G. Louie. New Dirac fermions in periodically modulated bilayer graphene. *Nano Letters*, 11(7):2596–2600, 2011.

[219] Seon-Myeong Choi, Seung-Hoon Jhi, and Young-Woo Son. Controlling energy gap of bilayer graphene by strain. *Nano Letters*, 10(9):3486–3489, 2010.

[220] Seon-Myeong Choi, Seung-Hoon Jhi, and Young-Woo Son. Effects of strain on electronic properties of graphene. *Physical Review B*, 81(8):081407, Feb 2010.

[221] Zhen Hua Ni, Ting Yu, Yun Hao Lu, Ying Ying Wang, Yuan Ping Feng, and Ze Xiang Shen. Uniaxial strain on graphene: Raman spectroscopy study and band-gap opening. *ACS Nano*, 2(11):2301–2305, 2008.

[222] Vitor M. Pereira, A. H. Castro Neto, and N. M. R. Peres. Tight-binding approach to uniaxial strain in graphene. *Physical Review B*, 80(4):045401, Jul 2009.

[223] Giulio Cocco, Emiliano Cadelano, and Luciano Colombo. Gap opening in graphene by shear strain. *Physical Review B*, 81(24):241412, Jun 2010.

[224] Hendrik J. Monkhorst and James D. Pack. Special points for Brillouin-zone integrations. *Physical Review B*, 13(12):5188–5192, Jun 1976.

[225] Katsunori Wakabayashi. Physics and Chemistry of Graphene: Graphene to Nanographene. In Toshiaki Enoki and Tsuneya Ando, editors, *Electronic Properties of Nanographene*. Pan Stanford Publishing, January 2013.

[226] Yousuke Kobayashi, Ken-ichi Fukui, Toshiaki Enoki, Koichi Kusakabe, and Yutaka Kaburagi. Observation of zigzag and armchair edges of graphite using scanning tunneling microscopy and spectroscopy. *Physical Review B*, 71(19):193406, May 2005.

[227] Yousuke Kobayashi, Ken-ichi Fukui, Toshiaki Enoki, and Koichi Kusakabe. Edge state on hydrogen-terminated graphite edges investigated by scanning tunneling microscopy. *Physical Review B*, 73(12):125415, Mar 2006.

[228] Y. Niimi, T. Matsui, H. Kambara, K. Tagami, M. Tsukada, and Hiroshi Fukuyama. Scanning tunneling microscopy and spectroscopy studies of graphite edges. *Applied Surface Science*, 241(1–2):43 – 48, 2005. The 9th International Symposium on Advanced Physical Fields.

[229] Pavel B Sorokin and Leonid A Chernozatonskii. Graphene-based semiconductor nanostructures. *Physics-Uspekhi*, 56(2):105–122, 2013.

[230] A.P. Sutton and R. W. Balluffi. *Interfaces in Crystalline Materials*. Oxford University Press, Oxford, UK, 1995.

[231] J. H. Los and A. Fasolino. Intrinsic long-range bond-order potential for carbon: Performance in Monte Carlo simulations of graphitization. *Physical Review B*, 68(2):024107, Jul 2003.

[232] Jan H. Los, Luca M. Ghiringhelli, Evert Jan Meijer, and A. Fasolino. Improved long-range reactive bond-order potential for carbon. I. Construction. *Physical Review B*, 72(21):214102, Dec 2005.

[233] Luca M. Ghiringhelli, Jan H. Los, A. Fasolino, and Evert Jan Meijer. Improved long-range reactive bond-order potential for carbon. II. Molecular simulation of liquid carbon. *Physical Review B*, 72(21):214103, Dec 2005.

[234] Pekka Koskinen, Sami Malola, and Hannu Häkkinen. Self-passivating edge reconstructions of graphene. *Physical Review Letters*, 101(11):115502, Sep 2008.

[235] W. H. Brito, R. Kagimura, and R. H. Miwa. B and N doping in graphene ruled by grain boundary defects. *Physical Review B*, 85(3):035404, Jan 2012.